ACTA TECHNICA JAURINENSIS
Vol. 17, No. 1, pp. 1-7, 2023
10.14513/actatechjaur.00723

Effect of Reprocessing on the Crystallization of Different Polyesters

Zoubeida Taha Taha [1,2], Andrea Ádámné Major [1], Ferenc Ronkay[1,*]

[1] Department of Innovative Vehicles and Materials, GAMF Faculty of Engineering and Computer Science, John von Neumann University, Izsáki út 10, H-6000, Kecskemét, Hungary
[2] Doctoral School of Materials Sciences and Technologies, Óbuda University, Népszínház u. 8, H-1081 Budapest, Hungary
*e-mail: ronkay.ferenc@nje.hu

Submitted: 10/11/2023 Accepted: 23/12/2023 Published online: 27/12/2023

Abstract: The changes in crystallization characteristics of four polyesters were investigated during multiple processing. Two of these were petroleum-based materials: poly (ethylene terephthalate) (PET) and poly (butylene terephthalate) (PBT), and two were bio-based materials: poly (lactic acid) (PLA) and poly (butylene succinate) (PBS). We found that during non-isothermal crystallization the different type of polyesters shown different behaviour: the PET and PLA materials were more sensitive to the cooling rate than the PBT and PBS. Interestingly, at low cooling rates, the number of reprocessing steps had no significant effect on the crystallinity of PBT and PBS, but reduced it for PET, but increased it for PBT.

Keywords: polyesters, bio-based polymer, petroleum-based polymer, crystallization, recycling

I. INTRODUCTION

Modern industries need materials that have properties which are not found among the traditional materials used, so the manufacture of materials with special specifications has raised the interest of researchers in recent years [1,2,3,4]. Different types of polyester materials have started to be widely used, since these polymers are commonly used in most applications due to their low cost, adaptability and high mechanical properties such as strength and moisture resistance. They are used as the main component in different industries and daily products such as textiles, clothes, backpacks, home furniture, pillows, napkins, air and water filters, packaging materials, computers and recording tapes, building and construction materials and electrical insulation as well as in the medical field. Also, biodegradable polyester materials are used in environmentally friendly products like compostable bags and food containers [1,2,3,5,6].

Polyester can be classified into two main types depending on the raw materials used in their production. One of them is bio polyester, which is extracted from renewable resources such as microorganisms and plants like sugarcane and corn, the most important of which are polylactic acid (PLA) and polybutylene succinate (PBS) [7,8]. The other type is called petroleum-based polyesters, which can be obtained from petrochemical raw materials, including polyethylene terephthalate (PET) and polybutylene terephthalate (PBT) [9,10]. In addition, bio-based polyesters are considered more environmentally friendly than their petroleum-based counterparts because they reduce dependence on fossil fuels [7,8,9,10]. However, both types of polyesters have their advantages and disadvantages, and the selection of the most suitable option depends on the specific needs of a particular application [7,8,9,10].

Polyester recycling has received great attention in recent years because it helps reduce the amount of waste, energy consuming and environmental impacts and conserve resources [7,9,11]. Also, the recycling process can have an effect on the structure of the polymer, including its crystallinity, thus affect the mechanical properties of polymer [11,12].

The present work was undertaken to study the effect of reprocessing on the non-isothermal crystallization behaviour of PET, PBT, PLA and PBS. This work is intended to provide a better insight into the crystallization kinetics of petroleum-based and bio-based polyesters.

Table 1. *Tested polyesters*

Name	*Origin*	*Type (Producer)*	*MFI parameters*	*MFI value*
PET	Petroleum-based	Neopet 80 (Neogroup)	260°C / 1.2 kg	21 g / 10 min
PBT	Petroleum-based	Pocan B1305 (Lanxess)	250°C / 2.16 kg	47 cm^3 / 10 min
PLA	Bio-based	Ingeo 3100HP (Natureworks)	210°C / 2.16 kg	24 g / 10 min
PBS	Bio-based	BioPBS FZ91PM (PTT MCC Biochem)	190°C / 2.16 kg	6 g / 10 min

II. Materials and Methods

1. Materials

The type and main properties of the two petroleum-based and two bio-based polyesters tested are presented in **Table 1**.

For reprocessing the materials Labtech 26-44 (Labtech Engineering, Thailand) twin screw extruder with a screw diameter of 26 mm and an L/D ratio of 48 was used. The main parameters of extrusion processing are summarized in **Table 2**. This step was repeated twice for the reprocessed samples.

Table 2. *Processing parameters*

Name	*Drying*	*Temperature zones*	*Screw speed*
PET	160 °C / 4 h	270 - 280 °C	34 rpm
PBT	120 °C / 4 h	250 - 260 °C	65 rpm
PLA	90 °C / 5 h	195 - 205 °C	52 rpm
PBS	80 °C / 5 h	160 - 170 °C	85 rpm

2. Methods

Intrinsic viscosity (IV) measurements were done by RPV-1 (PSL Rheotek, USA) automatic solution viscometer according to ASTM D4603 standard. The IV values were measured at 30 °C in a 60/40 weight mixture of phenol/tetrachloroethane solvent with a concentration of 0.5 g/dl.

Crystallization characteristics were investigated using a non-isothermal DSC program using a DSC131 EVO (Setaram, France) device. The measurements were performed in nitrogen atmosphere with a flow rate of 50 ml/min. Samples were heated from room temperature to melting temperature (T_m)+30 °C at a rate of 20 °C/min, held for 4 min to erase thermal history, and then cooled back to 0 °C temperature at different rates (40, 20, 10, 5, and 2.5 °C/min). From the exothermic crystallization peak shown on the cooling curve the peak crystallization temperature was determined. Crystallinity (X_c) was calculated by Eq. (1) from the DSC heating scans at a heating rate of 20 °C/min, after specimens crystallized from a molten state to room temperature with different cooling rates. The area of each peak has been considered as the crystallization and melting enthalpy, ΔH_{cc} and ΔH_m, respectively.

$$X_c = \frac{\Delta H_m - \Delta H_{cc}}{\Delta H_m^0} \qquad (1)$$

The term ΔH_m^0 is a reference value corresponding to the heat of melting of a 100% crystalline polymer, the value of which is 140 J/g for PET [13]; 145 J/g for PBT [14]; 195 J/g for PBS [15] and 93 J/g for PLA [16].

III. Results and Discussion

The degradation of the polyesters during reprocessing was characterised by IV measurements. It was found that reprocessing had no remarkable effect on IV of PBS and PBT, while it led to a decrease in the viscosity of the rest of the types of polyesters used, especially PET as shown in **Table 3**.

Table 3. *Effect of reprocessing on the intrinsic viscosity of PET, PBS, PBT and PLA*

Name	*0x*	*1x*	*2x*
PET	0.79 ± 0.01	0.69 ± 0.01	0.67 ± 0.01
PBT	1.49 ± 0.01	1.49 ± 0.01	1.48 ± 0.01
PLA	0.84 ± 0.01	0.83 ± 0.02	0.82 ± 0.01
PBS	1.26 ± 0.02	1.20 ± 0.01	1.17 ± 0.02

Non-isothermal crystallization was used to investigate how the crystallization of different polyesters changes during multiple processing. Typical DSC curves are shown in **Fig. 1**. It can be seen that as the cooling rate increases, the degree of undercooling increases and the crystallization peak shifts to a lower temperature.

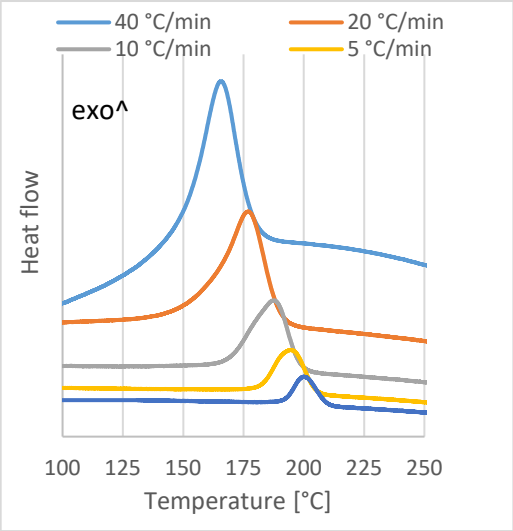

Figure 1. *DSC cooling curves with crystallization exotherm (Once-processed PET sample)*

The evaluations of the measurements are summarised in **Fig. 2** and **3**. The change in crystallinity as a function of the natural logarithm of the cooling rate is shown in Figure 2. For all samples, a logarithmic relationship between the crystallinity formed and the cooling rate is observed. It can be seen that the cooling rate has a marginal effect on crystallinity in PBS and PBT polymers. For the original PET, as well as for the original and recycled PLA materials, a significant change in crystallinity is observed for different cooling rates: faster cooling reduces the proportion of crystalline phase. The resulting crystallinity is generally in the range of 20-30%, except for original PET, where crystallinity is lower at high cooling rates; for once and twice-processed PLA, where the crystallinity is higher than this range at low cooling rates and for all PLA material lower at high cooling rates.

In the case of PLA, the crystallinity increases with the number of processing steps as expected because a decrease in molecular weight results in less restricted chain mobility [17]. However, in the case of PET the reprocessed sample has lower crystallinity than the once-processed sample in the whole cooling rate range. This can be explained by the fact that in PET, the smaller the molecular weight of the fraction, the shorter the chain, which makes it more difficult to fold the chains, the activation energy increases and therefore the crystallization rate is lower [18].

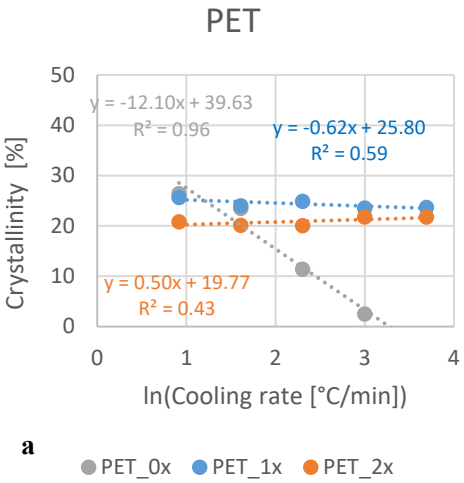

a

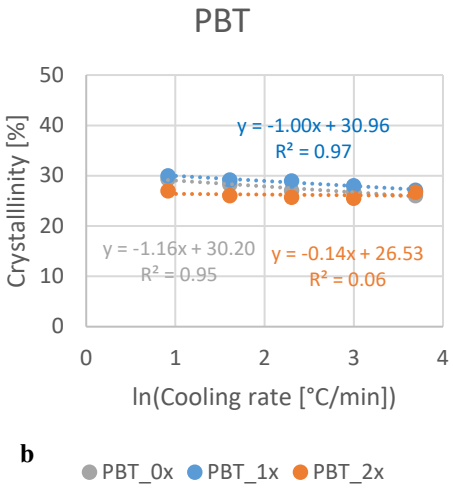

b

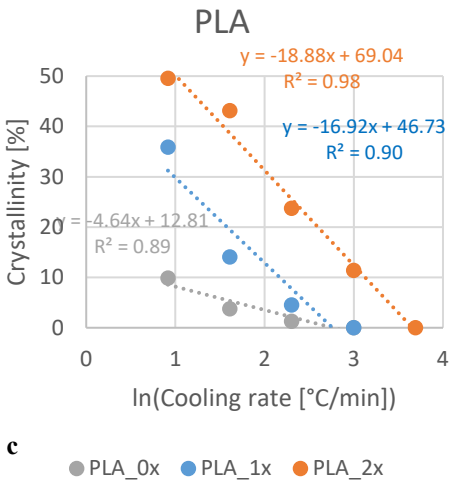

c

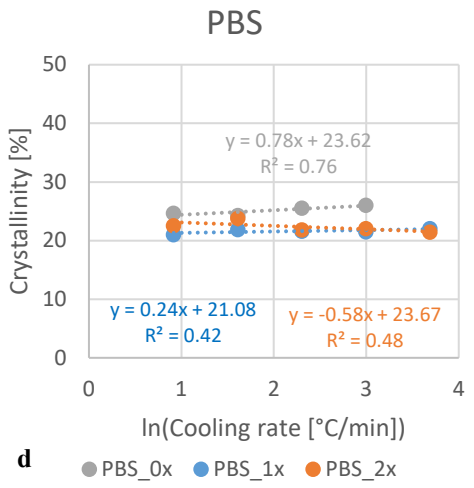

Figure 2. Effect of cooling rate on the crystallinity (a: PET; b: PBT; c: PLA; d: PBS; 0x: original material; 1x: once-processed materials; 2x: twice-processed (reprocessed) materials).

Non-isothermal crystallization data can be analyzed in terms of the degree of undercooling (ΔT_c) defined as the temperature difference between the equilibrium melting temperature (T_{m0}) and the peak temperature of crystallization ($T_{c,p}$) in the cooling scan [19]. The equilibrium melting temperatures used for calculation of the level of undercooling were: 280°C for PET [19], 245°C for PBT [20], 130°C for PBS [21] and 184°C for PLA [22]. It can be established that the degree of undercooling is in each case linearly related to the natural logarithm of the cooling rate (**Fig. 3**). It can be observed that for PET and PBS the original material crystallizes at significantly higher level of undercooling than the once and twice reprocessed variants, while no such big differences are seen for PBT and PLA.

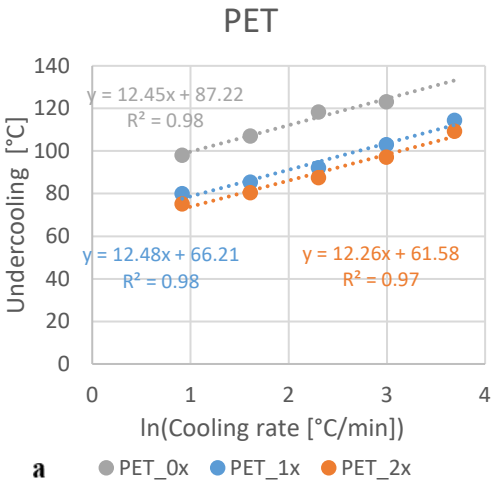

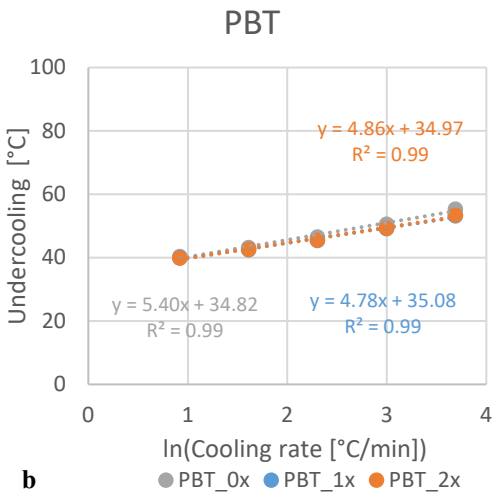

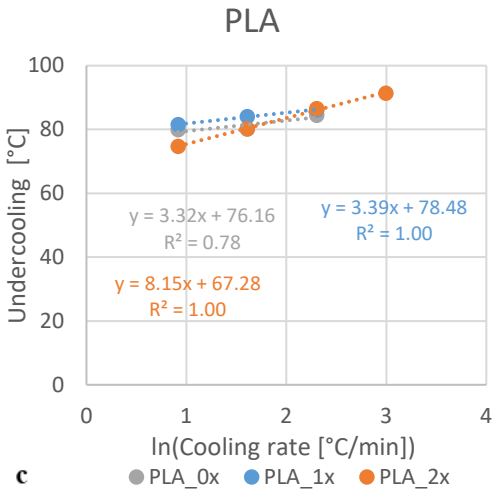

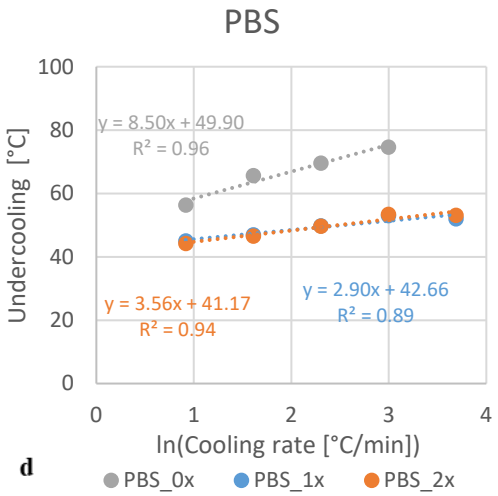

Figure 3. Effect of cooling rate on the degree of undercooling (a: PET; b: PBT; c: PLA; d: PBS; 0x: original material; 1x: once-processed materials; 2x: twice-processed (reprocessed) materials)

Based on Nadkarni et al. [23] the ΔTc with cooling rate can be fitted to a linear equation, however in the polyesters tested in our case these functions show logarithmic trends. Based on the function parameters on **Fig. 2** and **3** we defined the $\Delta T_{c,1}$ as the degree of undercooling required in the 1 °C/min cooling rate which is related to the thermodynamic driving force for nucleation, and ΔXm,1 indicating crystallinity at a cooling rate of 1 °C/min. **Fig. 4** shows the change of $\Delta T_{c,1}$ and $\Delta X_{m,1}$ after the processing steps in the case of the different polyester materials. It can be observed that reprocessing typically reduces the value of $\Delta T_{c,1}$, but the value of $\Delta X_{m,1}$ can vary in several ways during recycling, depending on the type of polyester.

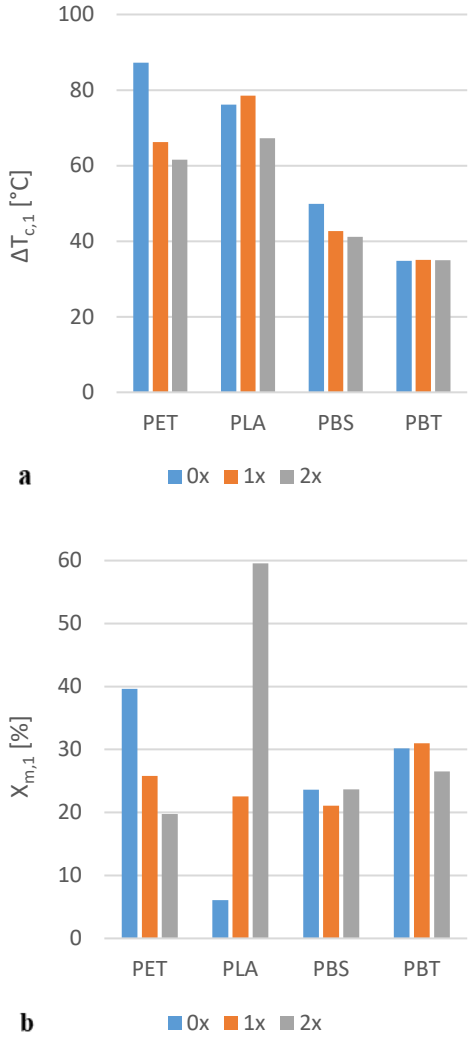

Figure 4. The change of the degree of undercooling (a) and the crystallinity (b) after the processing steps at a cooling rate of 1 °C/min; 0x: original material; 1x: once-processed materials; 2x: twice-processed (reprocessed) materials)

IV. Conclusions

Experiments were carried out to investigate the crystallization of different types of bio-based and petroleum-based polyesters at different cooling rates. Based on the measurement results the degree of undercooling and the crystalline fraction formed were determinate and compared between different polyester types and processing steps.

Our experimental results reveal that the both overcooling and crystallinity are logarithmically related to the cooling rate. By extrapolating the fitted functions, we determined the $\Delta T_{c,1}$ and $\Delta X_{m,1}$ value corresponding to a cooling rate of 1 °C/min. $\Delta T_{c,1}$ is related to the thermodynamic driving force for nucleation and its value depends mainly on the type of polyester: the highest for PET and the lowest for PBT. $\Delta X_{m,1}$ is primarily influenced by the crystal growth rate, which is connected to the that mobility or diffusion of molecular chains. For PET and PLA. for which reprocessing has caused significant degradation, this value varies greatly during the recycling steps: While in the case of PET, degradation during reprocessing reduces the crystallinity formed, PLA, on the contrary, increases the crystalline fraction. For PBS and PBT, no significant change in crystallinity is observed at low cooling rates.

AUTHOR CONTRIBUTIONS

Z. Taha Taha: Experiments.

A. Ádámné Major: Supervision, Review and editing.

F. Ronkay: Conceptualization, Analysis of the results.

Disclosure Statement

The authors declare that they have no known competing financial interests or personal relationships that could have appeared to influence the work reported in this paper.

ORCID

F. Ronkay: https://orcid.org/0000-0003-0525-1493

A. Ádámné Major: https://orcid.org/0009-0009-8546-718X

REFERENCES

[1] J. D. Reehard, Understanding Solids, the Science of Materials, Wiley Sons ltd, England, 2004.

[2] R. M. Wang, S. R. Zheng,Y. P. Zheng, Polymer matrix composites and technology, Woodhead Publishing and Science Press, 2011. https://doi.org/10.1533/9780857092229

[3] D. B. Harris, Engineering composite materials, The Institute of Materials, London, 1999. https://doi.org/10.1007/978-1-84882-831-5

[4] D. L. Chung, Composite Materials -Science and Applications, Engineering Materials and Processes, London, 2010. https://doi.org/10.1007/978-1- 84882-831-5

[5] W. D. Callister, Materials science and engineering, John Wiley & Sons, Inc, USA, 2006, https://doi.org/10.1007/BF01184995

[6] J. Scheirs, T. E. Long, Modern polyesters chemistry and technology of polyesters and copolyesters, Wiley series in Polymer Science, 2003.

[7] Q. Zhang, M. Song, Y. Xu, W. Wang, Z. Wang, L. Zhang, Bio-based polyesters: Recent progress and future prospects, Progress in Polymer Science 120 (2021) 101430. https://doi.org/10.1016/j.progpolymsci.2021.101430

[8] P. B. Yang, M. G. Davidson, K. J. Edler, S. Brown, Synthesis, Properties, and Applications of Bio-Based Cyclic Aliphatic Polyesters, Biomacromolecules, 2021. https://doi.org/10.1021/acs.biomac.1c00638

[9] M. Rabnawaz, I. Wyman, R. Auras, S. Cheng, A roadmap towards green packaging: current status and future outlook for polyesters in the packaging industry, Green Chemistry, 2017. https://doi.org/10.1039/x0xx00000x

[10] A. Larrañaga, E. Lizundia,, A review on the thermomechanical properties and biodegradation behaviour of polyesters, European Polymer Journal, Volume 121, December 2019, 109-296. https://doi.org/10.1016/j.eurpolymj.2019.109296

[11] R. Franz, F. Welle, Recycling of Post-Consumer Packaging Materials into New Food Packaging Applications—Critical Review of the European Approach and Future Perspectives, Sustainability 2022, 14, 824. https://doi.org/10.3390/su14020824

[12] V. Shanmugam, O. Das, R. E. Neisiany, K. Babu, S. Singh, M. S. Hedenqvist, F. Berto, S. Ramakrishna, Polymer Recycling in Additive Manufacturing: An Opportunity for the Circular Economy, Materials Circular Economy, 2020. https://doi.org/10.1007/s42824-020-00012-0

[13] B. Molnar, F. Ronkay, Effect of solid-state polycondensation on crystalline structure and mechanical properties of recycled polyethylene-terephthalate, Polymer Bulletin, 76, 2387–2398, 2019. https://doi.org/10.1007/s00289-018-2504-x

[14] D. Heidrich, M. Gehde, The 3-Phase Structure of Polyesters (PBT, PET) after Isothermal and Non-Isothermal Crystallization, Polymers, 14(4), 793, 2022. https://doi.org/10.3390/polym14040793

[15] M. C. Righetti, M. L. di Lorenzo, P. Cinelli, M. Gazzano, Temperature dependence of the rigid amorphous fraction of poly (butylene succinate). RSC Adv. 11, 25731–25737, 2021. https://doi.org/10.1039/D1RA03775G

[16] O. Mysiukiewicz, M. Barczewski, Crystallization of polylactide-based green composites filled with oil-rich waste fillers, Journal of Polymer Research 27: 374, 2020. https://doi.org/10.1007/s10965-020-02337-5

[17] S. Saeidlou, M. A uneault, C. B. Li H.,Park, Poly(lactic acid) crystallization, Progress in Polymer Science, Volume 37, Issue 12, Pa 1657-1677,2012. https://doi.org/10.1016/j.progpolymsci.2012.07.005

[18] P. C. Zilanova, S. M. Ribas, G. M. Guzman, Isothermal crystallization of poly(ethylene-terephthalate) of low molecular weight by differential scanning calorimetry: 1. Crystallization kinetics, Polymer, volume 26, Issue3, Pages 423-428, 1985. https://doi.org/10.1016/0032-3861(85)90205-8

[19] M. L. Di Lorenzo, C. Silvestre, Non-isothermal crystallization of polymers, Progress in Polymer Science, 1999, Vol. 24, No. 6, pp. 917–950. https://doi.org/10.1016/S0079-6700(99)00019-2

[20] A. Mehta, U. Gaur, B. Wunderlich, Equilibrium melting parameters of poly (ethylene terephthalate), Journal of Polymer Science: Polymer Physics Edition, Vol. 16, 289-296,1978. https://doi.org/10.1002/pol.1978.180160209

[21] D. Heidrich, M. Gehde, Calorimetric analysis of the crystallization of PBT considering the dynamic cooling condition of real processing, Polymer Testing, Volume 85, May 2020, 106459. https://doi.org/10.1016/j.polymertesting.2020.106459

[22] R. Androsch, K. Jariyavidyanont, A. Janke, C. Schick, Poly (butylene succinate): Low-temperature nucleation and crystallization, complex morphology and absence of lamellar thickening, Polymer, Volume 285, 126311, 2023. https://doi.org/10.1016/j.polymer.2023.126311

[23] V. M. Nadkarni, N. N. Bulakh, J. P. Jog, Assessing polymer crystallizability from nonisothermal crystallization behavior, Advances in Polymer Technology, Vol. 12, No. 1, 73-79, 1993. https://doi.org/10.1002/adv.1993.060120107

ACTA TECHNICA JAURINENSIS
Vol. 17, No. 1, pp. 8-21, 2024
10.14513/actatechjaur.00726

Use of Zero-crossings Segmentation for Track Quality Assessment

Abdaljbbar B. A. Dawod[1,*], **György Terdik**[2]

[1] Doctoral School of Informatics, University of Debrecen, 4032 Debrecen, Egyetem tér 1., Hungary
[2] Department of Information Technology, Faculty of Informatics, University of Debrecen, 4032 Debrecen, Egyetem tér 1., Hungary
[*] email: abdaljbbar@gmail.com

Submitted: 13/11/2023 *Accepted: 27/12/2023* *Published online: 17/02/2023*

Abstract: This study concerns track quality assessment of standard-gauge railways in the context of the Hungarian railway system. Data gathered by multipurpose track recording vehicles matched the EN 13,848 requirements. Track Quality Index (TQI) measurement systems (The Federal Railroad Administration (FRA), the Netherlands', and the Chinese TQI) are considered where three types of predetermined segment techniques: separate, moving, and Zero-crossings segmentation are employed. The importance of track segmentation in quality assessment, which affects maintenance planning, is shown by key findings. For heterogeneous data, the TQIs might be deceptive, highlighting the need for alternatives. The robustness of the Zero-crossings method makes it possible to analyze deterioration factors in great detail and in some efficient way. Longer analytical segments and smoothing of the data improved precision. Based on empirical data, we advise considering a Zero-crossings strategy for precise and efficient track-quality evaluations. With the help of this study, track quality can be better evaluated for train systems.

Keywords: *Track Quality Indices, Track geometry, Signal processing, Zero-crossing, Empirical Mode Decomposition, FRA Geometry TQI, Netherlands TQI, Chinese TQI*

I. Introduction

In the era of high-speed railway systems, the railway track is considered a main pillar for safety and train punctuality. Using total quality management in railway maintenance has led practitioners to find better ways to manage railway assets more efficiently and cost-effectively [4, 6, 20]. Predicting degradation plays a pivotal role in formulating inspection and maintenance strategies. Monitoring the condition of railway tracks is essential to uphold the efficiency of infrastructure assets [22]. When a geometric track indicator approaches the established legal limit, it signifies the necessity for maintenance intervention. These actions are undertaken to minimize or prevent potential failures, ensuring the restoration of any malfunctioning railway components to an operational condition.

Railway track geometry includes 4 main parameters: 1) Longitudinal level: the concept refers to how much the running table level differs from a smoothed vertical position (reference line) within specific wavelength ranges. 2) Alignment: the concept pertains to how much the rail deviates laterally from a smoothed reference line within specific wavelength ranges. 3) Track gauge: the closest distance between the inner edges of the rail heads, measured slightly below the rail surface within a range of 0–14 mm. 4) Cross level: difference in the height of the adjacent running tables. For more details, the reader refers to [2, 6, 10]. In addition sensitive wavelengths of the track, irregularities have been considered by [7].

The track is divided into segments to evaluate railway track conditions based on track geometry, and the quality is assessed for each segment. Track Quality Indices summarize this assessment (TQI), which are preferred methods for comprehensively evaluating railway track conditions. TQIs are valuable for assessing track performance, planning interventions, and comparing track performance before and after modifications. Two decades ago, [11] identified that the segmentation approach used for TQI calculations is characterized as linear track geometry measurements with consistent attributes related to factors influencing track geometry degradation.

Paper [13] used simulated results to show that various TQIs are specified for track segments of varying lengths, typically categorized as 3–25 me-

ters, 25–70 meters, and 70–200 meters in length. The 200-meter long segment is the most commonly employed, although in certain instances, a specific track or even the entire network is assessed using just a single TQI value [23]. Recently, two approaches have been proposed to define the railway track segments, where both approaches have generated variable segment lengths along the railway track. The first approach relied on the specific type of track construction in use [12] and the second was based on the horizontal elements of track alignment (straight, curve, and curve with transition curve segments) [28]. Additionally, more recent research highlights the importance of considering not only technical factors but also economic and operational aspects when deciding on track segment lengths for maintenance purposes [21]. Although emerging technical factors and economic and operational aspects become crucial when deciding on track segment lengths, the statistical properties of the collected measurements should be treated carefully. The need to evaluate railway track quality to plan repairs is emphasized in [26], with a focus on the objective of preserving stable track geometry. The paper looked at the efficiency of remedial maintenance and the rates of track deterioration on a regional railroad. Also, to identify critical elements for sustainable development, [5] investigated actual measurement data of six geometric parameters of continuously welded rail (CWR). According to their results, vertical irregularities are important in the vertical plane (V-plane), but the track gauge gradient and horizontal irregularities are crucial in the horizontal plane (H-plane). These factors become more intense, particularly in curved sections, necessitating more frequent maintenance. In light of the increasing importance of rail as a sustainable mass transit alternative, the study findings offer a foundation for efficiently regulating the life cycle of CWR to advance sustainability.

Zero-crossings is a powerful tool for analyzing time series data, it can be used to characterize oscillatory patterns, extract useful information about the signal, and develop signal processing applications [3, 15]. Besides that, it can be used for non-Gaussian mixtures and products of Gaussian processes as well. Based on the information gathered by the authors, it can be deduced that there exists no substantial contribution aimed at improving railway track segmentation based on Zero-crossings.

This research aims to propose the Zero-crossings methodology as a possible way of railway track segmentation, evaluating the overall quality of individual track segments, and establishing management criteria based on the proposed approach. Time series and signal processing techniques will be applied since the measurements are very similar in nature to observations in time. The rest of the article is organized as follows. The materials and methods are introduced in Section II, and the results of the Hungarian State Railway are summarized in Section III, a track section of 5,900 meters serves as an example for illustration of our work, without keep mentioning it. Then, in Section IV, the results have been discussed thoroughly. Finally, Section V gives the main conclusions.

II. METHODOLOGY

Various countries have made efforts to customize their version of the TQI. For instance, in China, the TQI is based on the standard deviations of 7 types of track measurements. In the United States, the ratio of traced space curve length to track segment length is used. Polish J-synthetic coefficient based on standard deviation is used to assess the Polish Railways. India has its track geometry index formula, which focuses on standard deviations of geometry parameters over 200-meter segments. A detailed discussion of some approaches is shown in the following subsections.

1. FRA Geometry TQI

Federal Railroad Administration developed a length-based method to calculate the TQI_F of a given segment of the data for gauge, alignment, and longitudinal level, say [6]. Let x_k denote the sampling points and y_k the measurements. The formula of TQI_F is the following

$$TQI_F = 10^6 \left(\frac{\ell_s}{\ell_0} - 1 \right), \tag{1}$$

where ℓ denotes the theoretical length (in mm), in particular $\ell_0 = \sum_{k=1}^{n_0} \Delta x_k$, and ℓ_s is the traced length of the space curve of a track segment including n_0 measurements, i.e. $\ell_s = \sum_{k=1}^{n_0} \sqrt{\Delta y_k^2 + \Delta x_k^2}$. Here Δy and Δx are the differences between two consecutive measurements in the sample space, respectively. We consider equidistant measurements where $\Delta x_k = h$ therefore

$$TQI_F = 10^6 \left(\frac{1}{n_0} \sum_{k=1}^{n_0} \sqrt{\left(\frac{\Delta y_k}{h} \right)^2 + 1} - 1 \right).$$

Some other railway administrations use TQI which combines two or more geometrical parameters into a single measure of ride quality.

2. Netherlands Track Quality Index

The Netherlands Q index proposes a more universal form of quality index across different classes of

railway tracks [16], [23]. This index considers the standard deviation of a particular quality parameter for a specific track segment. It compares it to the 80% quantile of the standard deviations of that parameter across all track segments. The Q index spans from 0 to 10. A higher Q index indicates improved track quality for a 200-meter track segment

$$TQI_N = 10 * 0.675^{\sigma_k/\sigma_{80,\bullet}}. \tag{2}$$

Where σ_k is the standard deviation for the quality parameter, and $\sigma_{80,\bullet}$ represents 80^{th} percentile of standard deviations of all segments in the maintenance section ranging from 5 to 10 km.

3. Chinese Track Quality Index

Chinese national railroads use the sum of standard deviations σ_k of seven quality parameters to assess the overall track quality of a track segment [8]. It is calculated by

$$TQI_C = \sum_{k=1}^{7} \sigma_k. \tag{3}$$

Two possible lengths of the overall track quality assessment are 200 m and 500 m. The first is applied to conventional railway lines and the second is usually applied to high-speed railroads. The segment is considered worse in the overall track quality as the TQI_C value increases.

4. European Standard EN 13848-5

European Standard is also monitoring the railway track geometry. Longitudinal level, alignment, and gauge are the key track geometry parameters that one evaluates. The mean value determines gauge irregularities over a 100-meter segment while longitudinal level and alignment are assessed by analyzing the standard deviation of irregularities in a 200-meter segment. European Standard provides the permissible thresholds for geometry parameters [1, 4, 10]. The permissible thresholds are given in **Table 1**.

5. Zero-crossings approach

In the literature, the most straightforward procedure of track segmentation is to divide the whole railway track into equally-length segments. The length is usually chosen according to the train's speed, either 200 m or 500 m [23, 27]. However, although the fixed segment length is easier to construct and measure the railway efficiency sometimes it might be misleading where the measurements in the same segment might be heterogeneous. Recently, [18] investigated the impact of changing the segment length to assess railway track quality. They evaluated analytical segments of various lengths, including 200 meters, 100 meters, 50 meters, and 25 meters. The comparative assessment of the calculations for TQIs revealed that decreasing the segment length led to an enhancement in the resolution of the track quality analysis. [21] used the linear regression function and demonstrated its aptness in characterizing track quality between two tamping tasks and exhibited superior accuracy in forecasting future track quality.

Our approach is based on the idea that two consecutive zero observations define the most important changes in the railway track. Since the distortion is restarting from zero at each time. The Zero-crossings in a series of measurements are the points where the signal changes from positive to negative or vice versa. **Fig. 1** illustrates the idea of Zero-crossings as the blue dots show the point where the sign has been changed. The signal crosses the zero line (red) at the blue points. Zero-crossings are a

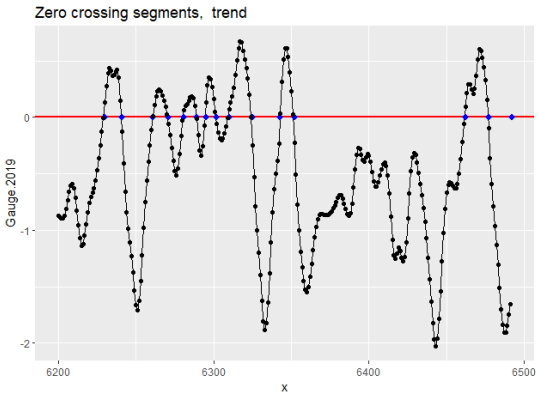

Figure 1. *Example for zero-crossings of the denoised (by EMD) Gauge 2019 (mm) in terms of measurement numbers.*

powerful tool for analyzing a series of data, they can be used to characterize oscillatory patterns in time series data in particular providing a robust approach to the detection of periodic autocorrelation, [19]. It gives useful information about the signal and base for signal processing applications [15, 24]. It is worth noting that the lengths of zero-crossing segments are not fixed and the data included in different segments can be considered independent.

Zero-crossings method

Consider that we have data sampled over time or space, let $X_s, (s = 1, 2, \ldots, N)$ denote the corresponding stochastic series. We define zero-crossings for observations in equidistant distances. Let the associated (to X_s) clipped binary series Y_s

Table 1. *Difference limit between the specified gauge and mean gauge over 100 m segment (in mm)*

	Mean Gauge threshold			Standard deviation threshold	
Speed (km/h)	Safety limits	Intervention limits	Alert limit	Longitudinal level	Alignment
80-120	[-7, +27]	[-6, +25]	[-5, +22]	1.8-2.7	1.2-1.5
120-160	[-5, +20]	[-4, +18]	[-3, +16]	1.4-2.4	1.0-1.3
160-220	[-5, +20]	[-4, +18]	[-3, +16]	1.2-1.9	0.8-1.1
220-300	[-5, +20]	[-4, +18]	[-3, +16]	1.0-1.5	0.7-1.0

defined by

$$Y_s = \begin{cases} 1, & X_s \geq 0, \\ 0, & X_s < 0, \end{cases} \qquad s = 1,2,\ldots,N,$$

and let d_s be the indicator function at distance s

$$d_s = (Y_s - Y_{s-1})^2, \quad s \geq 2$$

Now, d_s is 0 or 1. When $d_s = 1$ we say that a zero-crossing occurs at distance s. The number of zero-crossings in $X_1, X_2, \ldots X_N$ is denoted by D_X and is defined by the sum

$$D_X = \sum_{s=2}^{N} d_s.$$

The expected number of zero-crossings D_X per unit distance can be calculated for a Gaussian stationary series by the formula

$$\mathrm{E}D_X = \frac{N-1}{\pi} \arccos \rho_1, \tag{4}$$

where ρ_1 is the autocorrelation of X_s at lag 1, see [14]. It will be clear later that the assumption of zero mean and Gaussian stationarity does not fulfill our data nevertheless the formula (4) provides some basic information.

Table 2 shows that although the formula (4) is not applicable precisely there is some clear connection between the observed number of zero crossings *nZC* and the theoretical values *nZCth* of it. The column $nZC/nZCth$ points out the dependence on the mean μ, since the zero mean is assumed for the formula (4). After we have centered the series column $nZC0^*$ became really close to theoretical values, see column $\%nZC0/nZCth$. Nevertheless, we are interested in the zero-crossing segments of the non-centered data and use the formula (4) for the orientation of the investigation.

6. EMD and trend

We consider the Empirical Mode Decomposition (EMD) as a possible tool for preliminary transformations for non-stationary, non-Gaussian data, moreover which is not smooth enough. EMD is a data-driven auto-adaptive method, which decomposes signals into components referred to as Intrinsic Mode Functions (IMF) and a residual. IMFs are satisfying the following conditions: (i) In the whole dataset, the number of extrema and the number of zero crossings must either equal or differ by at most one; (ii) at any point, the mean value of the envelope defined by the local maxima and the envelope defined by the local minima is zero, [9]. The construction of IMFs is not unique. In our calculations, we apply the R package Rlibeemd using the so-called sifting process method, see [9], [17]. One of the advantages of EMD is that the modes (IMFs) are orthogonal. The sum of all modes and the remaining residual resemble the original signal. The IMFs fluctuated around zero. The only non-zero mean component is the remaining residual. An IMF represents a simple oscillatory mode. It has been noticed [25] that the frequency bandwidths tend to reduce as the number of IMFs increases.

We are interested in the decomposition of a signal into a possible continuous deterministic trend and an additive noise since the result of the changes of the railway track should be a smooth signal i.e. there are no sudden changes except the noise of the measurement. The trend can serve as the nonlinear smooth signal and the additive noise as the stationary Gaussian process. The separation of the signal to the trend and noise has been considered by [29]. The methodology is the following: consider the correlations of the marginal Hilbert spectrum for two consecutive IMFs then starting from the first IMF $u_1(t)$, check step by step if the modulus of correlation is smaller than an ε (typically $\varepsilon = 0.2$). The separation before and after that stopping order p_0 say, provides the decomposition of the signal into noise which is the sum of IMFs: $W(t) = \sum_{k \leq n_0} u_k(t)$ and the trend $X(t) - W(t)$. In our case, we have $p_0 = 2$ for Gauge 2019. One observes that the outliers are included in the noise but the residual, which is considered a nonlinear trend.

Fig. 3 shows an example where the observation X_{13710} has neighbors with significantly different values. Therefore it should be considered to be an outlier. The trend (EMD residual) smooths the observations.

III. RESULTS

A formal analysis has been conducted to compare the effectiveness of segmentation by Zero-crossings

Table 2. *Number of zero crossing segments for data Gauge 2019, in mm.*

Type	Year	nZC^*	$nZCth^*$	$\%\ nZC/nZCth$	μ	$nZC0^*$	$\%\ nZC0/nZCth$
Gauge	2017	1245	1892	66	-1.13	1794	95
	2018	1553	1930	80	-0.76	1812	94
	2019	1528	1893	81	-0.73	1782	94
	2020	1387	1805	77	-0.96	1748	97
Left	2017	1398	1619	86	-0.45	1598	99
	2018	1506	1568	96	0.43	1634	104
	2019	1369	1523	90	-0.50	1565	103
	2020	1515	1529	99	-0.42	1575	103
Right	2017	1604	1634	98	-0.30	1686	103
	2018	1327	1578	84	0.57	1575	100
	2019	1517	1528	99	-0.32	1531	100
	2020	1471	1531	96	-0.33	1561	102

**We have denoted the number of zero crossings segments of the data: nZC, estimated by the formula (4): nZCth, percentage: $nZC/nZCth$, mean: μ, in mm, number of zero crossing segments for centered data: $nZC0^*$, percentage: $\%nZC0/nZCth$.*

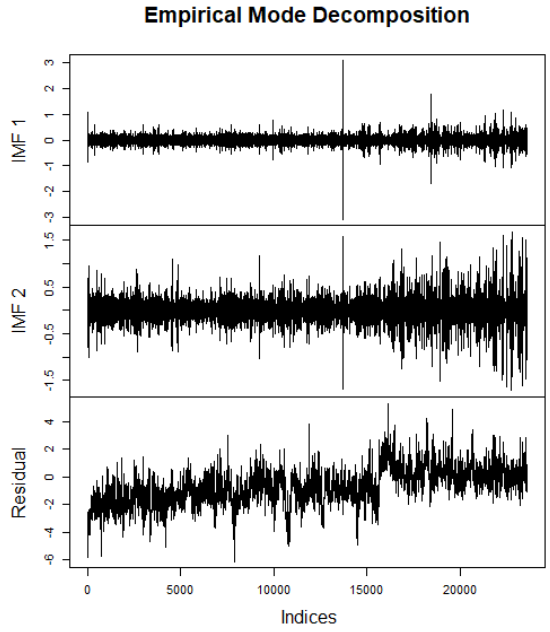

Figure 2. *EMD, data Gauge 2019, in mm.*

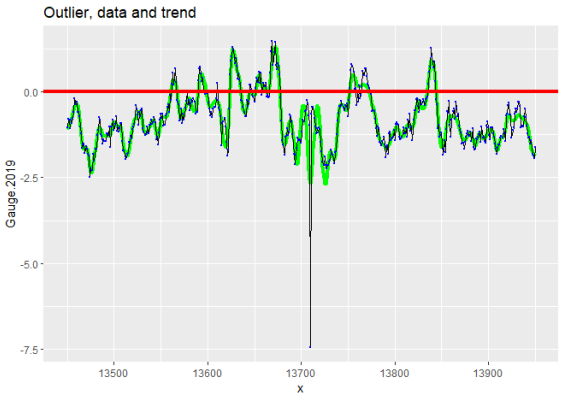

Figure 3. *Data Gauge 2019, in mm,(black) and trend, i.e. denoised data generated by EMD (green). Outlier: $X_{13710} = -7.43$ in between $X_{13709} = -0.97$, and $X_{13711} = -0.65$, (indices denote the measurement numbers).*

and fixed-length segmentation. MÁV CRTI Ltd. (Hungarian State Railways Central Track Inspection Ltd., Budapest, Hungary) provided a local gauge narrowing fault dataset obtained from their measurements by a versatile Track Recording Vehicle (TRV). The TRV operated at an average speed of 160 km/h, and track irregularity data was meticulously sampled at 0.25-meter intervals along the railway track. We have considered the dataset comprised four years, from 2017 to 2020, and was sourced from diverse segments of railway lines in Hungary. We consider a specific choice of a track section spanning measurements including a chain 5,900 m. The primary focus of the inquiry is on specific track geometry parameters, including measurements of the track gauge (mm) and alignment (mm) of both the right and left rails. The surveyed railway maintains straight-line geometry within each year.

1. Basic statistics

The primary objective of our statistical methodology is to examine and elucidate the location and variability characteristics of our railway dataset and to assess and describe the skewness and kurtosis parameters.

Table 3 provides a summary of the statistical data related to track gauge measurements and left and right rail alignments, and categorizes the defined railway sections by years. The results of the Hungarian railway measurements meet or exceed the established EU benchmarks, as stated in [2], which are consistent with EU standards. The statistical

Table 3. *Summary statistics of the railway geometrical parameters, including gauge (mm), left, and right alignments (mm), were measured over a period of four years.*

Type	Year	Mean	Var	Corr. matrix				Min	Max	Skewness	Kurtosis
				2017	2018	2019	2020				
Gauge	2017	-1.13	1.58	1.00	0.46	0.52	0.58	-6.70	4.86	-0.04	0.87
	2018	-0.76	1.60	0.46	1.00	0.51	0.51	-6.06	5.02	0.05	0.59
	2019	-0.73	1.68	0.52	0.51	1.00	0.63	-6.03	5.18	0.05	0.65
	2020	-0.96	1.81	0.58	0.51	0.63	1.00	-6.79	4.91	0.01	0.76
Left	2017	-0.45	1.61	1.00	0.02	-0.05	-0.02	-5.92	4.74	-0.05	0.59
	2018	0.43	1.72	0.02	1.00	-0.16	0.07	-5.05	5.57	-0.03	0.58
	2019	-0.50	1.96	-0.05	-0.16	1.00	-0.12	-6.42	5.21	-0.07	0.69
	2020	-0.42	1.88	-0.02	0.07	-0.12	1.00	-6.95	7.51	-0.04	1.41
Right	2017	-0.30	1.32	1.00	-0.00	0.02	0.04	-7.63	4.48	-0.08	0.90
	2018	0.57	1.45	-0.00	1.00	-0.19	0.03	-6.86	5.57	-0.09	0.77
	2019	-0.32	1.66	0.02	-0.19	1.00	-0.14	-7.72	6.01	-0.09	0.85
	2020	-0.33	1.61	0.04	0.03	-0.14	1.00	-6.78	7.90	0.01	1.37

properties of the gauge look different from those of alignments. The correlation matrix shows that the dependence during the years does not change too much. The skewness of every variable is small it refers to the symmetry of the distributions. All kurtosis suggests the non-normality of the variables. **Fig. 4** illustrates in agreement with **Table 3** (non-zero positive kurtosis values) that the distributions of data exhibit a greater degree of peakedness than a normal distribution should. We note that all the above statistical statements should be tested, here we spare some room not to do so. The autocorrelation function (ACF) analysis revealed non-stationarity within the data, see **Fig. 5**.

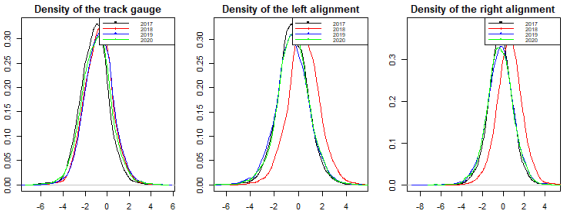

Figure 4. *The distribution of the Hungarian railway track geometry measurements over the different years.*

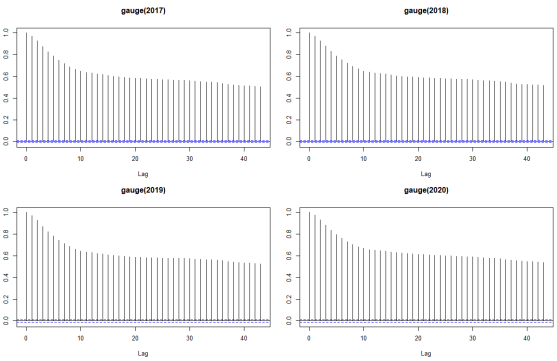

Figure 5. *ACF plots for the gauge measurements.*

As it has been shown trimming necessarily follows from the smoothness of the rail track but it should not affect the mean, say. The EMD method provides the trend (nonlinear) which can be used for smoothing the data. Another simpler method is the moving average of consecutive values. **Fig. 6** implies that although the trend is smoother nevertheless the moving averages of three consecutive values (MA3) do the job as well. Therefore from now on we shall use MA3 smoothed data for our analysis.

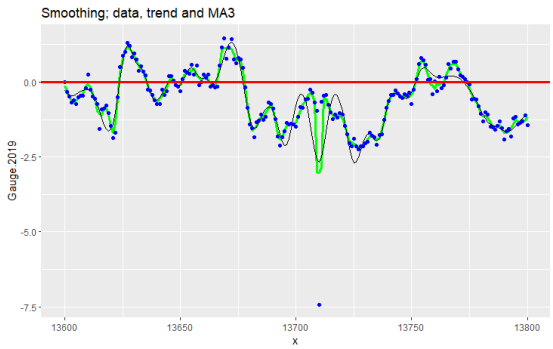

Figure 6. *Data Gauge 2019, in mm: data (blue dots), EMD trend (black), and smoothed data by MA3 (green), by observation numbers.*

We note an additional property of the measurements arising from the railway track which is the reversibility i.e. the signal is invariant under reversing the starting and ending point of the process. It also reserves some methodologies for the future.

2. TQI for quality assessment

This study aims to evaluate the effectiveness of the TQI techniques when applied to the data from the Hungarian railway system by considering various segment-length strategies. Now we are given the array of railway track quality assessment method-

ologies introduced in Section II. To this end, two distinct segment lengths, 100 and 200 meters, are employed by the guidelines provided by the Federal Railroad Administration for calculating TQI_F. Moreover, both the discrete segmentation approach (i.e., split the entire length of the railroad track into equal L_0 distances) and the continuous moving segmentation approach (i.e., use a moving window of size L_0, recursively selecting segments of length L_0 from the whole railway track) were utilized to select the segment measurements.

The adoption of these two lengths ensures the availability of at least one zero-crossing segment for comparative analysis. The resulting calculations are presented in **Tables 4, 5** and **6**, which provide the top five maximum TQI_Fs values using discrete segmentation ($L_0 = 400$ and 800) and discrete-moving segmentation approaches, respectively. From now on L_0 denotes the number of measurements included in segments.

Table 4 presents an array of distinct railway track segments, accompanied by their respective TQI_F values spanning 2017, 2018, 2019, and 2020. The table evaluates three critical railway track geometry parameters: Gauge, Left alignment, and Right alignment. Within the table, the "Segment" column specifies the particular section of the railway track under scrutiny, with the numbers in parentheses designating the commencement observation points for these segments.

It is essential to note that lower TQI_F values indicate improved track conditions, whereas elevated values may suggest potential issues or track degradation, as established by [6]. Examining the results, a discernible trend emerged, wherein the track gauge consistently exhibited the highest TQI_F values, particularly in 2019, followed by 2017 and 2020. In contrast, the TQI_Fs for the left and right alignments consistently registered lower values when compared to the gauge. Consequently, it is apparent that the gauge parameter exhibits heightened sensitivity to railway degradation, necessitating periodic decision-making in the context of track maintenance and management. A graphical summary of the calculated TQI_Fs employing the distinct segmentation approach is shown in **Fig. 7**. One can read from **Fig. 7** the yearly change in the quality of TQI_F .

Using a formal tone, the authors report that their findings in **Table 6** support the conclusions drawn from their earlier analysis using the distinct segmentation approach. The track gauge consistently exhibited the highest TQI values, with notable prominence in 2019. To further elucidate the factors contributing to the elevated TQI_Fs observed in 2019, the authors conducted a deeper investigation and found that certain measurements deviated significantly from the expected pattern. For example, measurement number 13710 registered a value of -7.43, **Fig. 3**. Given the continuous nature of the observations, outliers in TQI_F values can potentially introduce misleading interpretations without smoothing the data. Segment no. 17 with $L_0 = 800$ (200m) and measurements $X_{13601:14400}$ includes 32 zero-crossing segments and one of them has a larger length than 25 m with TQI_F value 0.0632. At the same time, the TQI_F value of this segment is 1.5305 and the TQI_F value for the same segment of the trend is 0.1693, **Fig. 6**.

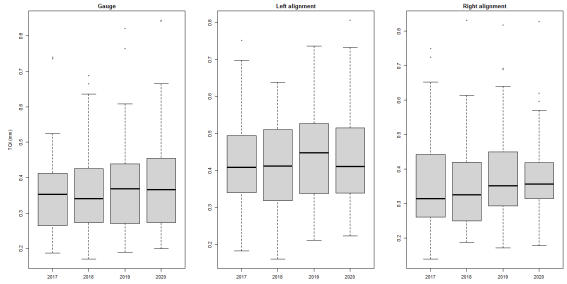

Figure 7. *Summary plot of TQI_F values per segment of the track geometry parameters. ($L_0 = 400$)*

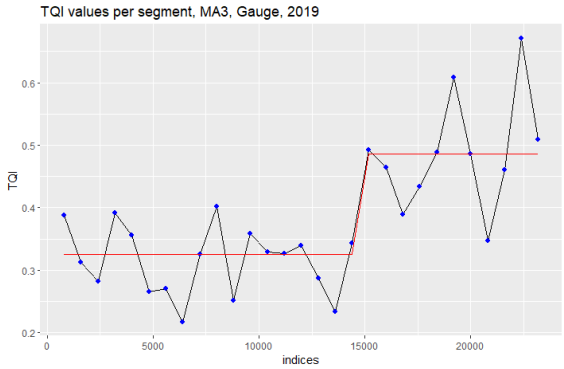

Figure 8. *TQI_F Variations for the Track Gauge with change point detection (red), MA3, by 200 m in the Year 2019, indices refer to the measurement numbers.*

IV. Discussion

The aforementioned section highlights the significance of theoretical segment length on the computed TQI, resulting from diverse TQI methodologies. The following subsections will discuss the findings in detail.

1. Federal Railroad Administration, TQI_F

To evaluate the efficacy of the FRA TQI under various segmentation approaches, **Tables 4** through **7**, along with **Fig. 7**, provide insights into its

Table 4. *Maximum TQIs for the associated segments for the railway geometrical parameters with length 100 m, $L_0 = 400$.*

		2017		2018		2019		2020	
		Segment	TQI_F	Segment	TQI_F	Segment	TQI_F	Segment	TQI_F
Gauge	1	47 (18401)	0.74	55 (21601)	0.69	55 (21601)	0.82	55 (21601)	0.84
	2	55 (21601)	0.73	46 (18001)	0.66	47 (18401)	0.76	47 (18401)	0.84
	3	46 (18001)	0.52	57 (22401)	0.64	49 (19201)	0.61	57 (22401)	0.66
	4	38 (14801)	0.52	47 (18401)	0.54	57 (22401)	0.59	49 (19201)	0.60
	5	49 (19201)	0.52	44 (17201)	0.53	54 (21201)	0.56	56 (22001)	0.60
Left	1	39 (15201)	0.75	11 (4001)	0.64	39 (15201)	0.74	39 (15201)	0.80
	2	19 (7201)	0.70	19 (7201)	0.64	20 (7601)	0.68	31 (12001)	0.73
	3	20 (7601)	0.70	38 (14801)	0.63	31 (12001)	0.67	20 (7601)	0.72
	4	11 (4001)	0.64	44 (17201)	0.62	44 (17201)	0.65	19 (7201)	0.67
	5	56 (22001)	0.63	7 (2401)	0.58	19 (7201)	0.63	37 (14401)	0.65
Right	1	56 (22001)	0.75	39 (15201)	0.83	39 (15201)	0.82	39 (15201)	0.83
	2	39 (15201)	0.72	55 (21601)	0.61	47 (18401)	0.69	30 (11601)	0.62
	3	54 (21201)	0.65	52 (20401)	0.61	54 (21201)	0.69	47 (18401)	0.60
	4	47 (18401)	0.65	56 (22001)	0.58	56 (22001)	0.64	54 (21201)	0.57
	5	52 (20401)	0.62	54 (21201)	0.57	52 (20401)	0.63	31 (12001)	0.54

**The term "Segment" refers to the section of the railroad track with length L_0 that contains the measurements in the order beginning with the measurement in the bracket.*

Table 5. *Maximum TQIs for the associated segments for the railway geometrical parameters with length 200 m, $L_0 = 800$.*

		2017		2018		2019		2020	
		Segment	TQI_F	Segment	TQI_F	Segment	TQI_F	Segment	TQI_F
Gauge	1	28 (21601)	0.61	28 (21601)	0.60	28 (21601)	0.67	28 (21601)	0.72
	2	24 (18401)	0.55	29 (22401)	0.58	24 (18401)	0.61	24 (18401)	0.65
	3	23 (17601)	0.51	23 (17601)	0.54	29 (22401)	0.51	29 (22401)	0.54
	4	19 (14401)	0.47	24 (18401)	0.50	19 (14401)	0.49	23 (17601)	0.51
	5	20 (15201)	0.46	19 (14401)	0.47	23 (17601)	0.49	19 (14401)	0.51
Left	1	10 (7201)	0.70	10 (7201)	0.61	10 (7201)	0.65	10 (7201)	0.70
	2	20 (15201)	0.62	19 (14401)	0.58	20 (15201)	0.63	20 (15201)	0.66
	3	6 (4001)	0.61	5 (3201)	0.56	6 (4001)	0.59	19 (14401)	0.61
	4	19 (14401)	0.57	28 (21601)	0.53	5 (3201)	0.58	6 (4001)	0.59
	5	28 (21601)	0.54	6 (4001)	0.53	19 (14401)	0.57	16 (12001)	0.54
Right	1	28 (21601)	0.64	28 (21601)	0.60	28 (21601)	0.64	20 (15201)	0.66
	2	20 (15201)	0.61	20 (15201)	0.54	20 (15201)	0.62	28 (21601)	0.48
	3	27 (20801)	0.57	27 (20801)	0.53	24 (18401)	0.59	24 (18401)	0.47
	4	24 (18401)	0.55	24 (18401)	0.51	27 (20801)	0.58	15 (11201)	0.47
	5	26 (20001)	0.48	23 (17601)	0.49	26 (20001)	0.50	27 (20801)	0.46

**The term "Segment" refers to the section of the railroad track with length L_0 that contains the measurements in the order beginning with the measurement in the bracket.*

performance. These findings underscore the effectiveness and reliability of the approach across diverse segmentation scenarios.

Tables 4, 5 and **6** provide valuable insights into the vulnerability of the Federal Railroad Administration approach when applied in conjunction with the distinct and moving segmentation methods. These findings underscore its susceptibility to influence by outliers, consequently yielding potentially misleading Track Quality Index (TQI) values. A notable illustration of this susceptibility was observed in the context of track gauge measurements in 2019, where the presence of a few outliers had a considerable impact. This is evident when comparing the moving TQI_F values for the gauge measurements in 2019 with their trimmed counterparts (the trimmed counterpart is derived from the original measurements after applying the moving average, MA3, method).

Furthermore, **Table 6** highlights the maximum TQI_F values obtained using the moving segmentation approach under the different lengths ($L_0 = 400$ and 800). Notably, these segments exhibit a con-

Table 6. *Maximum moving TQIs for the associated segments for the railway geometrical parameters with lengths 100 m and 200 m.*

		$L_0 = 400$		$L_0 = 800$	
	Year	segment*	max	segment	max
Gauge	2017	18281	0.79	22797	0.65
	2018	23170	0.86	22692	0.67
	2019	21497	0.86	21501	0.71
	2020	18252	0.88	21521	0.75
Left	2017	7380	0.83	7182	0.71
	2018	7264	0.80	7022	0.68
	2019	7346	0.86	7120	0.71
	2020	7363	0.90	7158	0.74
Right	2017	15302	0.87	15030	0.69
	2018	15182	0.85	14910	0.68
	2019	15243	0.91	14979	0.74
	2020	15250	0.96	15007	0.77

**Segment represents the part of the railway track that contains the sequence of measurements starting with the given observation of length L_0.*

Table 7. *TQI_F values under Zero-crossings segmentation with number of measurements exceeding the lengths of 25 m and 50 m.*

			$L_0 = 100$		$L_0 = 200$		
Parameter	Year	Segment	Start at	TQI_F	Segment	Start at	TQI
Gauge	2017	87	7622	0.59	313	15318	0.46
	2018	578	17593	0.79	3	411	0.36
	2019	504	16415	0.71	642	18082	0.39
	2020	373	14468	0.52	413	15287	0.51
Left	2017	324	5583	0.11			
	2018	1205	22253	0.36			
	2019	421	7939	0.30			
	2020	1185	22167	0.47			
Right	2017	1306	22187	0.23			
	2018	1073	22254	0.28			
	2019	1213	22128	0.28			
	2020	734	14425	0.26			

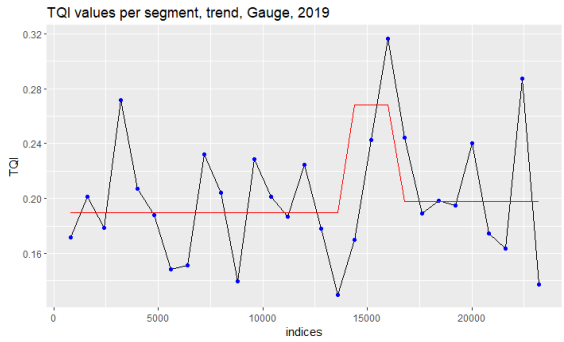

Figure 9. *TQI_F Variations for the Trend of Track Gauge with change point detection (red) by 200 m in the Year 2019, indices refer to the measurement numbers.*

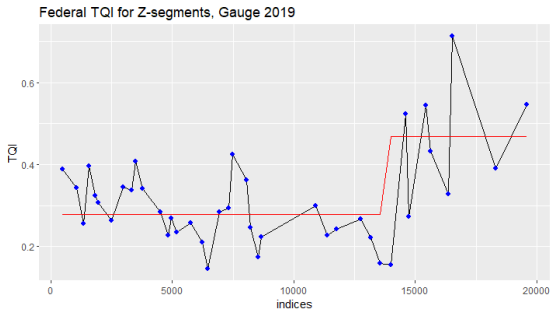

Figure 10. *TQI_F Variations for Z-segments with lengths greater than 25 m of Track Gauge (mm) in the Year 2019, and change point detection (red), indices refer to the measurement numbers.*

secutive pattern, with the difference between them typically amounting to a single measurement. Consequently, it is apparent that the distinct segmentation approach represents a special case within the framework of the moving segmentation approach, wherein the maximum TQI_F value achieved under the distinct segmentation approach does not surpass the TQI_F values obtained through the moving segmentation approach.

Table 8. *Minimum Netherlands Q indices with lengths 100 m and 200 m.*

	$L_0 = 400$						$L_0 = 800$					
	Gauge		Left		Right		Gauge		Left		Right	
Year	Segm.	TQI_N	Segm.	TQI_N	Segm.	TQI_N	Segm.	TQI_N	Segm.	TQI_N	Segm.	TQI_N
	1 28 (10801)	5.45	56 (22001)	5.75	56 (22001)	5.11	20 (15201)	6.06	28 (21601)	6.28	28 (21601)	5.65
	2 50 (19601)	5.86	37 (14401)	5.89	54 (21201)	6.11	14 (10401)	6.30	19 (14401)	6.31	27 (20801)	6.21
2017	3 32 (12401)	5.93	39 (15201)	6.31	39 (15201)	6.30	10 (7201)	6.37	16 (12001)	6.32	20 (15201)	6.47
	4 20 (7601)	5.94	32 (12401)	6.39	52 (20401)	6.31	19 (14401)	6.47	20 (15201)	6.53	26 (20001)	6.54
	5 40 (15601)	6.06	31 (12001)	6.45	53 (20801)	6.40	25 (19201)	6.66	6 (4001)	6.70	24 (18401)	6.54
	1 27 (10401)	5.95	56 (22001)	5.69	56 (22001)	5.29	20 (15201)	5.52	28 (21601)	6.09	28 (21601)	5.66
	2 49 (19201)	5.95	34 (13201)	6.17	34 (13201)	6.12	10 (7201)	6.18	14 (10401)	6.29	27 (20801)	6.42
2018	3 32 (12401)	6.14	36 (14001)	6.28	55 (21601)	6.22	14 (10401)	6.29	16 (12001)	6.48	26 (20001)	6.58
	4 20 (7601)	6.20	27 (10401)	6.32	53 (20801)	6.33	16 (12001)	6.40	18 (13601)	6.60	14 (10401)	6.64
	5 9 (3201)	6.24	49 (19201)	6.42	52 (20401)	6.42	19 (14401)	6.44	17 (12801)	6.61	17 (12801)	6.68
	1 27 (10401)	5.88	56 (22001)	5.61	56 (22001)	5.26	20 (15201)	5.89	28 (21601)	6.12	28 (21601)	5.73
	2 49 (19201)	6.03	34 (13201)	5.85	34 (13201)	5.87	14 (10401)	6.27	14 (10401)	6.19	27 (20801)	6.36
2019	3 32 (12401)	6.08	27 (10401)	6.04	54 (21201)	6.18	10 (7201)	6.42	16 (12001)	6.43	14 (10401)	6.47
	4 20 (7601)	6.18	37 (14401)	6.14	27 (10401)	6.36	19 (14401)	6.53	17 (12801)	6.45	17 (12801)	6.49
	5 28 (10801)	6.28	31 (12001)	6.34	55 (21601)	6.54	16 (12001)	6.60	19 (14401)	6.65	26 (20001)	6.54
	1 32 (12401)	6.00	34 (13201)	5.17	34 (13201)	5.05	20 (15201)	5.88	17 (12801)	5.98	17 (12801)	5.94
	2 27 (10401)	6.08	27 (10401)	5.84	56 (22001)	6.03	14 (10401)	6.38	14 (10401)	6.15	14 (10401)	6.33
2020	3 20 (7601)	6.17	37 (14401)	6.22	27 (10401)	6.08	10 (7201)	6.51	16 (12001)	6.35	28 (21601)	6.58
	4 28 (10801)	6.23	31 (12001)	6.26	25 (9601)	6.23	19 (14401)	6.68	10 (7201)	6.58	10 (7201)	6.59
	5 46 (18001)	6.27	20 (7601)	6.27	20 (7601)	6.38	23 (17601)	6.68	18 (13601)	6.66	16 (12001)	6.67

**The term "Segm." refers to the section of the railroad track with length L_0 that contains the measurements in the order beginning with the measurement in the bracket.*

Table 9. *Netherlands Q indices under Zero-crossings segmentation*

		with length more than 25 m			with length more than 50 m		
Parameter		Segment	start at	TQI_N	Segment	start at	TQI_N
Gauge	2017	183	10762	5.30	183	10762	5.51
	2018	712	19429	5.63	145	7653	5.61
	2019	728	19495	5.76	159	7727	6.04
	2020	25	3336	5.83	25	3336	6.09
Left	2017	324	5583	6.75			
	2018	1205	22253	6.41			
	2019	421	7939	6.50			
	2020	1185	22167	6.09			
Right	2017	1306	22187	6.75			
	2018	1073	22254	5.30			
	2019	1213	22128	6.39			
	2020	1165	22177	6.53			

In contrast, the Zero-crossings segmentation approach exploits the intrinsic structure of railway track measurements by modeling them as a signal process. Acknowledging its theoretical advantages, the amalgamation of the FRA approach within a Zero-crossings segmentation framework highlights augmented resilience, as presented in **Table 7**. Additionally, it is evident that the sensitivity of the FRA approach, when applied across the three segmentation methodologies, is significantly influenced by the choice of length (L_0) and the number of measurements utilized in the distinct, moving, and Zero-crossings segmentation approaches, respectively. Formula (1) shows that FRA TQI for a segment can be separated by the zero-crossings segmentation inside the formula (1), hence the TQI_F calculated by the zero-crossings provides finer results for further actions. One can compare the TQI_F values considering the plots: **Fig. 8** and **Fig. 9** and **Fig. 10** . We have identified the segments in the x-axis by the indices of their ending points. Notice that Z-segments show up not equidistantly, the reason is that not all segments are considered and the segment lengths are different. We have analyzed the quality of the segments using change points in the mean detection as well. In this way, not only

Table 10. *Maximum Chinese TQI_C with lengths $L_0 = 400$ and 800.*

		$L_0 = 400$		$L_0 = 800$	
Year		Segment	TQI_C	Segment	TQI_C
	1	47(18401)	1.95	28(21601)	1.80
	2	39(15201)	1.94	20(15201)	1.69
2017	3	56(22001)	1.87	24(18401)	1.61
	4	55(21601)	1.72	27(20801)	1.44
	5	54(21201)	1.56	10(7201)	1.43
	6	55(21601)	1.85	28(21601)	1.73
	7	39(15201)	1.83	24(18401)	1.50
2018	8	46(18001)	1.63	22(16801)	1.45
	9	56(22001)	1.62	19(14401)	1.44
	10	7(2401)	1.59	20(15201)	1.43
	11	47(18401)	2.08	28(21601)	1.87
	12	39(15201)	2.00	24(18401)	1.76
2019	13	55(21601)	1.97	20(15201)	1.72
	14	56(22001)	1.76	27(20801)	1.56
	15	54(21201)	1.76	22(16801)	1.45
	16	39(15201)	2.11	20(15201)	1.82
	17	47(18401)	1.98	28(21601)	1.65
2020	18	55(21601)	1.79	24(18401)	1.58
	19	31(12001)	1.57	19(14401)	1.53
	20	49(19201)	1.54	10(7201)	1.50

**The term "Segment" refers to the section of the railroad track with length L_0 that contains the measurements in the order beginning with the measurement in the bracket. .*

the places of the maximum values but the significant changes in the mean can be recognized. All three methods provide the same results, in particular, **Fig. 8** and **10** are very similar.

2. Netherlands Q index

Nevertheless, it is important to note that the Netherlands Q index was originally formulated for assessing the quality of 200-meter segments within maintenance sections spanning distances of 5 km to 10 km. To evaluate the quality of Hungarian railway track geometry, lengths of 100 m and 200 m were adopted for the application of the Netherlands Q index.

The numerical findings presented in **Table 8** indicate a notably high level of quality within the Hungarian railway system, with an average score of 80% relative to the maximum achievable quality. Furthermore, these results highlight the resilience of the Netherlands Q indices across multiple years as the methodology effectively mitigated the influence of outliers. Interestingly, the minimum TQI_N values were obtained from disparate and distinct segments; however, the method exhibited relatively low variation among these segments. Additionally, the outcomes underscore the minimal impact of theoretical length on Netherlands Q indices.

Conversely, the approach exhibited a marginally increased track gauge quality level when utilizing a Zero-crossings segmentation approach with a theoretical length of 200 m as the benchmark for segment consideration. Nevertheless, the methodology demonstrated consistent quality levels over the years and exhibited greater resilience to the influence of outliers. Additionally, it should be noted that the quality of the left and right alignments was comparatively same as the results obtained through the distinct/moving segmentation approach, as shown in **Table 9**.

3. Chinese TQI

The primary objective of the Chinese Track Quality Index (TQI_C) approach within the context of high-speed railways is to evaluate the overall quality of track segments. **Table 10** presents the computed TQI_C values for the Hungarian railway. We used three instead of seven quality parameters because only the gauge and left and right alignments were available in our datasets. Notably, the method exhibited increased variability between segments as the theoretical length decreased. Conversely, greater theoretical lengths resulted in reduced TQI variability among the segments. Furthermore, the adoption of higher theoretical lengths yielded more stable TQI values throughout this study.

Although both the FRA and Netherlands Q index approaches yielded exceptional TQI values when applied within the Zero-crossings segmentation framework, it is essential to note that the adoption of the Zero-crossings segmentation approach is not feasible for the Chinese TQI_C. This limitation arises from the fact that, for the same sequence of measurements, distinct Zero-crossings segments are obtained for various railway geometric parameters, rendering it impractical for uniform application.

V. Conclusion

The current TQI methodologies are predominantly designed to assess the quality of track geometry in the context of standard-gauge railways, encompassing both high-speed and broadband rail networks. These methodologies hinge on track geometry data collected under loaded track conditions by employing a versatile multifunctional TRV. The track geometry parameters extracted from the TRV measurements on the Hungarian railway align with the criteria stipulated in the EN 13,848 series.

The evaluation of track geometry quality entails the computation of the TQI within a predetermined segment characterized by specified dimensions. In the context of assessing the Hungarian railway system, a range of metrics, including the FRA's TQI, Netherlands' Q index, and Chinese TQI, have been utilized. Diverse segmentation techniques encompassing Distinct, Moving, and Zero-crossings approaches have been investigated.

The primary objective of this study was to address these questions by conducting a comprehensive track quality assessment of the Hungarian railway system employing three fundamentally distinct TQI measures. Based on the acquired results and ensuing discussion, the following conclusions can be drawn.

- Track segmentation plays a pivotal role in the assessment of railway track quality by facilitating the analysis of deviations and irregularities in track geometry. In addition, it has significant implications for strategic planning related to maintenance and reconstruction efforts on railway tracks.
- The FRA's TQI may occasionally yield misleading quality assessments when applied to heterogeneous railway measurements.
- The utilization of the Zero-crossings segmentation approach demonstrates enhanced stability and robustness compared to distinct or moving length segmentation methods. It is evident that a thorough analysis of the factors contributing to the heterogeneity of railway track geometry degradation cannot be adequately accomplished through an examination of fixed-length track segments.
- Increasing the length of the analytical segment enhances the precision of the analysis concerning railway track geometry quality.
- The Netherlands Q index and Chinese TQI exhibit greater resilience to outliers and consistently provide more stable results over the four years.

In conclusion, based on the theoretical advantages of the Zero-crossings segmentation method and the empirical results obtained from the Hungarian railway track, it is recommended that professionals give due consideration to implementing the Zero-crossings approach over more conventional methods.

VI. Limitations of the Study

This study undertook some evaluations of three TQI methods for measuring track quality, despite the existence of over ten other techniques within the broader domain of track quality evaluation. The selection of these specific methods was intentional and based on the observation that many of the reviewed techniques required access to a more sophisticated track-geometry dataset, which can be challenging to obtain due to its complex nature. This often requires specialized track geometry measurement vehicles or dedicated equipment for data collection.

Nomenclature

ρ	The autocorrelation, unitless.
L_0	The number of measurements by segments.
TQI_C	Chinese Track Quality Index, mm.
TQI_F	Federal Railroad Administration Track Quality Index, unitless.
TQI_N	Netherlands Track Quality Index, unitless.
ACF	The autocorrelation function.
CWR	Continuously welded rail.
E	Expected value of a random variable, in unite of a random variable.
EMD	Empirical Mode Decomposition.

IMF Intrinsic Mode Functions.

MA3 Moving averages of three consecutive values.

TQI Track Quality Index, unitless.

Var Variance of a random variable, in square unit of a random variable.

Acknowledgment

The authors would like to thank MÁV Ltd. and MÁV CRTI Ltd. for their help with providing the data; Balázs Suhajda director general, Track and Engineering Facilities, MÁV CRTI Ltd.; Szabolcs Fischer, Department of Transport Infrastructure and Water Resources Engineering, Faculty of Architecture, Civil and Transport Engineering, Széchenyi István University, Győr.
This work has been supported by QoS-HPC-IoT Laboratory and project TKP2021-NKTA of the University of Debrecen, Hungary. Project no. TKP2021-NKTA-34 has been implemented with the support provided by the National Research, Development, and Innovation Fund of Hungary, financed under the TKP2021-NKTA funding scheme.

AUTHOR CONTRIBUTIONS

A. Dawod: Writing the manuscript, Writing the code, Theoretical analysis.

G. Terdik: Conceptualization, writing the code, Review and editing. Supervision.

DISCLOSURE STATEMENT

The authors declare that they have no known competing financial interests or personal relationships that could have appeared to influence the work reported in this paper.

ORCID

Abdaljbbar Dawod https://orcid.org/0000-0002-8870-8577

György Terdik https://orcid.org/0000-0002-9663-6892

REFERENCES

[1] EN 13848-5 Railway applications-Track-Track geometry quality-Part 5: Geometric quality assessment (2005).

[2] EN 13848-3 Railway Applications: Track. Track Geometry Quality. Part 3: Measuring Systems. Track Construction and Maintenance Machines (2009).

[3] J. Barnett, B. Kedem. Zero-crossing rates of mixtures and products of gaussian processes. IEEE Transactions on Information Theory (1998), 44(4):1672–1677.
https://doi.org/10.1109/18.681350.

[4] A. R. B. Berawi R. Delgado R. Calçada, C. Vale. Evaluating track geometrical quality through different methodologies. Int. J. Technol. (2010), 1(1):38–47.

[5] K. Dybeł, A. Kampczyk. Sensitivity of geometric parameters in the sustainability development of continuous welded rail. Acta Technica Jaurinensis (2022), 15(3):150–161.

[6] Federal Railroad Administration. Development of objective track quality indices (2005), pages 6–9.
http://www.fra.dot.gov/downloads/research/rr0501-.pdf.

[7] S. Fischer N. Liegner P. Bocz Á. Vinkó, G. Terdik. Investigation of Track Gauge and Alignment Parameters of Ballasted Railway Tracks Based on Real Measurements Using Signal Processing Techniques. Infrastructures (2023), 8(2).
https://doi.org/10.3390/infrastructures8020026.

[8] L. Guo H. Lin X. Wu, H. Cui. Study on comprehensive evaluation method for track irregularity based on hsmm. In: 2015 4th International Conference on Sensors, Measurement and Intelligent Materials (2016). Atlantis Press, pages 1191–1194.

[9] N. E. Huang Z. Shen S. R. Long M. C. Wu H. H. Shih Q. Zheng N.-C. Yen C. C. Tung, H. H. Liu. The empirical mode decomposition and the hilbert spectrum for nonlinear and non-stationary time series analysis. Proc. of the Royal Society of London. Ser. A: Mathematical (1998), pages 903–995.

[10] ISO 23054 (2020). Railway applications — Track geometry quality — Part 1: Characterization of track geometry and track geometry quality. Standard ISO/IEC TR ISO 23054-1:2022,

International Organization for Standardization, Geneva, CH.
https://standards.iteh.ai/catalog/standards/sist/8f0-d380b31fd-437e-b673-ee5d18304be5/iso-23054-1-2022.

[11] S. Jovanovic. Railway track quality assessment and related decision making. In: 2004 IEEE International Conference on Systems, Man and Cybernetics (IEEE Cat. No.04CH37583) (2004), volume 6. pages 5038–5043 vol.6.
https://doi.org/10.1109/ICSMC.2004.1400992.

[12] V. Jover, S. Fischer. Statistical analysis of track geometry parameters on tramway line no. 1 in budapest. Baltic Journal of Road & Bridge Engineering (RTU Publishing House) (2022), 17(2).

[13] T. Karis. Correlation between track irregularities and vehicle dynamic response based on measurements and simulations (2018).
https://www.divaportal.org/smash/record.jsf?pid=-diva2%3A1206424&dswid=2266.

[14] B. Kedem. Spectral analysis and discrimination by zero-crossings. Proceedings of the IEEE (1986), 74(11):1477–1493.
https://doi.org/10.1109/proc.1986.13663.

[15] B. Kedem, S. Yakowitz. Time series analysis by higher order crossings (1994). IEEE press, New York.

[16] R.-K. Liu P. Xu Z.-Z. Sun C. Zou Q.-X. Sun et al. Establishment of track quality index standard recommendations for beijing metro. Discrete Dynamics in Nature and Society (2015), 2015.

[17] P. J. J. Luukko J. Helske, E. Räsänen. Introducing libeemd: a program package for performing the ensemble empirical mode decomposition. Computational Statistics (2015), 31(2):545–557.
https://doi.org/10.1007/s00180-015-0603-9.

[18] I. Majstorović M. Ahac J. Madejski, S. Lakušić. Influence of the Analytical Segment Length on the Tram Track Quality Assessment. Appl. Sci. (2022), 12(19).
https://doi.org/10.3390/app121910036.

[19] D. E. Martin. Detection of periodic autocorrelation in time series data via zero-crossings. Journal of Time Series Analysis (1999), 20(4):435–452.

[20] E. Nedeliaková V. Štefancová, Š. Kudláč. Six sigma and dynamic models application as an important quality management tool in railway companies. Procedia Engineering (2017), 187:242–248.

[21] J. Neuhold I. Vidovic, S. Marschnig. Preparing track geometry data for automated maintenance planning. Journal of Transportation Engineering, Part A: Systems (2020), 146(5):04020032.

[22] C. Ngamkhanong S. Kaewunruen, B. J. A. Costa. State-of-the-art review of railway track resilience monitoring. Infrastructures (2018), 3(1):3.

[23] S. Offenbacher J. Neuhold P. Veit, M. Landgraf. Analyzing major track quality indices and introducing a universally applicable tqi. Appl. Sci. (2020), 10(23):1–17.
https://doi.org/10.3390/app10238490.

[24] S. O. Rice. Mathematical analysis of random noise. The Bell System Technical Journal (1945), 24(1):46–156.

[25] R. A. Rios, R. F. de Mello. Applying empirical mode decomposition and mutual information to separate stochastic and deterministic influences embedded in signals. Signal Processing (2016), 118:159–176.
https://doi.org/10.1016/j.sigpro.2015.07.003.

[26] J. Šestáková A. Pultznerová, M. Mečár. The maintenance of the railway superstructure and its influence on the track geometry of regional line. Acta Technica Jaurinensis (2022), 15(3):162–173.

[27] I. Soleimanmeigouni A. Ahmadi H. Khajehei, A. Nissen. Investigation of the effect of the inspection intervals on the track geometry condition. Structure and Infrastructure Engineering (2020), 16(8):1138–1146.
https://doi.org/10.1080/15732479.2019.1687528.

[28] Á. Vinkó, P. Bocz. Experimental investigation on condition monitoring opportunities of tramway tracks. Periodica Polytechnica Civil Engineering (2018), 62(1):180–190.

[29] Z. Yang B. W.-K. Ling, C. Bingham. Trend extraction based on separations of consecutive empirical mode decomposition components in hilbert marginal spectrum. Measurement (2013), 46(8):2481–2491.
https://doi.org/10.1016/j.measurement.2013.04.071.

ACTA TECHNICA JAURINENSIS
Vol. 17, No. 1, pp. 22-35, 2024
10.14513/actatechjaur.00728

The development of a stitch-based strain sensor for woven lashing straps

Norman Lesser[1,*], Bernd Sadlowsky[2]

[1]Institute for BFSV, Ulmenliet 20, 21033 Hamburg, Germany Phone: +49 17641911633
[2]HAW Hamburg University of Applied Sciences, Department of process engineering, Ulmenliet 20, 21033 Hamburg, Germany
[*]E-mail: lesser@bfvs.de

Submitted: 13/12/2023 Accepted: 29/01/2024 Published online: 19/02/2024

Abstract: In this paper the development of a stitch-based strain sensor for lashing straps is discussed. A variety of Three different commercial woven narrow fabric straps were embroidered with conductive yarns in two designed patterns to enable belt tension measurement and monitoring. The applications were tested in a cyclic elongation test and a creep elongation procedure to investigate the strain sensitivity and the influences of the narrow fabric's properties, the stitch design, and the conductive yarn properties. It was found that the developed applications provided a good strain sensing ability but lack in cyclic recovery abilities.

Keywords: smart textiles; strain sensor; lashing strap; load security

I. INTRODUCTION

Woven narrow fabric straps are an essential tool for modern road freight transportation. They play a pivotal role in ensuring a proper load security by lashing down cargo or fixating it in the transport carrier vehicle. During road transportation the transport vehicle accelerating, braking, and manoeuvring is conducting dynamic acceleration forces onto the transported freight. If not properly secured those dynamic acceleration forces will move and shift the transported goods inside of the vehicle and will eventually lead to severe transport damages occurring in the freight or even cause fatal road traffic accidents.

A proper securing procedure requires a precise load securing belt tensioning, which amount of required tension must be calculated precisely in regard of the cargos mass, size and shape. Complex loads may require securing with multiple straps with each belt tension individually adjusted and monitored during the whole transport. [1 - 5] In recent years various research and development projects have successfully implemented stitch-based textile resistive strain sensors for a textile substrates strain and elongation measurement. Especially in medicine and healthcare applications as well as in soft robotics or lightweight construction materials, stitched sensor applications with the ability to sense even tiny amounts of substrate elongation have proven to be promising to solve specific technical problems. [6, 7]

However, research focusing on stitch-based strain sensors for belt tension measurement of woven lashing straps is relatively rare and the particular use of stitch-based strain sensors for load security monitoring have not been widely explored until this point. CNC-embroidery machines allow smart textile developers to freely design and embroider textile circuitry and conductive pathways onto a broad variety of textile substrates in various dimensional shapes and stages of manufacturing. [8, 9] This paper presents a case study about embroidering narrow fabric straps feasible for object securing and fixation with a stitch-based resistive strain sensor. The aim of this study is to investigate if stitch-based strain sensors are a feasible attempt to measure the applied belt tension while fixating an object and to monitor it during a transport time.

II. STITCH-BASED STRAIN SENSORS

Stitching techniques like sewing and embroidery are some of the oldest textile manufacturing processes known. A stitch is generally formed by a needle penetrating a fabric while guiding a yarn thru it. The Yarn loop with itself or with another present yarn on the fabrics reverse side, locking it form-fitting and by friction force. A stitch can generally be classified by the pattern of its loop formation and its geometrical properties like its stitch length, width, and depth. Stich types are commonly categorized by established standards like ISO 4915:1991. [10, 11]

A Stitch made from a single or multiple conductive yarns conducts electrical current thru a textile fabric acting as a textile conducting element in a circuit. Like every conventional conductor, like for example metal wires, the stitched conductive yarn has a specific electrical resistivity in relaxed condition, which changes when deformation occurs. [12, 13]

The change of the stitch's resistivity can be used as a computable electrical signal to calculate its physical elongation and therefore the stitched fabrics elongation itself. With the general deformation behaviour of the textile substrate known, the working strain can be calculated from the measured resistivity change using the sensors gauge factor. [14] The gauge factor is a proportional factor describing resistivities change in comparison to the sensor's elongation. It is commonly used as an indicator for a strain sensors general level of sensitivity. Other important sensor characteristics are its linearity, describing the proportion in resistance change in relation to the change in working strain., as well as the sensors recovery property. A sensors recovery property describes the ability to maintain its sensing quality after multiple cycles of use without permanent resistance drift or occurring damages decreasing its sensitivity. [15-17]

Conductive fibers spun to conductive yarns and being stitched onto fabric in a certain pattern are far from being ideal conductors. So most conventional models depicting the strain resistive behaviour of metal wires or printed metal films are not suitable to describe or predict a stitch-based strain sensors sensing mechanism or general conductive behaviour. [18] The conductivity and resistivity of a single conductive fiber depends on various factors like for example it's length, width, and square geometry as well as the used functionalization method. Spun yarns may contain several thousands of single conductive fibers entangled with one another. A conductive yarn with a certain length can therefore be depicted as a conductive network of an infinitesimal high number of single conductors short circuiting with one another due to their physical entanglement. In generally a yarns resistivity was found to be positively correlated with its length, meaning that a piece of yarns measured resistivity is higher, the longer it is. [19-22]

When a certain Pattern is stitched onto a fabric a certain amount of total yarns length is integrated into the substrate, depending on the stitch's properties like its density, width, and depth. Considering the found positive correlation between a piece of yarns length and its resistivity, stitches with a high stitch density, width, and length, like for example a lockstitch in ZigZag-Pattern, tend to have a higher absolute stitch resistivity than straight lockstitches in comparison. The base resistivity of a stitched sensor application per lengths unit on a fabric's surface therefore depends highly on the stitch's pattern and its properties. [23-26]

When multiple conductive yarns are used to form a stitch, looping, or physically contacting one another due to several loops or conductive yarn sections overlapping causes short circuits leading an overall stitched patterns resistivity to drop. A stitch can be described as a conductive network with its overall resistivity depending mostly on the stitched patterns properties and the presence and concentration of the conductive yarn short circuiting overlapping or cross sectioning loops and entanglement points. (**Fig. 1** and **Fig. 2**) When the fabric is stretched its deformation causes the stitch's width, depths as well as the stitch's density to change as well. When the stitch's properties change and the stitch's geometry seen on the fabrics surface as well deforms, overlapping loops of the conductive yarn separate from one another and cross sectioning areas may shift in contact size and location. These causing former yarn to yarn contact induced short circuits to eventually open and the patterns overall resistivity to change. (**Fig. 3**)

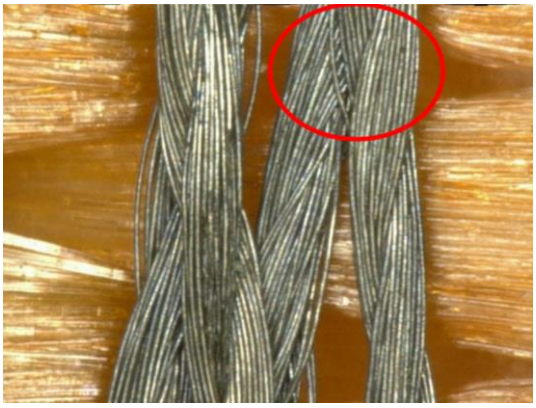

Figure 1. *Overlapping conductive yarn loops*

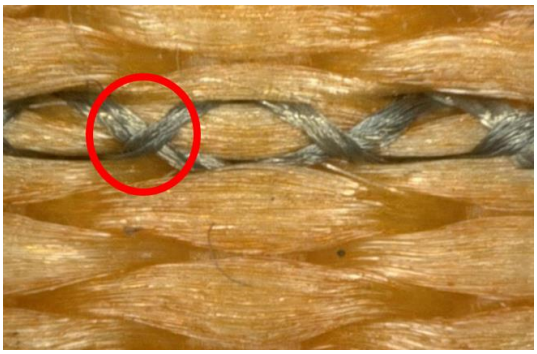

Figure 2*. Cross sectioning conductive yarn loops*

The fabrics and stitch's deformation induces mechanical stress to the conductive yarn. The yarn gets stretched due to the stitch's properties changing. Also, the deformation of the fabric may cause lateral compressive forces to increase locally around the stitch's loop entanglement points. The fabrics deformation will therefore shift the stitch's conductive network as well as the yarns resistive

properties itself due to the working mechanical stress.

A stitches overall measured change in resistivity under deformation therefore results both from the combined conductive network changes of yarn and stitched pattern. [27, 28] The fabrics general deformation properties affecting the degree to which its strain induced elongation is conducted to an applied stitch. In reverse the stitch-based application of a yarn onto a fabric and its physical entanglement with it may also affect the fabrics deformation behaviour to some degree. This interaction between the stitch's mechanical deformation characteristics and the fabrics mechanical properties have been the focus of research in the past. A strain sensors functional aspects like its sensitivity, linearity and especially its recovery properties (like its hysteresis error and baseline resistivity drift) have been found to be largely dependent on the stitch's deformation behaviour matching the fabric's. [29] A stitch-based sensors strain sensing behaviour can therefore be described as depending on three main aspects. That being the used conductive yarns resistance changing behaviour under applied strain, the stitch's mechanism of its conductive networking shifting when a fabrics deformation is conducted and at last the stitches and the fabrics deformation behaviour under applied strain interacting with one another.

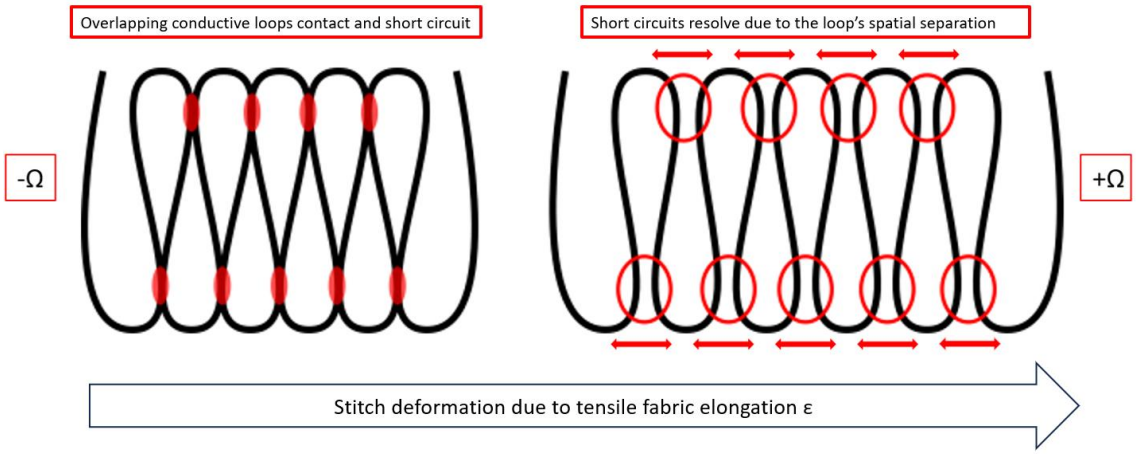

***Figure 3**. Schematic representation of the mechanism of increasing resistance by dissolving the yarn contacting*

III. PROBE PREPARATION

Three commercial narrow fabric straps differing in their belt thickness, width, and weight as well as in their maximum tensile strength and stiffness were chosen to be functionalized with a stitch-based strain sensor. All narrow fabric were bought from *Rolf Schwarzbach – Fachhandel (Wipperfürth, GER)* All straps were plain woven from synthetic filament yarns. (**Fig. 4-6**) (**Table 1-2**) In this paper the different narrow fabrics are coded by their product number, given by the supplier. The narrow fabrics were embroidered with two versions of a 304-ZigZag lockstitch using a *ZSK JCZA* computer-controlled embroidery machine *(ZSK Stickmaschinen GmbH, Krefeld (GER))*. Both applications dimensions are illustrated in **Fig. 7**.

***Table 1.** Narrow fabric properties*

Narrow fabric	*Fiber material*	*Width [mm]*	*Thickness [mm]*
2.23.100.0105	100% PP	40	1
2.23.200.1600	100% PES	45	1.5
2.23.100.0115	100% PP	50	2.3

***Table 2**. Narrow fabric mechanical deformation properties*

Narrow fabric	*Maximum tensile strength F_N [daN]*	*Elongation at maximum tensile strength ε [%]*
2.23.100.0105	404	28.4
2.23.200.1600	1140	23.4
2.23.100.0115	1100	31.2

Both versions varied in their stitch properties to examine their influence on the strain sensing behaviour in comparison. (**Table 3**)

The stitch *ZigZag_V2_Axial* (**Fig. 8-9**) was designed with a particular high stitch density and width. Therefore, a generally high absolute length of conductive yarn was used for this stitch. The second stitch *ZigZag_Double_V2* (**Fig. 10-11**) was composed of two 304-ZigZag lockstitches cross sectioning one another. All probes were embroidered with loose ends for contacting to a multimeter. The individual Probe's consistency is attached in the Appendix (**Table 5**)

Table 3. *Stitch properties*

Stitch Version	***Stitch density***	***Stitch width***	***Stitch depth***
ZigZag_V2_Axial	11 Stitches /10mm	5mm	0.9mm
ZigZag_Double_V2	8 Stitches /10mm	0.8mm	1.2mm

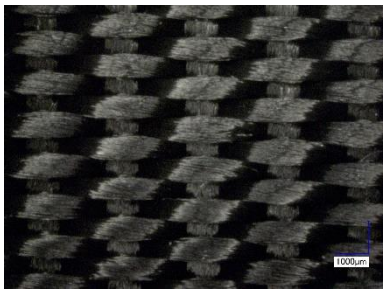

Figure 4 *Narrow fabric surface image 22.23.100.0105“*

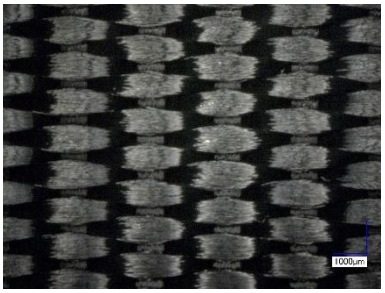

Figure 5. *Narrow fabric surface image 2.23.200.1600”*

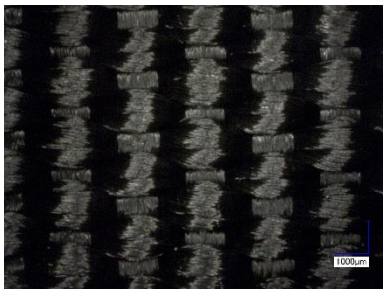

Figure 6. *Narrow fabric surface image 22.23.100.0115“*

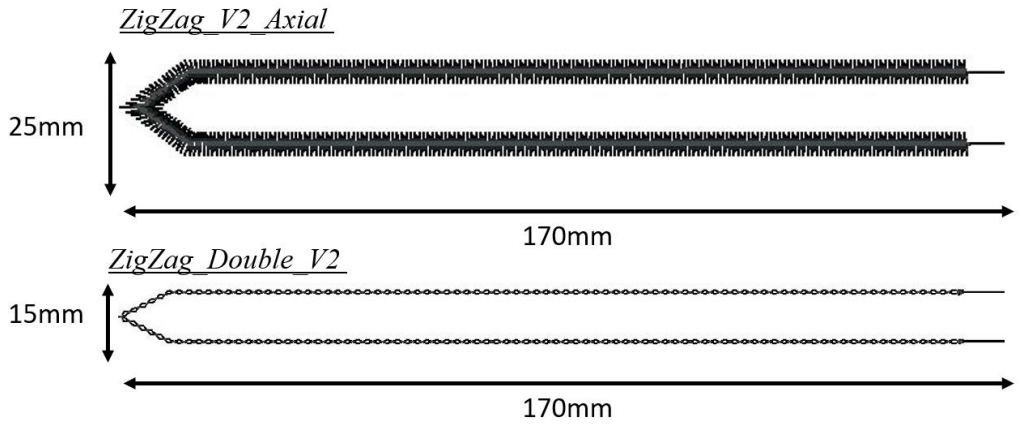

Figure 7. *Stitch dimensions*

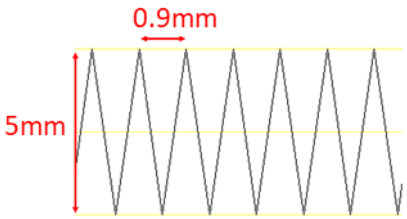

Figure 8. *Stitch properties ZigZag_V2_Axial*

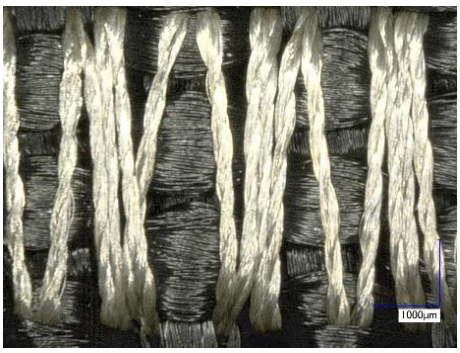

Figure 9. *Microscope image ZigZag_V2_Axial*

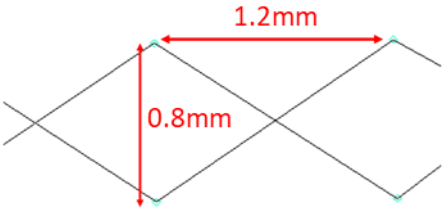

Figure 10. *Stitch properties ZigZag_Double_V2*

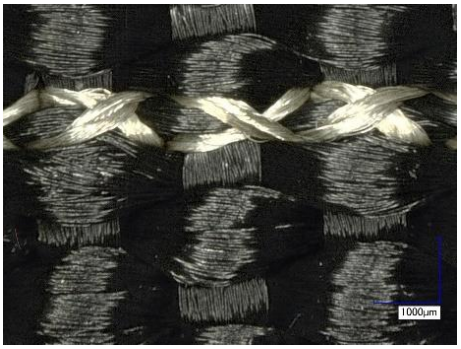

Figure 11. *Microscope Image ZigZag_Double_V2*

The chosen silver-plated yarns *Amann Silver-tech+100* and *Amann Silver-tech+150* (Amann&Söhne GmbH & Co.KG, Bönningheim (GER)) came with a different titer and electrical resistivity per meter yarn length. For the stitch version called *ZigZag_V2_Axial* the non-conductive yarn *Amann ISA Tex 80* was used as a lower yarn. For *ZigZag_Double_V2* the conductive yarns were used as both upper and lower yarns. (**Table 4**)

Table 4. *Yarn properties*

Yarn	***Fiber material***	***Titer [dtex]***	***Yarn resistivity [Ω/m]***
SIlver-Tech+100	100% PA	330	<200
SIlver-Tech+150	100% PA	220	<300
ISA 150	100% PES	180	-

IV. TESTING METHOD

The manufactured probes were tensile tested using a *Zwick 1455 20kN (ZwickRoell GmbH & Co. KG, Ulm (GER))* tensile testing machine (**Fig. 12**) with an attached *Elabo R-Meter /SRM 05 (ELABO GmbH, Crailsheim (GER))* multimeter (**Fig. 13**). For tensile testing *Zwick Pneum. Probenhalter Typ 8487 – Fmax.20kN* specimen clamps were installed in the tensile testing machine. For pneumatic probe fixation air pressure of 4 bar was used. The clamps were equipped with ribbed clamping jaws for a better grip in probe fixation. The tensile testing machine was controlled with the testing software TestXpert3 (*ZwickRoell GmbH & Co. KG, Ulm (GER)*). The software allowed the simultaneous measurement of the probe deformation data as well as their electrical resistivity change. The stitches electrical resistivity was measured by connecting the used multimeter to the stitched loose ends using crocodile clamps. (**Fig. 14**)

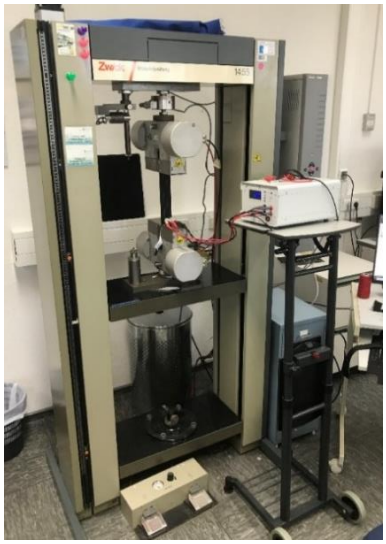

Figure 12. *Zwick 1455 20kN tensile testing machine*

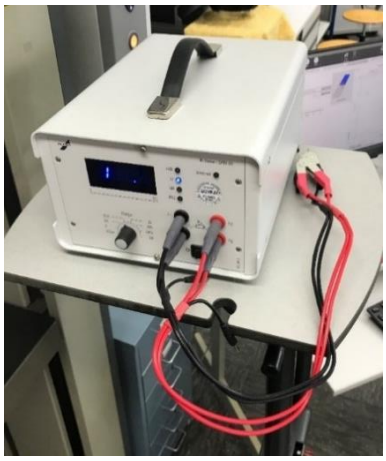

Figure 13. *Elabo R-Meter/SRM 05*

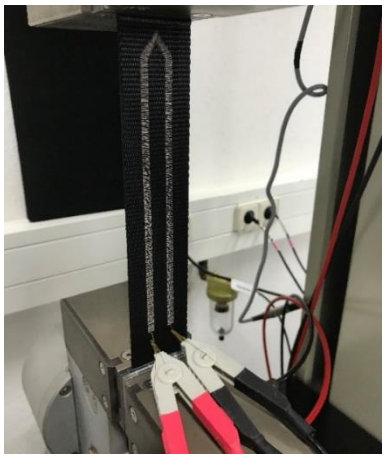

Figure 14. *Loose stitch ends contacted with crocodile clamps*

To investigate the probes strain sensing behaviour two tensile testing procedures were set up in orientation to DIN EN ISO 13934-1. For each test three probes of each combination type were manufactured and tested.

The first testing procedure consisted of the probes controlled cyclic elongation from ε=0% to ε=7%. (**Fig. 15**) The aim of this procedure was to simulate multiple object fixation and release procedures. A maximum elongation of ε=7% was chosen in orientation to DIN EN 12195-2. The probes change in electrical resistivity was plotted alongside the elongation. During this procedure the different probes strain sensitivity and linearity was determined by calculating the probes gauge factor K, using the following formulas (1 – 3).

$$K = \frac{\frac{\Delta R}{R0}}{\frac{\Delta l}{l}} \tag{1}$$

$$\frac{\Delta R}{R0} = k \cdot \frac{\Delta l}{l} = k \cdot \varepsilon \tag{2}$$

$$\varepsilon = \frac{\Delta l}{l} = \frac{\frac{\Delta R}{R0}}{k} \tag{3}$$

where K = gauge factor; R0 = Resistivity [Ω]; l = length [mm]; ε = elongation [%] .

For each deformation cycle the probes strain gauge factors were calculated in intervals of 0.5% elongation. All interval related gauge factors from one cycle were averaged arithmetically and compared in relation to the number of cycles to examine the cyclic wear on the strain sensors. The probes single cycles average gauge factors were then again averaged to compare the different probes sensitivity in general. The sensing linearity was examined by calculating the gauge factors standard deviation for each cycle. A high standard deviation was interpreted as the gauge factor changing volatile in relation to the applied rate of strain. Therefore, a high gauge factor standard deviation was seen as an indicator for a low linearity. The cycles standard deviations were arithmetically averaged to compare the single probes. The second procedure was a creep elongation test where the probes were stretched to an amount of 2000N Force. The probes were locked in their state of elongation after reaching 2000N over 5 Minutes. (**Fig. 16**) This procedure was designed to simulate an object fixation procedure and fixation over a certain amount of transportation time. The harvested data was used to examine if the built belt tension would lose over time due to the fabrics relaxation and if this loosening could be monitored by measuring the stitches resistivity change. The probes absolute resistivity change was plotted alongside the machines applied strain tension Force and the procedures time. Every procedure was tested with stitched probes as well as with unstitched narrow fabric probes and the single conductive yarns for reference. Every narrow fabric probe was cut to a length of 250mm for testing. The single yarn probes were cut to a length of 350mm. Before the testing all probes were exposed to climatization 20°C/65% rel. humidity for 24 hours. All tests were done in a climatized environment with 20°C/65% rel. humidity. The probes narrow fabric length as well as the stitched applications length were measured before every procedure. After the test procedures the tested probes were then again exposed to climatization 20°C/65% rel. humidity for 24 hours and the lengths were again measured for comparison. The stitches resistivity in relaxed state were also measured before and after the testing procedures together with the probe's length. For length measurements a steel ruler was used. For measuring the probes initial resistivity, a DMM6500 6 ½ multimeter *(Keithley Instruments Inc., Cleveland (USA))* was used

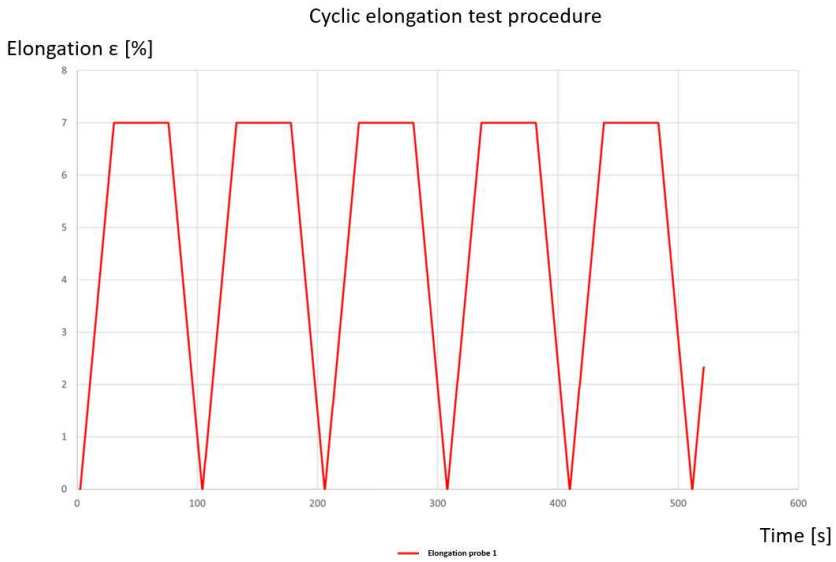

Figure 15. *Cyclic elongation test routine*

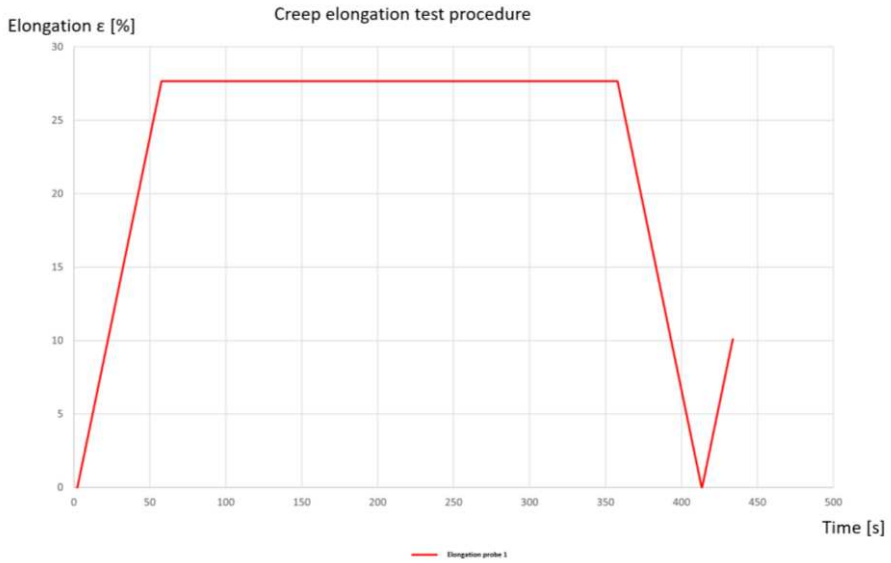

Figure 16. *Creep elongation test routine*

V. RESULTS AND DISCUSSION

In this section the experiments result will be presented. The probes strain sensitivity and linearity differ in relation to the composition of narrow fabric, conductive yarn, and stitch type. In **Fig. 17** the probes averaged sensitivity (green) and linearity (blue) is shown. The single probes overall calculated sensitivity is the result of the three composition parameters behaviour under applied strain, interacting with one another.

Probes based on the stitch type ZigZag_Double_V2 tend to provide a higher averaged strain sensitivity than the ZigZag_V2_Axial equivalents. The ZigZag_Double_V2 tend to show a higher sensitivity when Amann Silver-tech+100 is used as conductive yarn. The probes based on ZigZag_V2_Axial show none such tendency. The ZigZag_Double_V2 probes linearity increase when Amann Silver-tech+150 is used, while Amann Silver-tech+150 tends to show a higher linearity with ZigZag_V2_Axial. The probes linearity seems to be mainly dependent on the used yarn, while the sensitivity is particularly influenced by the stitched pattern. The exercised cyclic elongation causes a drift in the sensor applications resistivity and sensitivity, increasing over the number of cycles. The probes measured resistivity at ε=0% to ε=7% elongation increases successively while the working amount of strain Force oppositely decreases. (**Fig. 18-19**) This behaviour can be explained with by the cyclic tensile stress causing wear to the probes. The unstitched reference narrow fabric probes show the same cyclic decrease of loaded tensile force at ε=7% elongation. The comparison of the single probes measured narrow fabrics length and stitch length showed a permanent elongation of both after the experiment. The resistivity drift at ε=0% to ε=7% therefore is likely to be caused by the strain induced permanent deformation, where short circuiting overlapping conductive yarn loops become physically separated from one another and the stitches conductive network permanently alters with every passing elongation cycle. The level of the resistivity increasing and tensile force decreasing at ε=7% elongation alters with individual probe composition. The ZigZag_Double_V2 based probes tend to show a higher resistivity drift caused by cyclic wear then the equivalents based on ZigZag_V2_Axial in comparison. The decreasing amount of the applied tensile force is lower on the probes based on ZigZag_Double_V2 in comparison with ZigZag_V2_Axial. The two stitches different properties therefore influence the probes tensile stiffness. Probes stitched with Amann Silver-tech+150 tend to show a higher relative resistivity drift compared with Amann-Silver-tech+100. The reference tests executed on the single conductive yarns also show that Amann Silver-tech+150 resistivity increases more significantly than Amann Silver-tech+100. The probes resistivity drifting behaviour can therefore be described as mainly caused by the chosen conductive yarn behaviour and the stitches properties as well as by their influence on the fabric tensile stiffness. (**Fig. 20**)

The **Fig. 21** illustrates the probes cyclic strain sensitivity drift for each cycles averaged gauge factor. The red and yellow line illustrate the spread between the first cycle and all cycles gauge factor averaged. The probes based on ZigZag_V2_Axial show a higher resistivity drift with Amann Silver-tech+150, as the increasing spread between the first cycles averaged gauge factor and all cycles averaged gauge factors indicates. With ZigZag_Double_V2

this is the opposite with Amann Silver-tech+100 showing a higher spread. Both illustrations show that the probes individual sensitivity drifting behaviour is highly dependent on the chosen yarn and the narrow fabrics individual cyclic wear behaviour. The probes based on ZigZag_Double_V2 overall show a higher level of cyclic sensitivity drift then ZigZag_V2_Axial. The ZigZag_Double_V2 based probes level of sensitivity drift is closer to the individual conductive yarns calculated drifting behaviour.

Due to the stitch ZigZag_Double_V2 reduced stitch width and increased stitch length, the single stitched loops are aligned in steeper angle to the direction of the working tensile force during probe elongation. The higher loops orientation in the tensile force direction is likely to result in a higher direct tensile stress and stretch working on the yarn in comparison to ZigZag_V2_Axial. (**Fig. 22**) The increased tensile stress causes the yarns conductive network to alter and therefore the resistivity and sensitivity to permanently drift. The stitches sensitivity drifting behaviour approaching the single yarns behaviour at a higher loop orientation indicates that the sensitivity drift of a stitch under cyclic elongation is mainly dependent on the used conductive yarns behaviour and the stitched loops orientation to the direction of force.

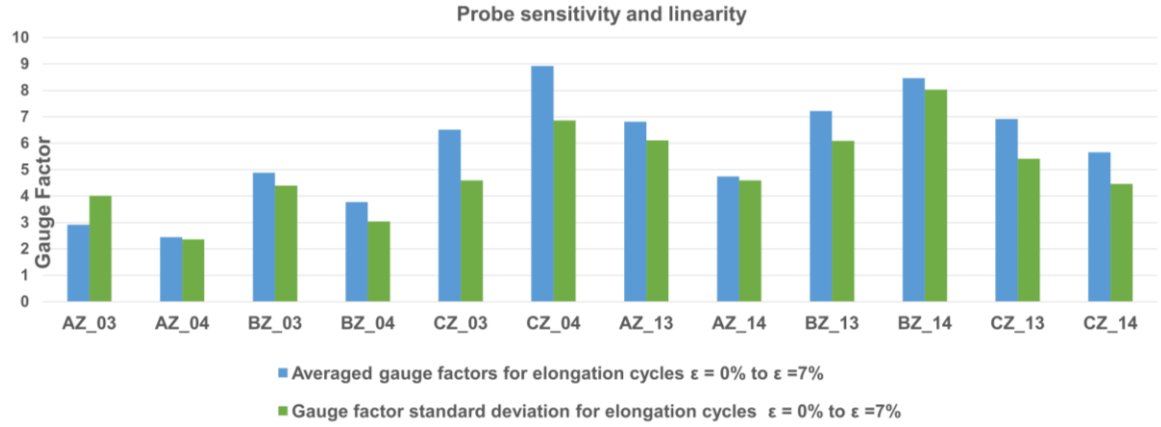

***Figure 17**. Probe averaged gauge factors (blue) and gauge factor linear deviation (green)*

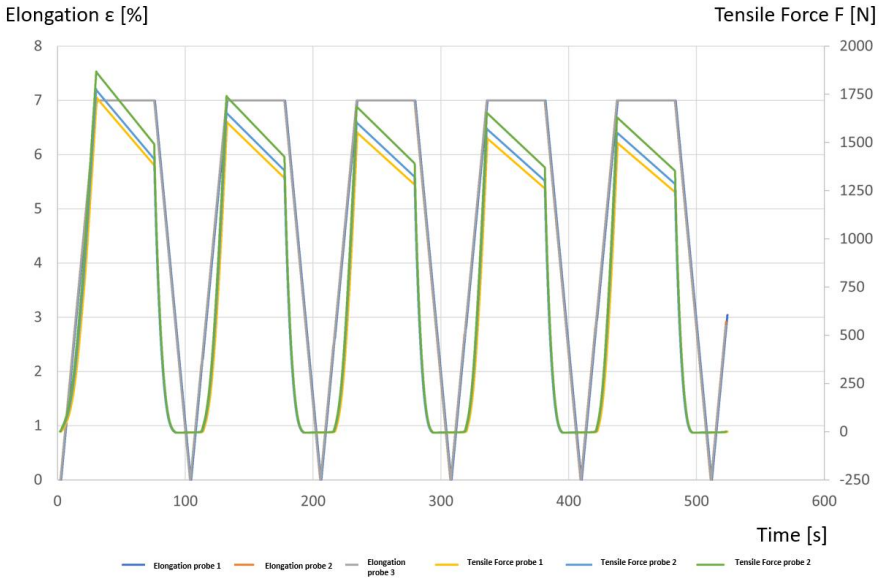

***Figure 18**. Probe C_Z0_3 strain force drifting over multiple elongation cycles*

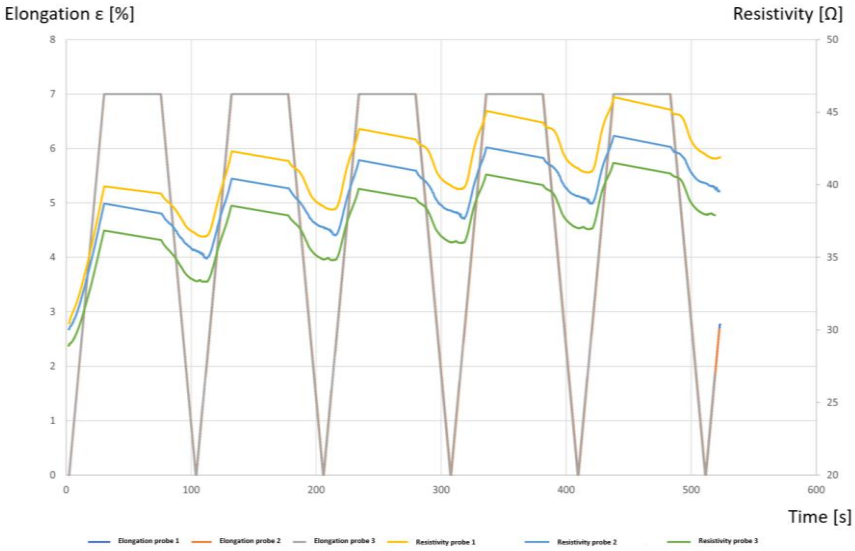

Figure 19. *Probe C_Z0_3 resistivity drift over multiple cycles*

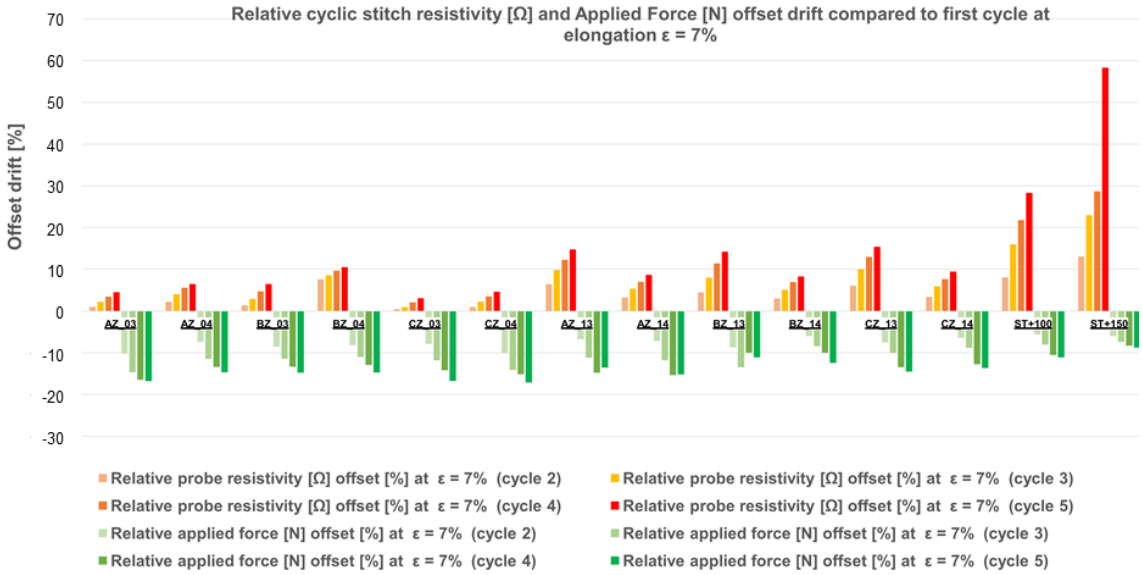

Figure 20. *Probe relative cyclic resistivity drift and relative strain force drift*

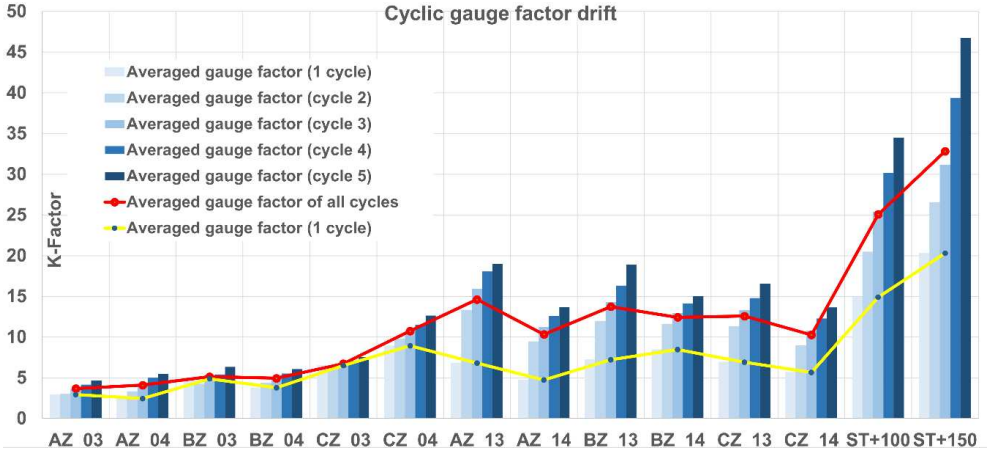

Figure 21. *Probe cyclic strain gauge factor drift*

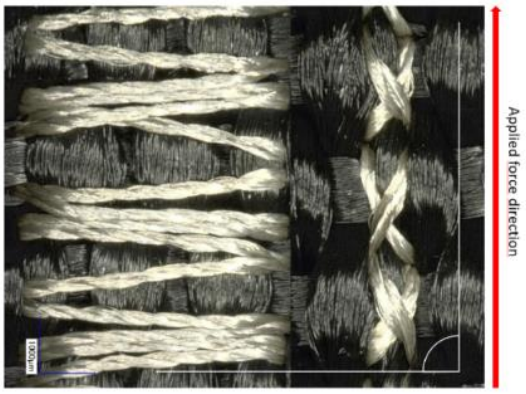

Figure 22. *ZigZag_V2_Axial (left) and ZigZag_Double_V2 (right) loop orientation in applied force direction.*

The conducted creep tests show a regressive decrease of the tensile force working on the stitched and unstitched narrow fabric probes over 275 seconds after first reaching 2000N. This belt tension loosening is expected to be caused by the fabrics woven surface rearranging and the narrow fabrics creep-elongating overtime to reduce the amount of tensile tension. Those fabrics relaxation mechanisms cause the stitches resistivity to alter. In the **Fig. 23** and **24**, the probes decrease in working tensile force and resistivity is exemplary plotted. The fabrics relaxation is conducted to the stitch, causing its conductive network to shift also back into a more relaxed state. To compare the single probes behaviour the stitches range of absolute resistivity change [Ω] is plotted and compared to the relative range of working force [%] decreasing over the creep test time of 275 seconds. (**Fig. 25**) The relative range of working force is interpreted to be mostly dependent on the narrow fabric's physical properties and relaxation behaviour. Though no correlation between the relative range of working force and electrical resistivity is clearly identifiable, the stitched probes resistivity creep alters with the narrow fabric and the yarn. The creep behaviour of ZigZag_V2_Axial is more volatile and likely to be dependent more on the specific narrow fabrics mechanical creep characteristics than ZigZag-Double_V2. ZigZag_V2_Axial behaviour can be explained due to the stitch properties. The fabric surface loosening led to formerly physically separated overlapping loops to reconnect, so the formerly increased stitch resistivity drops back. With the ZigZag_Double_V2 probes this is not the case. The investigation of the occurred permanent elongation and base resistivity drift of all probes shows that the permanent elongation of the fabrics and stitches is higher due to cyclic elongation than to a single long-term exposure to working strain. (**Fig. 26**) The amount of resistivity drift is therefore most likely dependent to the fabrics and stitches grade of permanent elongation. ZigZag_Double_V2 showed a higher resistivity drift which can be explained due to the yarn being damaged because of the sharp angle to the force direction. The amount of elongation is dependent on the fabric's mechanical deformation properties and the recovery ability. So, the occurring drift and therefore wear recovery abilities of the stitched sensors depend highly on the narrow fabric itself.

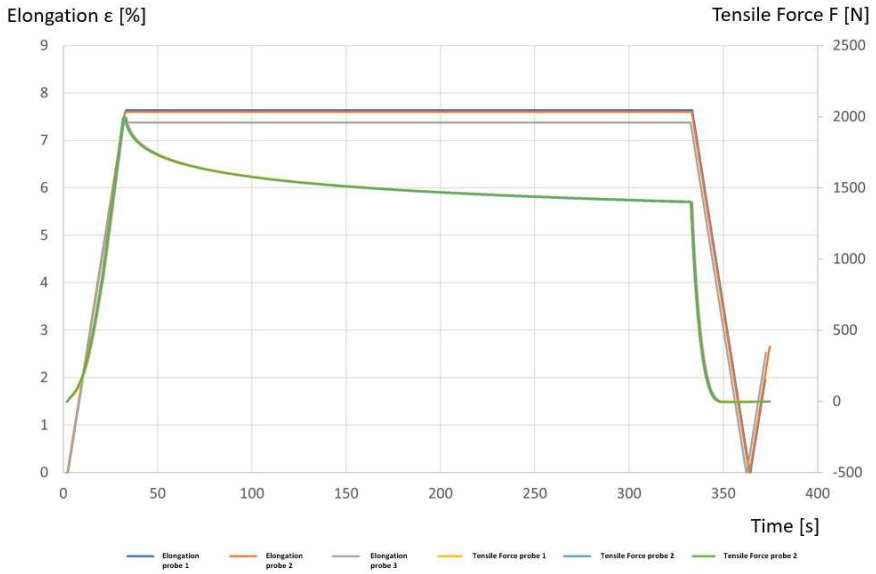

Figure 23. *Probe C_Z0_3 regressive strain force creep*

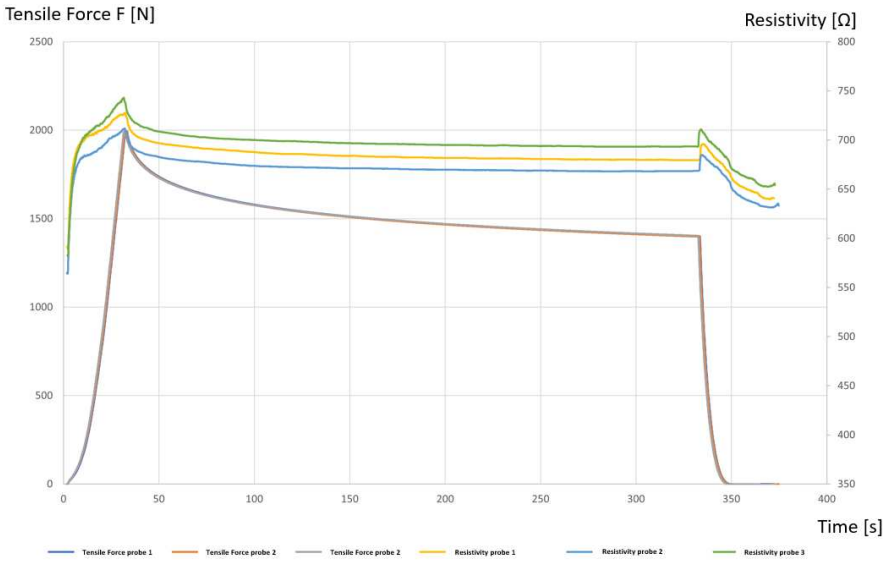

Figure 24. *Probe C_Z0_3 resistivity creep compared with strain force creep*

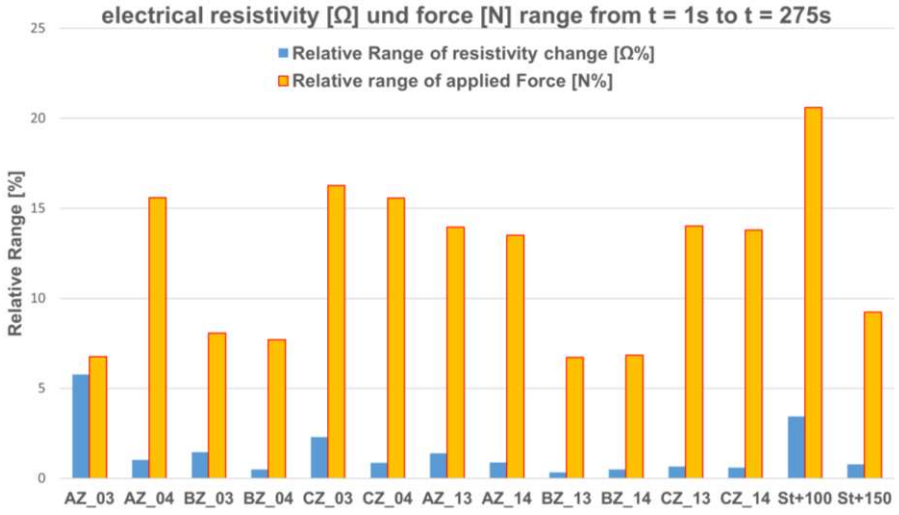

Figure 25. *Probe resistivity and strain force creep behaviour*

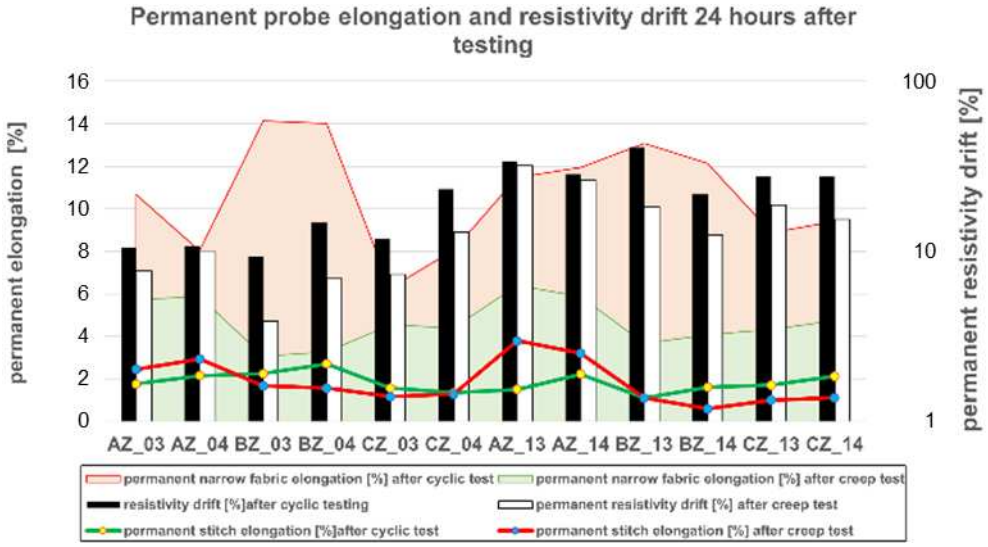

Figure 26. *Probe permanent elongation and resistivity creep 24 hours after testing procedure*

VI. CONCLUSION

The variety of stitch-based sensor applications investigated and examined in this work enabled the elongation measurement and tension monitoring on every chosen narrow fabric strap by measurable resistivity change. The individual probes level of strain sensitivity and linearity heavily depend on the combination of the conductive yarn, the stitch pattern and properties, and the narrow fabrics mechanical deformation characteristics themselves. For this work the strain sensing performance can be therefore described as the result of those three probe parameters interacting during probe deformation. Especially the stitch properties caused yarn loop orientation in tensile force direction highly influences the probes strain sensitivity and linearity. The probes gauge factor increases with a higher orientation, while the linearity decreases. This behaviour is likely to be caused from a higher exposure of the stitched yarn to mechanical stress. All probes show weak recovery properties with resistivity and sensitivity drifts occurring after multiple elongation cycles. This is likely to be caused mainly by the narrow fabrics themselves permanently elongating successively due to cyclic tensile wear, altering the applied stitches conductive network. A higher loop orientation in tensile force direction increases the drifting behaviour and reduces the probes sensor recoverability. The conducted creep elongation experiment's results shows that the narrow fabrics belt tension loosening is monitorable by the sensor applications resistivity altering with the substrates relaxation. The stitches resistivity and the working strain force decrease overtime in a similar regressive plotted curve progression. Although no correlation or regression pattern emerges from the gathered data, the feasibility to monitor the fabrics belt tension depends on the applied stitches properties. The stitch properties influencing the yarns geometrical orientation on the fabric's surface are especially found to significantly influencing the probes strain sensitivity and linearity during the chosen narrow fabric straps tensioning and monitoring. Modern computer-based embroidery provides developers with a broad freedom of stitch pattern design. With further investigation on the single stitch parameters, like stitch width, -length and -density, the use centred development of a stitch-based strain sensor could be a promising attempt for securing belt strain sensing functionalization in the future.

ACKNOWLEDGEMENT

The publishing of this paper was supported by the BFSV institute of Packaging Hamburg

AUTHOR CONTRIBUTIONS

N. Lesser: Conceptualization, Experiments, Theoretical analysis, Writing.

B. Sadlowsky: Supervision and editing.

DISCLOSURE STATEMENT

The authors declare that they have no known competing financial interests or personal relationships that could have appeared to influence the work reported in this paper.

APPENDIX

Table 5. *Manufactured probe combinations*

Probe Name	*Stitch*	*Yarn*	*Narrow fabric*	*Number of tested Probes*
A_Z0_3	ZigZag_V2_Axial	Amann Silver-tech+100	2.23.100.0105	3
A_Z0_4	ZigZag_V2_Axial	Amann Silver-tech+150	2.23.100.0105	3
B_Z0_3	ZigZag_V2_Axial	Amann Silver-tech+100	2.23.200.1600	3
B_Z0_4	ZigZag_V2_Axial	Amann Silver-tech+150	2.23.200.1600	3
C_Z0_3	ZigZag_V2_Axial	Amann Silver-tech+100	2.23.100.0115	3
C_Z0_4	ZigZag_V2_Axial	Amann Silver-tech+150	2.23.100.0115	3
A_Z0_3	ZigZag_Double_V2	Amann Silver-tech+100	2.23.100.0105	3
A_Z0_4	ZigZag_Double_V2	Amann Silver-tech+150	2.23.100.0105	3
B_Z0_3	ZigZag_Double_V2	Amann Silver-tech+100	2.23.200.1600	3
B_Z0_4	ZigZag_Double_V2	Amann Silver-tech+150	2.23.200.1600	3
C_Z0_3	ZigZag_Double_V2	Amann Silver-tech+100	2.23.100.0115	3
C_Z0_4	ZigZag_Double_V2	Amann Silver-tech+150	2.23.100.0115	3

*In each of both testing procedures 3 probes were tested

References

[1] Ladungssicherung auf Straßenfahrzeugen, VDI 2700, (2004), in German

[2] Ladungssicherung auf Straßenfahrzeugen – Berechnung von Sicherungskräften Grundlagen, VDI 2700 Blatt 2 / Part 2, (2014), in German

[3] Ladungssicherung auf Straßenfahrzeugen – Gebrauchsanleitung für Zurrmittel, VDI 2700 Blatt 3.1 / Part 3.1, (2023), in German

[4] Ladungssicherungseinrichtungen auf Straßenfahrzeugen – Sicherheit - Teil 1: Berechnung von Sicherheitskräften, DIN 12195-1, (2021), in German

[5] Ladungssicherungseinrichtungen auf Straßenfahrzeugen – Sicherheit - Teil 2: Zurrgurte aus Chemiefasern, DIN 12195-2, Berlin, (2000), in German

A. Moniruddoza, J. Mersch, P. Schegner, M. Hossain, A. Nocke, C. Chokri, Textilbasierte Sensor-Aktor-Netzwerke für hochpräzise In-Situ-Mechanismen in Faserkunststoffen, Institut für Textilmaschinen und Textile Hochleistungswerkstofftechnik, In: Institut für Textilmaschinen und Textile Hochleistungswerkstoffe, Jahresbericht 2021, Dresden, (2021), pp.1 - 2 in German

[6] R. Nolden, K. Zöll, A. Schwarz-Pfeiffer, Smart Glove with an Arduino-Controlled Textile Bending Sensor, Textile Data Conductors and Feedback Using LED-FSDs™ and Embroidery Technology, in: MDPI - Multidisciplinary Digital Publishing Institute (publ.), Technology Vol.68, Basel, (2021), pp.1 – 2. https://doi.org/10.3390/proceedings2021068004

[7] M. Hoerr, E-Textiles – Integration von Elektronik in Textilien durch Stickerei, in: Verlag Textilplus AG (Hrsg.) TEXTILplus Ausgabe 03/04-2021, (2021), pp. 23 – 24 Einsiedeln, in German

[8] V. Mecnika, M. Hoerr, I. Krievins, S. Jockenhoevel, T. Gries, Technical Embroidery for Smart Textiles: Review, Institut für Textiltechnik of RWTH Aachen, Institute of Design Technologies, Riga Technical University, Riga, Aachen, (2014), pp. 56 – 59 https://doi.org/10.7250/mstct.2014.009

[9] G. Golovic, Sewing stitches and seams, In: R. Nayak, Rajkishore, R. Padhye, Woodhead Publishing Series in textiles: Number 168 - Garment Manufacturing Technology, Woodhead Publishing Limited, Cambridge, (2015), pp.247

[10] Stitches and seams. Classification and terminology of stitch types, ISO 4915:1991, (1991)

[11] B. Moradi, R. Fernández-Garcia, I. Gil, E-Textile Embroidered Metamaterial Transmission Line for Signal Propagation Control, in: G. Stylios, Novel Smart Textiles, MDPI - Multidisciplinary Digital Publishing Institute, Basel, (2018), pp. 211–212. https://doi.org/10.3390/ma11060955

[12] J. Eichhoff, A. Hehl, T. Gries, Textile fabrication technologies for embedding electronic functions into fibres, yarns and fabrics, in: T. Kirstein, Woodhead Publishing Series in textiles: Number 139 – Multidisciplinary knowhow for smart-textiles developers Woodhead Publishing Limited, Cambridge, (2013), pp.193 – 223.

[13] K. Jansen, Performance Evaluation of Knitted and Stitched Textile Strain Sensors, in: MDPI - Multidisciplinary Digital Publishing Institute, Sensors 2020, 20, Basel, (2020), pp. 5-8. https://doi.org/10.3390/s20247236

[14] P. Regtien, E. Dertien, Sensors for Mechatronics – Second Edition, Elsevier B.V., Amsterdam, (2018), pp. 1-4 and pp. 23 – 79.

[15] O. Tangsirinaruenart, G. Stylios, A Novel Textile Stitch-Based Strain Sensor for Wearable End Users, In: MDPI - Multidisciplinary Digital Publishing Institute, Materials, Volume 12, 2019, Basel, (2019) pp. 2 – 17. https://doi.org/10.3390/ma12091469

[16] S. Keil, Dehnungsmessstreifen - 2. Auflage, Springer Vieweg Wiesbaden, Wiesbaden, (2017), pp.14 – 33 and pp. 142 - 145, in German

[17] A. Schwarz, L. Van Langenhove, Types and processing of electro conductive and semiconducting materials for smart textiles, In: T. Kirstein, Woodhead Publishing Series in textiles: Number 139 – Multidisciplinary knowhow for smart-textiles developers Woodhead Publishing Limited, Cambridge, (2013), pp. 28 – 57.

[18] L. Xiuhong, S. Chen, Y. Peng, Z. Zheng, J. Li, F. Zhong, Materials, Preparation Strategies, and Wearable Sensor Applications of conductive Fibers: A Review, In: MDPI - Multidisciplinary Digital Publishing Institute, Sensors 2022, 22, Basel, (2022), pp.1 – 23. https://doi.org/10.3390/s22083028

[19] J. Xie, M. Miao, Y. Jia, Mechanism of electrical conductivity in metallic fiber-based yarns, In: Walter de Gruyter GmbH, De Gruyter Open Access AUTEX Research Journal, Berlin, (2019), pp. 3-5. https://doi.org/10.2478/aut-2019-0008

[20] M. Miao, Electrical conductivity of pure carbon nanotube yarns, In: Elsevier B.V, Carbon Journal Vol. 49, Amsterdam, (2011), pp. 3756 – 3759.

[21] S. Chawla, M. Narahji, Effects of twist and porosity on the electrical conductivity of carbon nanofiber yarns, In: IOP Publishing ltd.,

Journal Nanotechnology Vol.24, Bristol, (2013), pp. 1 – 8. https://doi.org/10.1088/0957-24/25/255708

[22] F. Huang, H. Jiyong, X. Yan, Review of Fiber-on Yarn-Based Wearable Resistive Strain Sensors: Structural Design, Fabrication Technologies and Applications, In: MDPI - Multidisciplinary Digital Publishing Institute, Textiles 2022, 2, Basel, (2022), pp.165 – 189. https://doi.org/10.3390/textiles2010005

[23] K. Keum, S.S. Cho, J. Jeong-Wan, S.K. Park, K. Yong-Hoon, Mechanically robust textile-based strain and pressure multimodal sensors using metal nanowire/polymer conducting fibers, In: Elsevier Inc. - CelPress Open access, IScience 25, Cambridge MA, (2022), pp. 2 – 6. https://doi.org/10.1016/j.isci2022.104032

[24] S. Seyedin, P. Zhang, M. Naebe, S. Qin, J. Chen, X. Wang, J. M. Razal, Textile Strain Sensors: A Review of the Frabrication Technologies, peformance Evaluation and Applications, In: Royal Society of Chemistry: Materials Horizons Journal, Issue 2, (2019), London, (2019), pp. 2 – 25. https://doi.org/10.1039/C8MH01062E

[25] O. Tangsirinaruenart, G. Stylios, A Novel Textile Stitch-Based Strain Sensor for Wearable End Users, In: MDPI - Multidisciplinary Digital Publishing Institute, Materials, Volume 12, 2019, Basel, (2019) pp. 2 – 17. https://doi.org/0.3390/ma12091469

[26] M. Ruppert-Stroescu, M. Balasubramanian, Effects of stitch classes on the electrical properties of conducive threads, In: SAGE Publications, Textile Research Journal, Vol.88(21), Thousand Oaks – California, (2017), pp. 2455 – 2463. https://doi.org/10.1177/0040517517725116

[27] A. Vogl, P. Parzer, T. Babic, J. Leong, A. Olwal, M. Haller, StretchEBand: Enabling Fabric-based Interactions through Rapid Fabrication of Textile Stretch Sensors, in: Association For Computing Machinery (publisher), proceedings of the 2017 CHI Conference on Human Factors in Computing Systems, New York, (2017), pp. 2617 – 2627. https://doi.org/10.1145/3025453.3025938

[28] M. Martinez-Estrada, I. Gil, R. Fernández-García, Raúl, An Alternative Method to Develop Embroidery Textile Strain Sensors, In: MDPI - Multidisciplinary Digital Publishing Institute (publisher), Textiles 2021, Volume 1, Basel, (2021), pp. 506 – 511. https://doi.org/10.3390/textiles1030026

[29] E. Dupler, L. Dunne, Effects of the Textile-Sensor Interface on Stitched Strain Sensor Performance In: Association For Computing Machinery (publisher), ISWC'19: proceedings of the 2019 ACM International Symposium on Wearable Computers, New York, (2019), pp. 48 – 52. https://doi.org/10.1145/3341163.3347717

ACTA TECHNICA JAURINENSIS
Vol. 17, No. 1, pp. 36-44, 2024
10.14513/actatechjaur.00731

Soft computing implementations for evaluating Los Angeles abrasion value of rock aggregates from Kütahya, Turkey

Ekin Köken[1, *]

[1]Nanotechnology Engineering Department, Abdullah Gul University, Kocasinan, 38100, Kayseri – Turkey
*e-mail: ekin.koken@agu.edu.tr

Submitted: 10/01/2024 *Accepted: 12/02/2024* *Published online: 28/02/2024*

Abstract: The Los Angeles abrasion value (LAAV) of rocks is a critical mechanical aggregate property for designing road infrastructures and concrete quality. However, the determination of this critical aggregate property is labour-intensive and time-consuming and thus, in the literature, there are many predictive models to estimate the LAAV for different rock types. However, most of them are based on classical regression analyses, limiting their broader usage. In this study, several soft computing analyses are performed to develop robust predictive models for the evaluation of LAAV of rocks in the Ilıca region (Kütahya – Turkey). The main motivation for implementing soft computing analyses is that precise predictive models might be useful when exploring suitable rock types that are manufactured in crushing–screening plants. For this purpose, a comprehensive laboratory schedule was established to obtain some inputs for the evaluation of LAAV. As a result of the soft computing analyses, four robust predictive models are developed based on artificial neural networks (ANN), multiple adaptive regression spline (MARS), adaptive neuro-fuzzy inference system (ANFIS) and gene expression programming (GEP) methodologies. The performance of the proposed models is investigated by some statistical indicators such as R^2 and RMSE values and scatter plots. As a result, the ANFIS-based predictive model turns out to be the best alternative to estimate the LAAV of the investigated rocks.

Keywords: Los Angeles abrasion value (LAAV), rock aggregate properties, predictive model, soft computing.

I. INTRODUCTION

The construction and building sector, which are driving forces in expanding economies, creates a substantial demand for goods and services, including many subsectors [1, 2]. One of the subsectors that plays a crucial role in geoengineering projects is the rock aggregate industry. The demand for construction aggregates, in this regard, can be evaluated based on three different groups regarding their origin (i.e., igneous, metamorphic, and sedimentary rocks). For example, rock aggregates with specific size fractions are obtained from igneous rocks such as andesite, basalt, syenite, gabbro and granite [3, 4]. Rock aggregates suitable for technical requirements are used in some infrastructures, such as water storage filtration and distribution systems and waste collection-treatment plants, and in some superstructures, such as buildings, bridges, railways, highways, etc [5−7].

To overcome stability issues in aggregate-related engineering structures, rock aggregates should withstand crushing, fragmentation, and deterioration when stacked, compressed, and subjected to surcharge loads. [8].

For this reason, the suitability of rock aggregates for use in the construction industry has been investigated through several testing methods such as aggregate impact value (AIV), aggregate crushing value (ACV), Los Angeles abrasion value (LAAV), Micro-Deval abrasion value (MDAV) [9–12].

Of the above-mentioned testing methods, LAAV and MDAL are well-accepted rock aggregate properties for evaluating rock aggregate suitability [7, 13–15]. However, these tests are hard to perform and necessitate unique graded samples. It was also reported that the LAAV test is labour-intensive and time-consuming. Therefore, numerous theories have been postulated to estimate the LAAV for different rock types [10, 14, 16–22]. However, most of these studies are based on classical regression analyses, limiting their broader use.

Nevertheless, it should be mentioned that artificial intelligence methods such as Adaptive Neuro-Fuzzy Inference Systems (ANFIS), Artificial Neural Networks (ANN), Multivariate Adaptive Regression

Splines (MARS), Support Vector Machine (SVR), and Gene Expression Programming (GEP) are more sensitive to large datasets. Thus, they can provide better results compared to classical regression analyses [23, 24].

Based on the above comments, the present study aims to establish several predictive models to estimate the LAAV of rock aggregates in Ilıca region (Kütahya–Turkey). For this purpose, detailed laboratory studies are carried out to create a comprehensive database for soft computing analyses. Based on the ANFIS, ANN, MARS and GEP methodologies, four different predictive models are introduced in this study. The performance of these models is compared based on different statistical indicators.

The details and critical notes on how to implement these methodologies used to estimate the LAAV of the investigated rocks can be found in this research paper.

II. MATERIALS AND METHODS

The investigated rock types are exposed in the northeast part of Kütahya, Turkey (**Fig. 1**). These rock types are identified in the Miocene aged Tavşanlı volcanites, and they are mainly andesites, basalts, and basaltic andesites in lithology [25].

The investigated rocks have been considered as dimension stones and rock aggregate resources in the region. For laboratory studies, representative rock blocks are obtained from several locations around the Ilıca region.

During field observations, only unweathered rock blocks were obtained to mitigate the effects of weathering on rock engineering properties. While doing this, the qualitative approach suggested by the International Society of Rock Mechanics [26] was adopted to determine the weathering degree of rocks.

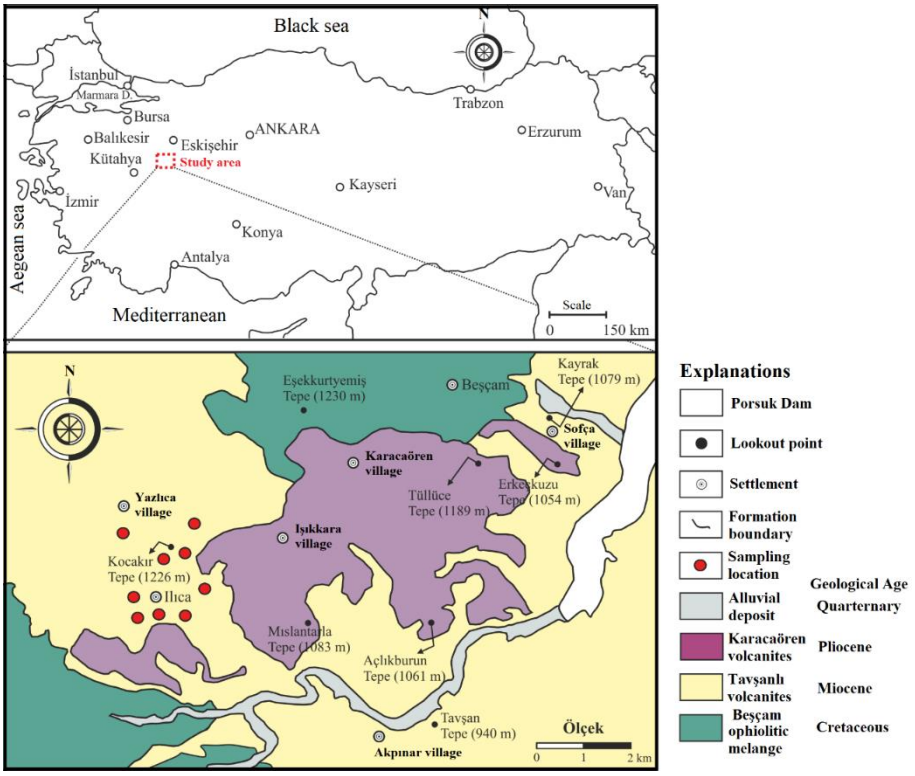

Figure 1. *Sampling locations and geological settings of the study area*

A total of 29 representative rock blocks were obtained for laboratory studies. For each rock block, physical and mechanical rock aggregate properties were determined. The laboratory studies were performed under oven-dried conditions. Each test was repeated at least three times, and average values were presented in this study.

III. LABORATORY STUDIES

The physical properties of rock aggregate consist of dry density (ρ_d) and water absorption by weight (w_a). These tests were performed by considering TS EN 1936 [27]. The mechanical rock aggregate properties considered in this study were AIV and LAAV.

These tests were also performed according to BS 812-112 [28] and TS EN 1097-2 [29], respectively. Laboratory test results are listed in **Table 1**. Accordingly, ρ_d, w_a, AIV and LAAV values were found to be between 2.59–2.74 g/cm^3, 1.19–3.80%, 12.01–24.43% and 12.27–25.46%, respectively.

Based on the database given in **Table 1**, soft computing analyses were performed.

Table 1. *Laboratory test results*

Lithology	ρ_d (g/cm^3)	w_a (%)	AIV (%)	LAAV (%)
Basalt	2.72	1.69	17.67	18.58
	2.67	1.91	16.40	21.14
	2.71	1.48	16.46	13.46
	2.72	1.71	13.10	15.25
	2.69	1.80	17.56	18.48
	2.67	2.46	17.10	23.72
	2.73	1.65	16.27	20.08
	2.69	2.70	23.96	25.46
	2.70	1.87	13.21	13.49
	2.71	1.60	15.74	16.78
	2.74	1.57	15.47	13.10
	2.73	1.45	15.02	17.97
	2.74	1.43	12.01	15.16
	2.74	1.59	14.28	12.27
	2.70	1.96	17.01	18.90
Basaltic andesite	2.71	2.15	12.33	15.46
	2.70	1.62	13.48	14.67
	2.71	1.96	20.77	23.45
	2.73	1.52	14.12	17.13
	2.67	2.53	17.51	20.31
	2.74	1.19	15.45	16.51
	2.69	2.28	14.11	17.12
	2.72	1.35	18.57	16.88
	2.68	2.05	21.31	23.90
Andesite	2.59	3.80	24.43	25.22
	2.61	1.93	18.58	18.76
	2.69	1.83	19.98	21.13
	2.62	1.90	21.25	20.39
	2.62	2.47	18.98	24.35

Explanations: ρ_d: dry density, w_a: water absorption by weight, AIV: aggregate impact value, LAAV: Los Angeles abrasion value

IV. SOFT COMPUTING ANALYSES

In this section, different soft computing methods, such as ANN, MARS, ANFIS, and GEP methodologies, were introduced.

For all methodologies, the input parameters are ρ_d, w_a and AIV with several combinations. Brief explanations of the adopted methodologies are given in the following subtitles.

1. Artificial neural networks (ANN)

Artificial Neural Networks (ANN) have gained popularity for their ability to predict dependent variables based on complex datasets.

Neural networks are commonly used in various engineering applications. In practice, they are trained through a feedforward backpropagation algorithm [30]. In this study, the neural network toolbox (nntool) was used to reveal a robust predictive model in the MATLAB environment. For this purpose, the dataset (**Table 1**) was randomly divided into training (70/100) and testing (30/100) datasets.

Various ANN architectures have been attempted to obtain the best predictive model. Before performing the analyses, the dataset was normalized between −1 and 1 to overcome overfitting problems. This normalization process is performed using Eq 1.

$$V_n = 2 \otimes \frac{X_i - X_{\min}}{X_{\max} - X_{\min}} - 1 \qquad (1)$$

Where V_n is the normalized data, x_i is the data to be normalized, x_{min} is the minimum value in the dataset, and x_{max} is the maximum value in the dataset.

After the normalization process, the dataset was loaded into the MATLAB environment to perform the neural network analyses. The analyses remained until the minimum error was obtained. Herein, root means square error (RMSE) was adopted as an error metric. Based on the analysis results, the most feasible ANN model was formulated by using the weights and biases extracted from the ANN outputs.

2. Multiple Adaptive Regression Spline (MARS)

MARS was first proposed by Friedman [31] as a nonparametric regression model. There are two important components in typical MARS models. The first one is the forward pass, and the other one is the backward pass. In the forward pass, the analyses are initiated with constant terms called basis functions (BFs). In the second part, BFs are connected to each other by employing linear regression models. It is a simple but powerful methodology to deal with datasets with a number of independent variables. MARS analyses were performed using software R, and details on the MARS-based predictive model are introduced in the following section.

3. Adaptive neuro-fuzzy inference system (ANFIS)

ANFIS is a hybrid approach that combines the fuzzy logic inference system (FIS) and ANN to establish a more efficient and accurate system.

In most ANFIS models, the Sugeno fuzzy reasoning algorithm is adopted based on numerous

membership functions [32, 33]. Similar to the ANN analyses, ANFIS models were run using MATLAB R2021b. Input parameters are represented by several Gaussian membership functions. Based on several if-then rules, a novel ANFIS-based predictive model is proposed in this study.

4. Gene expression programming (GEP)

GEP is another soft computing algorithm that uses evolutionary techniques to develop a mathematical formula which represents the relationship between the dependent and independent variables.

The GEP was developed by Ferreira [34] and has gained popularity in most geoengineering publications [35–37]. The GEP analyses were performed using GeneXproTools. Several numbers of chromosomes, head sizes and gene sizes were attempted to obtain the most feasible GEP model.

V. Results and Discussion

1. ANN analysis results

Based on several ANN analyses, the best ANN architecture was found to be 3–4–1. It means that there were three inputs (ρ_d, w_a and AIV), four hidden layers and one output (LAAV) (**Fig. 2**).

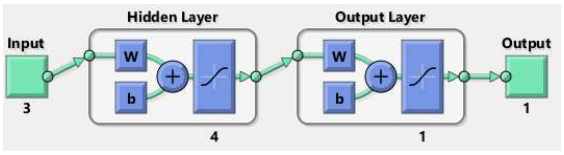

Figure 2. *ANN architecture adopted in this study.*

The mathematical formulations of the proposed ANN model were revealed by considering the deterministic approach provided by Das [38], which is given by Eq 2.

$$Y = f_{sig}\left\{b_0 + \sum_{j=1}^{n}\left[w_j \times f_{sig}\left(b_{hj} + \sum_{i=1}^{m} w_{ij} \times \delta_i\right)\right]\right\} \quad (2)$$

where Y is the output variable (LAAV), b_0 is the bias in the output layer, n is the number of neurons in the hidden layer (n=4 in this study), j denotes a specific neuron in the hidden layer, w_j is the weight of the connection between the j^{th} hidden layer and the single output neuron, b_{hj} is the bias in the j^{th} neuron of the hidden layer, w_{ij} is the weight of the connection between the i^{th} input parameter and the j^{th} hidden layer, δ_i is the normalized input parameter, f_{sig} is the nonlinear transfer function (tanh).

Based on the above deterministic approach, the LAAV can be estimated by the equations (Eqs 3 – 10). To estimate the LAAV of the investigated rocks, these equations can be easily implemented by coding them into any computational language.

$$LAAV = 6.595\tanh\left(\sum_{i=1}^{4} A_i - 0.2747\right) + 18.865 \quad (3)$$

$$A_1 = 1.2173\tanh\left(2.8187^n \rho_d + 0.85004^n w_a + 3.6887^n AIV - 0.5154\right) \quad (4)$$

$$A_2 = -1.2866\tanh\left(-0.15365^n \rho_d - 2.9709^n w_a - 0.06788^n AIV - 1.1679\right) \quad (5)$$

$$A_3 = 2.1584\tanh\left(-1.891^n \rho_d - 1.507^n w_a - 2.1233^n AIV - 0.90154\right) \quad (6)$$

$$A_4 = 1.9491\tanh\left(3.5233^n \rho_d + 0.42358^n w_a + 5.3114^n AIV + 2.5011\right) \quad (7)$$

Normalization functions:

$$^n\rho_d = 13.333\rho_d - 35.533 \quad (8)$$

$$^n w_a = 0.7663 w_a - 1.9119 \quad (9)$$

$$^n AIV = 0.161 AIV - 2.934 \quad (10)$$

2. MARS analyses results

Based on four BFs, the LAAV can also be investigated considering the MARS methodology. Accordingly, the LAAV can also be estimated by the following equations. The BFs listed in Eqs 12 – 15 are based on the global maxima (max function) in terms of different input parameters.

$$LAAV = 15.19 + 0.89BF1 - 121.55BF6 - 133.58BF9 \quad (11)$$

$$BF1 = \max\left(0; AIV - 12.01\right) \quad (12)$$

$$BF6 = \max\left(0; \rho_d - 2.73\right) \times BF1 \quad (13)$$

$$BF7 = \max\left(0; 2.73 - \rho_d\right) \times BF1 \quad (14)$$

$$BF9 = \max\left(0; 1.87 - w_a\right) \times BF7 \quad (15)$$

3. ANFIS analyses results

In the context of the ANFIS analyses, three input parameters were considered (**Fig. 3a**). During the training process, RMSE was adopted as an error metric.

The ANFIS analyses were performed until the minimum RMSE values were obtained (**Fig. 3b**). According to the ANFIS model structure (**Fig. 3c**), each input parameter was represented by five novel Gaussian membership functions. Consequently, five if-then rules activated the ANFIS model (**Fig. 3d**).

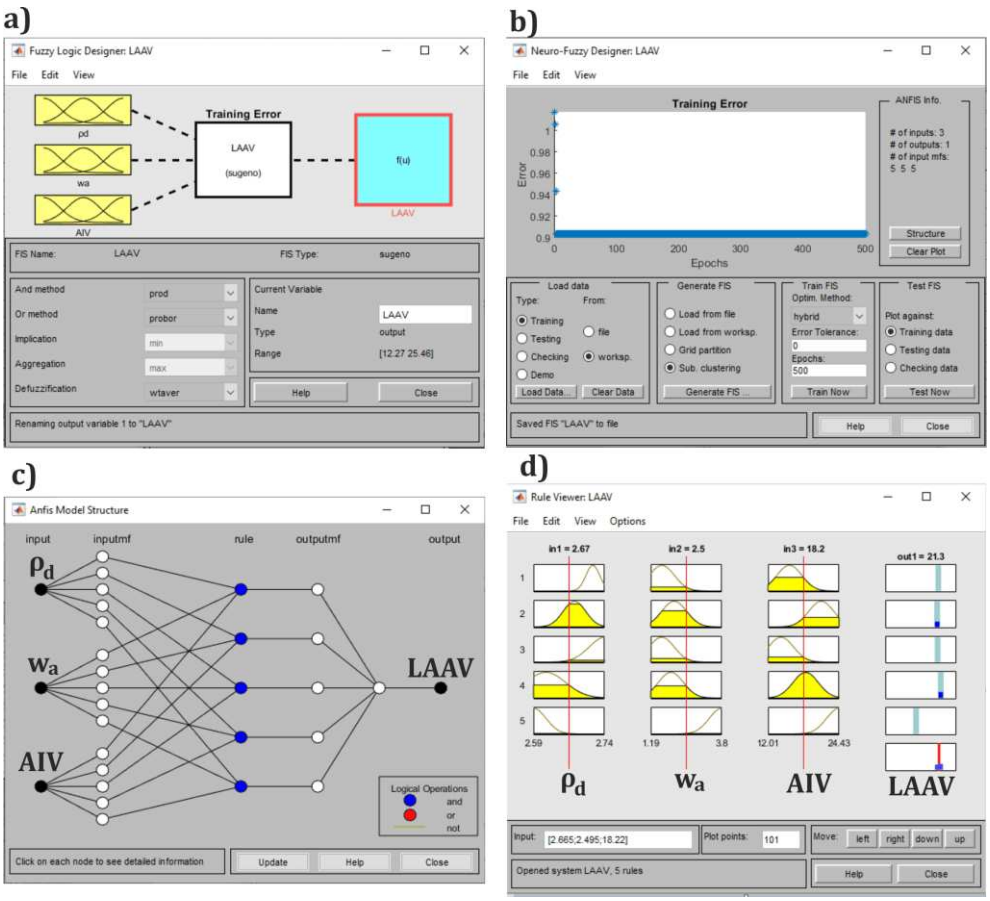

Figure 3. *ANFIS outputs a) Input parameters b) Training process c) ANFIS model structure d) Rule viewer*

4. GEP analyses results

Based on GEP analyses, the last predictive model was proposed. The sub-expression trees (Sub-ETs) are given in **Fig. 4**. The mathematical expressions of these Sub-ETs are also listed in Eqs 16 – 19.

$$LAAV = 0.9872\sum_{i=1}^{3} A_i + 0.1719 \tag{16}$$

$$A_1 = \max\left(\left(\min\left(2.46, w_a\right)\right)^2, 2.53\right) \tag{17}$$

$$A_2 = \frac{\frac{\frac{w_a + AIV}{2} + AIV}{2} + \min\left(w_a, 2.47\right)}{2} \tag{18}$$

$$A_3 = \frac{\left(w_a{}^2 \times -0.499\right) + \left(-0.133 + AIV\right)}{2} \tag{19}$$

By implementing the above equations, LAAV values can be easily estimated. The performance of the proposed predictive models is also investigated based on several statistical indicators, which are given in the following section.

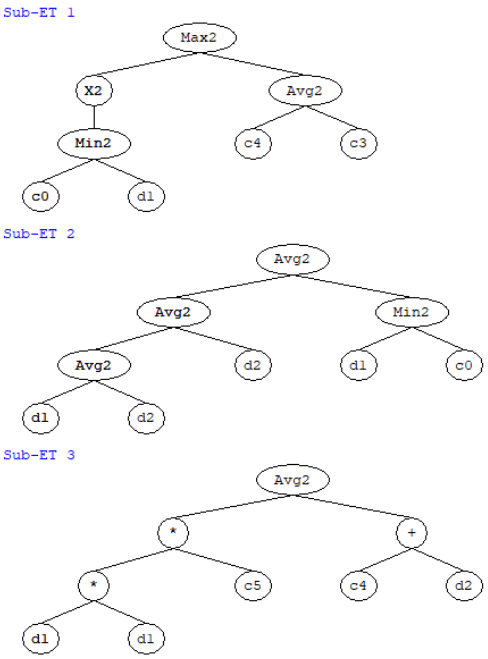

Figure 4. *Sub-ETs of the proposed GEP model (d_0: ρ_d, d1: w_a, d_2: AIV, g_1c_0: 2.469, g_1c_3: 2.527, g_1c4: 2.528, g_2c_0: 2.469, g_3c_4: −0.133, g_3c_5: −0.499).*

5. Performance Evaluation

The performance of the proposed predictive models is investigated based on several statistical indicators, such as correlation of determination (R^2) and RMSE values. The statistical indicators are calculated by the following equations:

$$R^2 = \frac{n\sum xy - \sum x \sum y}{\sqrt{n\sum x^2 - \left(\sum x\right)^2}\sqrt{n\sum y^2 - \left(\sum y\right)^2}} \quad (20)$$

$$RMSE = \sqrt{\frac{\sum_{i=1}^{n}\left(y_i - x_i\right)^2}{n}} \quad (21)$$

Where x is the predicted variable, y is the measured variable, and n is the number of datasets.

Focusing on the training (70/100) and testing (30/100) datasets, the R^2 and RMSE values are listed in **Table 2.**

Table 2. *Performance indicators of the proposed predictive models*

Methodology	Training dataset		Testing dataset	
	R^2	RMSE (%)	R^2	RMSE (%)
ANN	0.81	1.624	0.98	0.296
MARS	0.86	1.523	0.72	2.096
ANFIS	0.92	1.042	0.98	0.468
GEP	0.72	1.965	0.86	1.295

Accordingly, for training and testing datasets, the R^2 and RMSE values were found to be between 0.72–0.98 and 0.296–2.096%, respectively (**Table 2**). Based on the calculated performance indices, the ANFIS-based predictive model provides the best prediction performance when considering the whole dataset. On the other hand, the ANN-based predictive model, with its explicit mathematical formulations, can also be regarded as a concise model to estimate the LAAV of the investigated rocks. The scatter plots of the models are also given in **Fig. 5**. In **Fig. 5**, the performance of the predictive models is illustrated by focusing on the whole dataset (n=29).

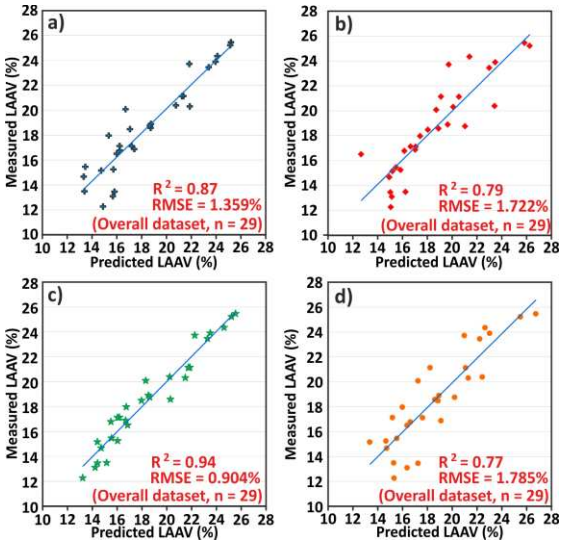

Figure 5. *Scatter plots of the proposed predictive models a) ANN b) MARS c) ANFIS d) GEP*

Similar to what has been stated earlier, the scatter plots also suggest that the ANFIS-based predictive model provides concise LAAV values and, thus, this methodology can be regarded as a robust methodology for the evaluation of LAAV. However, this methodology can have some difficulties in that it is a black-box model, and there are no definite mathematical expressions as an output in the ANFIS analyses. It should be herein mentioned that the outputs were extracted from the ANFIS model based on some computational commands (e.g., evalfis) in the MATLAB environment.

When explicit mathematical formulations are desired to estimate the LAAV of rocks, the ANN-based predictive model (Eqs. 3–10) can also be a coherent choice.

On the other hand, the GEP and MARS models should be improved by enhancing the number of datasets. These models often provide more accurate results by considering larger datasets.

6. Conclusions

In this study, robust predictive models are introduced to estimate the LAAV of the rocks in the Ilıca region (Kütahya–Turkey). For this purpose, a

comprehensive laboratory schedule was established to obtain some inputs for the evaluation of LAAV. Consequently, a database composed of 29 datasets was generated (**Table 1**). As a result of the soft computing analyses, four robust predictive models are developed. The performance of the proposed models is investigated by some statistical indicators such as R^2 and RMSE values and scatter plots. As a result, the ANFIS-based predictive model turns out to be the best alternative to estimate the LAAV of the investigated rocks. Nevertheless, in this study, some explicit mathematical formulations are also provided based on the ANN methodology. This model can also be considered and coded into any computation language for its possible implementations. Last but not least, the MARS and GEP models should be improved by enhancing the database and adding some input parameters such as mineralogical features and/or quantitative knowledge on rock weathering.

It is highly recommended to investigate the weathering degree of the rocks exposed in the Ilıca region. In this way, the physical and mechanical aggregate properties and their possible variations can be thoroughly revealed. The findings obtained from the present study and recommendations stated are believed to be beneficial for the evaluation of LAAV for the investigated rock types.

AUTHOR CONTRIBUTIONS

E. Köken: Conceptualization, Experiments, Analyses, Writing, Review and Editing.

DISCLOSURE STATEMENT

The author declares that he has no known competing financial interests or personal relationships that could have appeared to influence the work reported in this paper.

ORCID

Ekin Köken https://orcid.org/0000-0003-0178-329X

REFERENCES

[1] Rajprasad, J., & Pannirselvam, N. (2020, November). Optimizing the properties of treated recycled aggregate concrete. In AIP Conference Proceedings (Vol. 2277, No. 1). AIP Publishing, https://doi.org/10.14513/actatechjaur.v10.n2.446

[2] Přikryl, R. (2021). Geomaterials as construction aggregates: a state-of-the-art. Bulletin of Engineering Geology and the Environment, 80, 8831-8845, https://doi.org/10.1007/s10064-021-02488-9

[3] Blengini, G. A., Garbarino, E., Šolar, S., Shields, D. J., Hámor, T., Vinai, R., & Agioutantis, Z. (2012). Life Cycle Assessment guidelines for the sustainable production and recycling of aggregates: the Sustainable Aggregates Resource Management project (SARMa). Journal of Cleaner Production, 27, 177-181, https://doi.org/10.1016/j.jclepro.2012.01.020

[4] Brown T. (2019) Mineral Planning Factsheet Construction Aggregates, British Geological Survey, BGS, 32 pp, http://nora.nerc.ac.uk/id/eprint/524079/1/aggregates_2019.pdf

[5] Langer, W. (2016). Sustainability of aggregates in construction. In Sustainability of construction materials (pp. 181-207). Woodhead Publishing, https://doi.org/10.1016/B978-0-08-100370-1.00009-3

[6] Karim, Y., Khan, Z., Alsoufi, M. S., & Yunus, M. (2016). A review on recycled aggregates for the construction industry. American Journal of Civil Engineering and Architecture, 4(1), 32-38

[7] Juhász, E., & Fischer, S. (2019). Railroad ballast particle breakage with unique laboratory test method. Acta Technica Jaurinensis, 12(1), 26-54, https://doi.org/10.14513/actatechjaur.v12.n1.489

[8] Wu, Y., Parker, F., & Kandhal, P. S. (1998). Aggregate toughness/abrasion resistance and durability/soundness tests related to asphalt concrete performance in pavements. Transportation Research Record, 1638(1), 85-93, https://doi.org/10.3141/1638-10

[9] Kamani, M., & Ajalloeian, R. (2020). The effect of rock crusher and rock type on the aggregate shape. Construction and Building Materials, 230, 117016, https://doi.org/10.1016/j.conbuildmat.2019.117016

[10] Al-Harthi, A.A. A field index to determine the strength characteristics of crushed aggregate. Bull Eng Geol Environ 60, 193–200 (2001). https://doi.org/10.1007/s100640100107

[11] Köken, E. (2022). Assessment of Los Angeles Abrasion Value (LAAV) and Magnesium Sulphate Soundness (Mwl) of Rock Aggregates Using Gene Expression Programming and Artificial Neural Networks. Archives of Mining Sciences, 401-422, https://doi.org/10.24425/ams.2022.142407

[12] Adomako, S., Engelsen, C. J., Thorstensen, R. T., & Barbieri, D. M. (2021). Review of the relationship between aggregates geology and

Los Angeles and micro-Deval tests. Bulletin of Engineering Geology and the Environment, 80, 1963-1980.

[13] McNally G H (1998) Soil and Rock Construction Materials. E&FN SPON, ISBN: 9780419214205

[14] Ajalloeian, R., Kamani, M. An investigation of the relationship between Los Angeles abrasion loss and rock texture for carbonate aggregates. Bull Eng Geol Environ 78, 1555–1563 (2019). https://doi.org/10.1007/s10064-017-1209-y

[15] Tanyu, B. F., Yavuz, A. B., & Ullah, S. (2017). A parametric study to improve suitability of micro-deval test to assess unbound base course aggregates. Construction and Building Materials, 147, 328-338, https://doi.org/10.1016/j.conbuildmat.2017.04.173

[16] Kahraman, S., Gunaydin, O. Empirical methods to predict the abrasion resistance of rock aggregates. Bull Eng Geol Environ 66, 449–455 (2007). https://doi.org/10.1007/s10064-007-0093-2

[17] Khaleghi Esfahani, M., Kamani, M. & Ajalloeian, R. An investigation of the general relationships between abrasion resistance of aggregates and rock aggregate properties. Bull Eng Geol Environ 78, 3959–3968 (2019). https://doi.org/10.1007/s10064-018-1366-7

[18] Kahraman, S. A. İ. R., & Fener, M. (2007). Predicting the Los Angeles abrasion loss of rock aggregates from the uniaxial compressive strength. Materials Letters, 61(26), 4861-4865, https://doi.org/10.1016/j.matlet.2007.06.003

[19] Rigopoulos, I., Tsikouras, B., Pomonis, P., & Hatzipanagiotou, K. (2013). Determination of the interrelations between the engineering parameters of construction aggregates from ophiolite complexes of Greece using factor analysis. Construction and Building Materials, 49, 747-757, https://doi.org/10.1016/j.conbuildmat.2013.08.065

[20] Palassi, M., Danesh, A. Relationships Between Abrasion/Degradation of Aggregate Evaluated from Various Tests and the Effect of Saturation. Rock Mech Rock Eng 49, 2937–2943 (2016). https://doi.org/10.1007/s00603-015-0869-9

[21] Apaydın, Ö.F., Yılmaz, M. Correlation of petrographic and chemical characteristics with strength and durability of basalts as railway aggregates determined by ballast fouling. Bull Eng Geol Environ 80, 4197–4205 (2021). https://doi.org/10.1007/s10064-019-01654-4

[22] Gökalp, İ., Kaya, O., & Uz, V. E. (2023). Relationship Between Abrasion, Fragmentation and Thermal Weathering Resistance of Aggregates: Regression and Artificial Neural Network Analyses. International Journal of Pavement Research and Technology, 1-12, https://doi.org/10.1007/s42947-023-00336-5

[23] Mohamad, E.T., Jahed Armaghani, D., Momeni, E. et al. Prediction of the unconfined compressive strength of soft rocks: a PSO-based ANN approach. Bull Eng Geol Environ 74, 745–757 (2015). https://doi.org/10.1007/s10064-014-0638-0

[24] Mishra, D. A., Srigyan, M., Basu, A., & Rokade, P. J. (2015). Soft computing methods for estimating the uniaxial compressive strength of intact rock from index tests. International Journal of Rock Mechanics and Mining Sciences, 80, 418-424, https://doi.org/10.1016/j.ijrmms.2015.10.012

[25] Türkmenoğlu, A. G., & Yavuz-Işık, N. (2008). Mineralogy, chemistry and potential utilization of clays from coal deposits in the Kütahya province, Western Turkey. Applied Clay Science, 42(1-2), 63-73, https://doi.org/10.1016/j.clay.2007.11.006

[26] ISRM (2007) The complete ISRM suggested methods for rock characterization, testing and monitoring: 1974–2006. In: Ulusay R, Hudson JA (eds) Suggested methods prepared by the commission on testing methods. 2007 International Society for Rock Mechanics (ISRM), Ankara, Turkey

[27] TS EN 1936 (2007) Natural stone test methods – Determination of real density and apparent density, and of total and open porosity, Turkish Standards Institution, Ankara – Turkey.

[28] BS 812-112, British standard: Testing aggregates, method for determination of aggregate impact value (AIV), (1990)

[29] TS EN 1097-2, Tests for mechanical and physical properties of aggregates – Part 2: Methods for the determination of resistance to fragmentation. Turkish Standards Institution, Ankara, (2010).

[30] Saravanan, K., & Sasithra, S. (2014). Review on classification based on artificial neural networks. Int J Ambient Syst Appl, 2(4), 11-18, https://doi.org/10.5121/ijasa.2014.2402

[31] Friedman, J. H. (1991). Multivariate adaptive regression splines. The annals of statistics, 19(1), 1-67.

[32] Köken, E., Kadakçı Koca, T. Evaluation of Soft Computing Methods for Estimating Tangential Young Modulus of Intact Rock Based on Statistical Performance Indices. Geotech Geol Eng 40, 3619–3631 (2022). https://doi.org/10.1007/s10706-022-02112-x

[33] Cortés-Antonio, P., Batyrshin, I., Martínez-Cruz, A., Villa-Vargas, L. A., Ramírez-Salinas, M. A., Rudas, I., ... & Molina-Lozano, H. (2020). Learning rules for Sugeno ANFIS with parametric conjunction operations. Applied Soft Computing, 89, 106095.

[34] Ferreira C (2001) Gene expression programming: a new adaptive algorithm for solving problems. Complex Syst 13(2):87–129, https://doi.org/10.48550/arXiv.cs/0102027

[35] Abdulsalam, J., Lawal, A.I., Setsepu, R.L. et al. Application of gene expression programming, artificial neural network and multilinear regression in predicting hydrochar physicochemical properties. Bioresour. Bioprocess. 7, 62 (2020). https://doi.org/10.1186/s40643-020-00350-6

[36] Köken, E., & Lawal, A. I. (2021). Investigating the effects of feeding properties on rock breakage by jaw crusher using response surface method and gene expression programming. Advanced Powder Technology, 32(5), 1521-1531, https://doi.org/10.1016/j.apt.2021.03.00

[37] İnce, İ., Bozdağ, A., Fener, M. et al. Estimation of uniaxial compressive strength of pyroclastic rocks (Cappadocia, Turkey) by gene expression programming. Arab J Geosci 12, 756 (2019). https://doi.org/10.1007/s12517-019-4953-4

[38] Das, S. K. (2013). Artificial neural networks in geotechnical engineering: modeling and application issues, Metaheuristics in water, geotechnical and transport engineering, 231–270,https://doi.org/10.1016/B978-0-12 398296-4.00010-6.

ACTA TECHNICA JAURINENSIS
Vol. 17, No. 1, pp. 45-58, 2024
10.14513/actatechjaur.00735

Influence of different factors on the value of the rail wear rate

Yurii Makarov[1,*], Roman Zaleskyi[1], Mykola Mykhalichenko[1]

[1] Railway Inspection Station PS-1 of the Branch of Railway Infrastructure Diagnostic Center Ukrzaliznytsia, JSC, Dnipro, 49038, Ukraine
*e-mail: yu.makarov@dp.uz.gov.ua

Submitted: 16/01/2024 Accepted: 16/02/2024 Published online: 28/02/2024

Abstract: The article deals with the study of the influence of train operating modes on the uphill and downhill sections with radii less than 450 m, as well as the influence of railway superstructure design in curved sections on the wear rate of rolling stock wheel flanges and rails. The aim of the research is to reduce the wear that occurs between the wheel flanges of the rolling stock and the rails. Rail joints have been found to be the main shock source in the dynamic interaction between the railway and the rolling stock. There is unstable motion within the transition curves and at the joints of the curved rail on the curved track sections. This is accompanied by abrupt lateral rail wear in the joint area between the trailing and facing rails in the direction of train movement. It has been found that reducing the weight of the trains leads to a reduction in intensive lateral rail wear on curved track sections and can reach the following percentages: in curves with a radius of up to 300 m: up to 33% uphill, up to 55% downhill; in curves with a radius of 300 m to 450 m: up to 32.9% uphill, up to 26.3% downhill; in curves with a radius of 450 m: up to 3.2% uphill, up to 17.6% downhill. On the uphill and downhill sections, reducing the height and adjusting to the speed limit in percentage gives a positive result from 4.7% to 53.59%. The results of the research can be used in rail transport industry to extend the life of rolling stock wheel sets and rails, and to improve transport safety.

Keywords: rail wear; wheel set wear; rail joint irregularities

I. INTRODUCTION

The interaction between the wheels of rolling stock and the railway superstructure is characterised by the occurrence of transverse, longitudinal and vertical forces, which cause mutual wear of wheel and rail, disturbances in the railway superstructure and in the mechanical part of the wheels of rolling stock.

The most intense interaction occurs on the curved track sections where increased longitudinal and lateral forces are generated due to the wheels of the rolling stock fitting into the curve and also due to the accelerated movement in the curve. The forces generated by the movement on the curved track sections lead to displacement and buckling of the track, wear of the wheel flanges of the locomotives and cars, wear of the outer rail of the curve.

The interaction of rolling stock and track, the factors influencing the lateral wear and the dynamic indicators when the rolling stock moves on the curved track sections have been studied by many researchers in recent years. The study focused on the influencing factors, namely the change of track gauge in curves for low and high traffic railway lines in Hungary (i.e. secondary and main lines) [1].

Also, the influence of the length of the transition curve when organising high-speed traffic and the increase of the length of the transition curve with increasing speed [2]. The evaluation and prediction of the rolling surface damage of the point frog has been studied, which can also be applied to the rail surface to ensure proper design and maintenance of both point frogs and rails [3]. The study [4] analyses the accumulation of deviations in the geometric parameters of a tramway track as a function of the axial load, with a hard surface, which is also applicable to railway tracks when the vertical and horizontal irregularities of the track increase with the tonnage transported. The article

[5] analyses the vertical and lateral rail wear and the influence of the outer rail height, the type of traction and the longitudinal profile of the track. In order to automate railway straightening systems in the horizontal and vertical planes [6], a mathematical model has been created that allows the rational determination of curve parameters during the operation of railway machines. The influence of

speed parameters and wheel damage during the transfer of vertical loads, the occurrence of vibrations during the transfer of vertical force to the subgrade and the consequences that can be caused by the influence of these factors have been studied in the work [7].

In this study, the authors considered the results of several papers addressing environmental [8] and technological issues in the field of railway transport. This includes the processes involved in fitting rolling stock into curved sections of the track, considering both vertical and horizontal deviations, and the impact of these parameters on the life cycle of infrastructure elements. The latter is directly dependent on the geometric parameters of the rail track [9]. The publication also covers the repair of rail defects with a focus on determining hardness parameters in the contact zone [10]. Additionally, it delves into the control of hardness in the zone of the joint welded by the thermite method and examines the effect of hardness when welding rails of different categories [11]. The restoration of rail lash integrity through the use of glue-bolt rail joints on Continuous Welded Rail (CWR) tracks is also discussed [12].

The purpose of this research is to continue research in this area, taking into account changes in the amount of lateral rail wear, the dependence of changes in lateral rail wear along the length of the rail in jointed and jointless tracks, and the effect of joint irregularities in the vertical and horizontal planes on lateral rail wear.

II. RESEARCH METHODOLOGY

The research has studied the amount of lateral rail wear along the length of the transition, circular and second transition curves. This was done by measuring the amount of lateral wear every metre on the first transition curve, the circular curve and the second transition curve. Lateral wear was measured every 0.2 m in the joint area. This was done at a distance of 1 metre from the trailing and facing ends. Analysis of the lateral wear of the rails on a jointed track has revealed a characteristic pattern which has been confirmed by long-term studies of the extent, shape and nature of lateral wear along the entire curve when trains are 'properly driven'. The tapes on the gauge car have been included in the research. To decipher the tapes, special software was used to analyse the values for level, track deviation, track gauge and subsidence in 0.2m increments. It has been found that the main factor influencing the lateral wear of the rails is the radius of the curve. It has been found that in curves with a radius of 600 m, the wear is 4 times less than in curves with a radius of 300 m [8]. In addition, more than 30 factors have an influence on the wear of the wheels of the rolling stock and the lateral wear of the rails on the curved track sections [9]. This article describes and analyses the following factors:

- The design of the railway superstructure (type of sleepers and fasteners, outer rail height, jointed and jointless track);
- The weight of trains;
- The operating modes of the train (traction mode, running with current; deceleration mode, running without current; braking mode);
- The curve design and profile (downhill and uphill sections with gradients greater than 10‰ and R 450 m).
- The problem of the intensive lateral wear of the rails occurs on the curved track sections with a radius of less than 450 m. The curved track sections with a radius of R 450 m of the Ukrzaliznytsia, JSC railway can be equipped as follows:
- Jointed track in curves with a radius of up to 300 m;
- Jointless track in curves with a radius of between 300 and 350 m, provided that there is a technical and economic report which is approved by the head of the railway track service;
- Jointless track in curves with a radius of 350 m or more [10].

The detailed description of each option is given below.

III. JOINTED TRACK

A jointed track with curves with a radius of less than 300 m. In curves with small radii, almost every joint has local irregularities in the horizontal and vertical planes. Rail joints are the main source of dynamic interaction between the track and rolling stock, resulting in the occurrence of additional track disturbances, track design and profile violations [11].

The processes of dynamic interaction between the rolling stock and the rail track are particularly intense in curves with small radii, accompanied by track disturbances. These processes are complicated by the heavy weight of freight trains and the gradients of the longitudinal profile.

When travelling uphill or downhill, regenerative braking generates longitudinal compressive forces in the rolling stock, with the lateral component of these forces directed outwards. The joint makes the movement of the train unstable on the curved track sections, resulting in abrupt lateral wear.

The formation of lateral rail wear accumulations on jointed and jointless tracks at transitions and in circular curves is described below. Note the accumulation of lateral rail wear that occurs on a jointed track. **Fig. 1** shows the amount of lateral wear on the first transition curve of the jointed track in the direction of train movement.

The transition curve is formed by three 25 m long rails. The transition curve shows a gradual increase

in the amount of lateral rail wear from 2 mm to 10 mm.

The maximum value of lateral rail wear is at the end of the transition curve. Uneven rail wear is observed at the joints.Note the amount of lateral rail wear at the joint.

Fig. 2 shows the actual values of lateral rail wear within the joint over a length of 1 m in both directions from the joint axis. The size of the joint gaps corresponds to the standards applied in Ukraine [12].

The maximum value of lateral rail wear is observed at a distance of 0.4 m - 0.6 m from the facing rail in the direction of train movement. The difference between the minimum and maximum wear values of the facing rail and the trailing rail is 3 mm: 8.8 mm – 0.2 m; 11.8 mm – 0.4 m; 11.8 mm – 0.6 m.

The values of lateral wear in the circular curves of the jointed track and the locations of the largest deviations observed in the circular curves are examined in more detail below (**Fig. 3**).

At the ends of the rails, i.e. the trailing ends within 1 m of each other, the maximum lateral rail wear occurs in the circular curve. Note the values of lateral wear in Fig. 4 at joint 8 (**Fig. 3**): at the point of 24.8 m the value is 10.8 mm on the trailing rail and at the points of 0.8 m and 1 m the value is 15.8 mm on the facing rail. The difference in rail wear within one metre is up to 5 mm.

Rail wear at the joints is characterized by less wear on the trailing rail and more wear on the leading rail in the circular curve of a jointed track.

Here is an analysis of the indicators of lateral rail wear in the 2nd transition curve in the direction of train movement (**Fig. 5 and 6**)

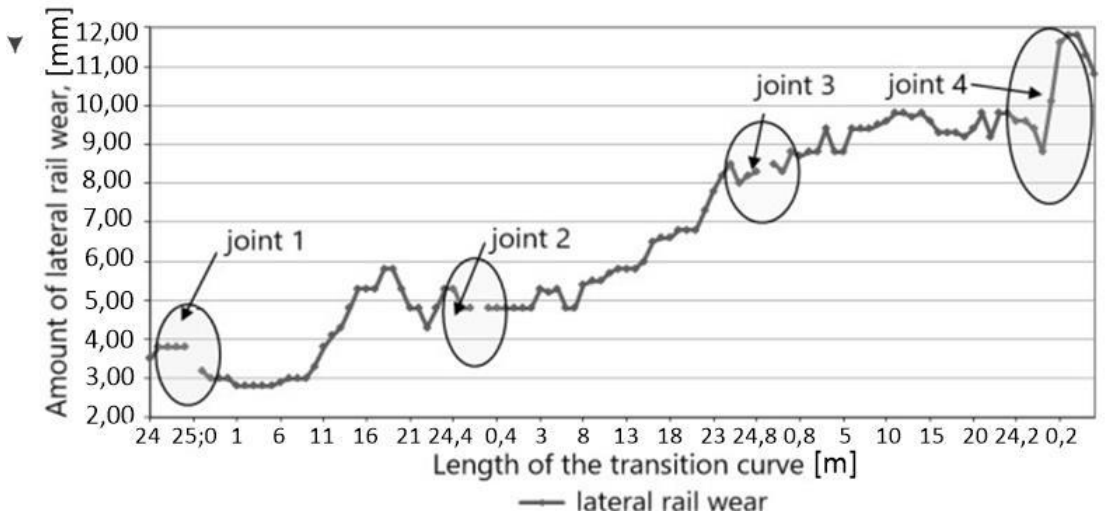

Figure 1. *The first transition curve in the direction of train movement on the jointed track*

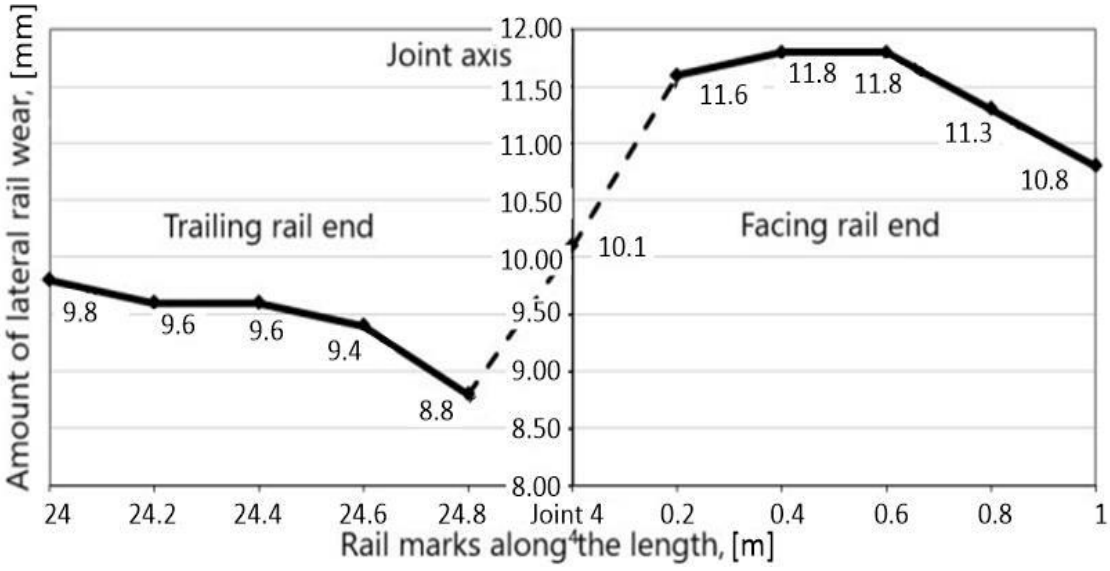

Figure 2. *Diagram of lateral wear in joint No. 4 (according to* ***Fig. 1****) of the transition curve*

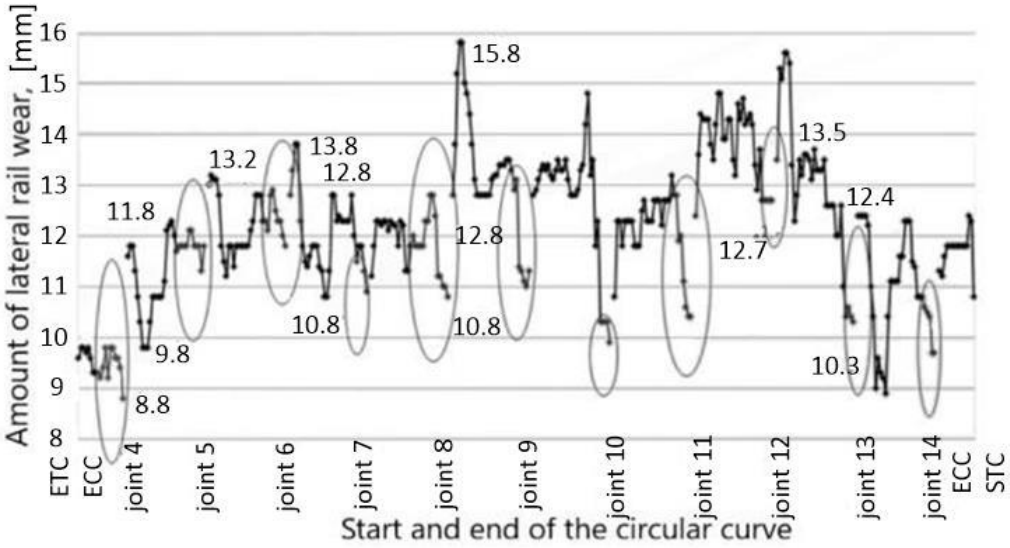

Figure 3. *Diagram of rail lateral wear in a circular curve of a jointed track*
STC – Start of the transition curve; ETC – End of the transition curve
SCC – Start of the circular curve; ECC – End of the circular curve

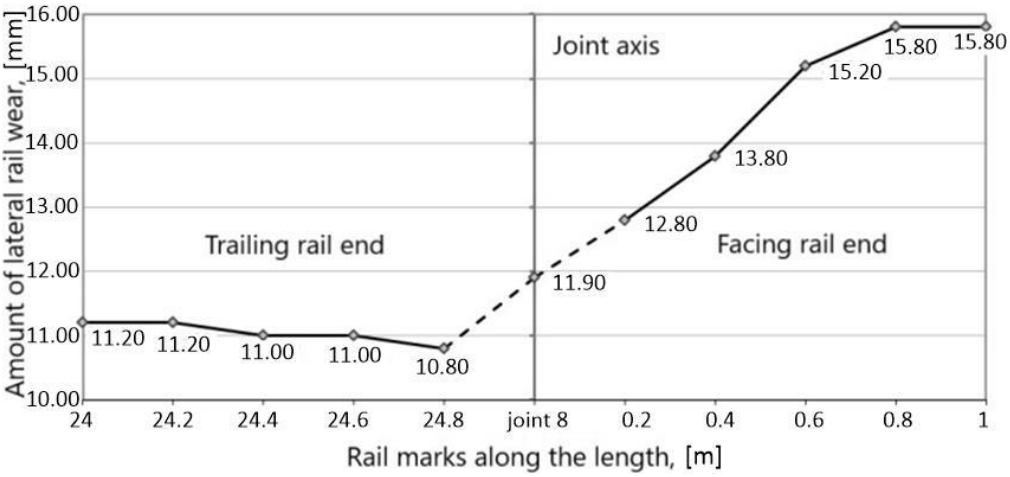

Figure 4. *Diagram of lateral wear in joint No. 8 of the circular curve*

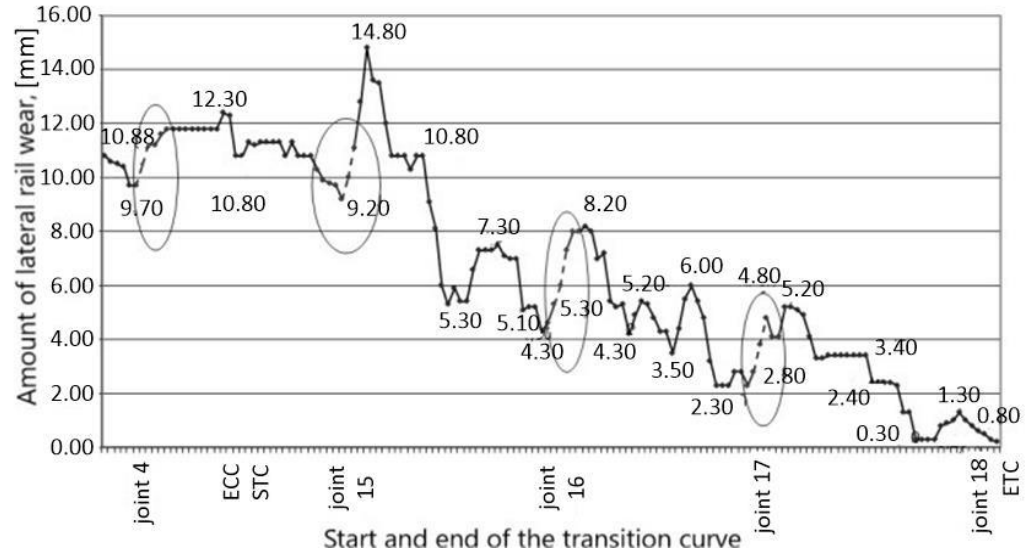

Figure 5. *Lateral rail wear in the second transition curve in the direction of train movement*

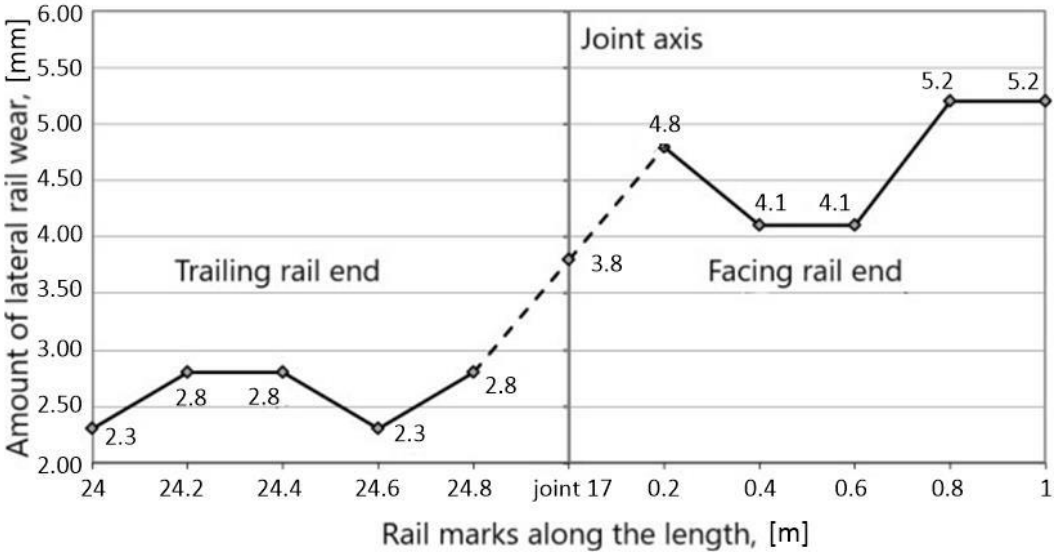

Figure 6. *The amount of the rail wear at joint No. 17 (**Fig. 5**) of the second transition curve in the direction of train movement*

In the second transition curve in the direction of train movement, the lateral rail wear gradually decreases from the circular curve with increasing radius at the exit of the curve section. There is also increased rail wear on the facing rail at a distance of 1 m and 2 m from the end of the rail.

IV. JOINTLESS TRACK

The characteristics of jointless track operation in curves with a small radius of the track are described below. Jointless track on Ukrainian railways is mainly used in curves of R 350 m and on straight sections, and only in some cases in curves of 300 m R 350 m. The main reason for this is that the stability of the jointless track decreases as the radius of the curve decreases. The loss of stability occurs at high temperatures due to the heating of the rails and the action of the compressive forces in them, which produce equal forces on each elementary section of the curve, directed outwards from the curve, i.e. in the direction of a possible ejection. The steeper the curve, the more difficult for the rolling stock into fit it, and the greater the lateral, steering and frame forces. Centrifugal force is an important factor and also increases as the radius of the curve decreases [13].

The second reason for limiting the use of jointless track in small radius curves is that the dynamic impact of rolling stock on the track increases as the radius decreases. Due to the significant dynamic stresses in the rails, their strength may not be sufficient to withstand the additional temperature stresses, which can exceed 100 MPa [14].

The third reason is the increased lateral wear of the rails in steep curves, which makes it necessary to remove the jointless rail from the track before the cost of installing the jointless track has been recouped.

For comparison, the characteristic formation and accumulation of lateral wear in the transition and circular curves of a jointless track is analysed (**Fig. 7 to 9**).

The value of the lateral rail wear in the transition curve of a jointless track is shown in **Fig.7**. The lateral wear does not show any sharp deviations at the adjacent points. Note the gradual increase in lateral rail wear and the maximum value within the transition curve to a circular curve, as observed in the transition curve of the jointed track.

In the first transition curve in the direction of train movement, the wear value at adjacent points does not exceed 2.0 mm. The variations in the lateral wear observed in the transition curve occur every 15 m to 20 m. This can be explained by the fit of the wheel sets of the rolling stock.

The largest deviations in the adjacent lateral wear points occur at the end of the first transition curve as the trains move forward. The indicators of the lateral rail wear in a circular curve of a jointless track are described in **Fig. 8**.

The indicators of lateral rail wear in the second transition curve of a jointless track in the direction of movement are shown in **Fig. 9**.

The lateral wear appears to be smoother, but it should be noted that the jump in lateral wear occurs at the end of the transition curve, as was also observed in the transition curve of the jointed track.

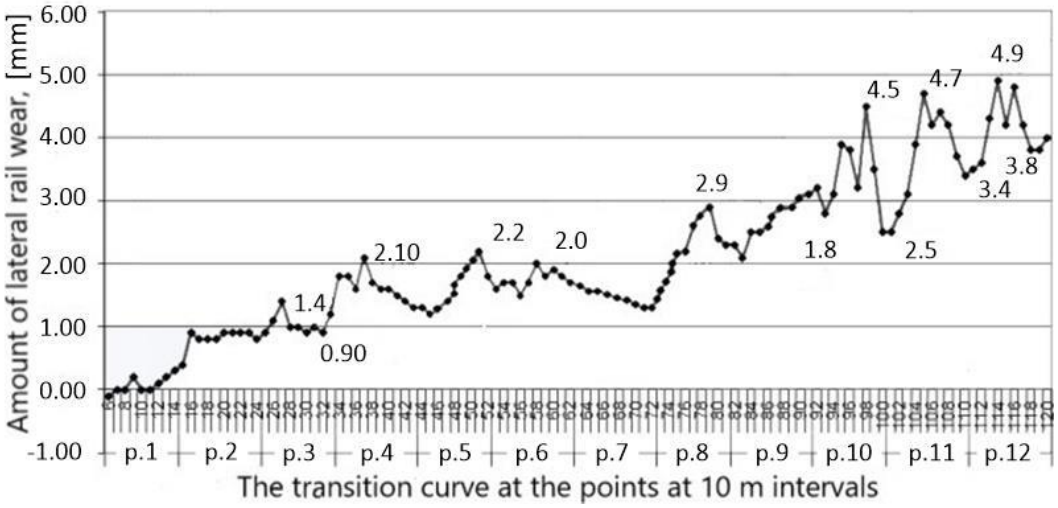

Figure 7. *Lateral rail wear in the transition curve of the jointless track*

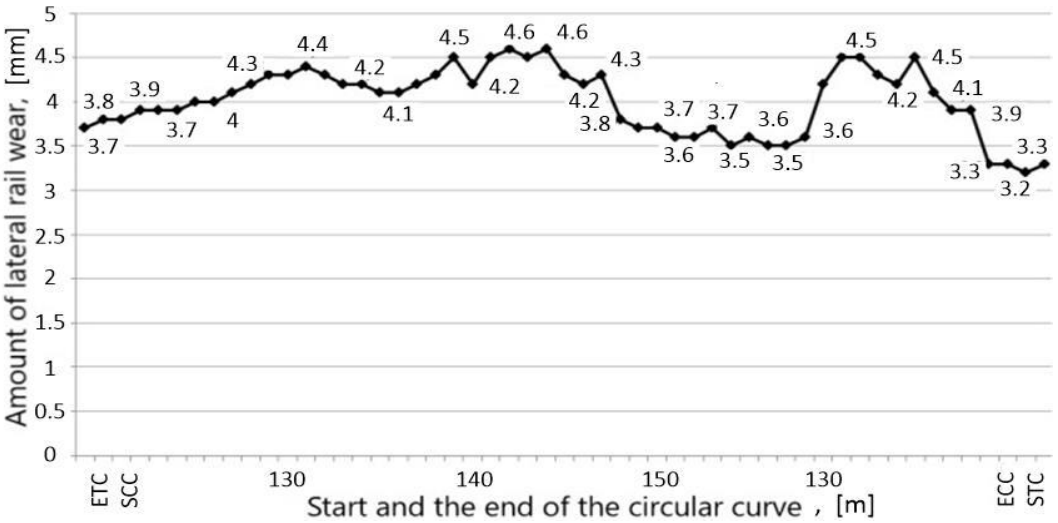

Figure 8. *Lateral rail wear values in a circular curve*

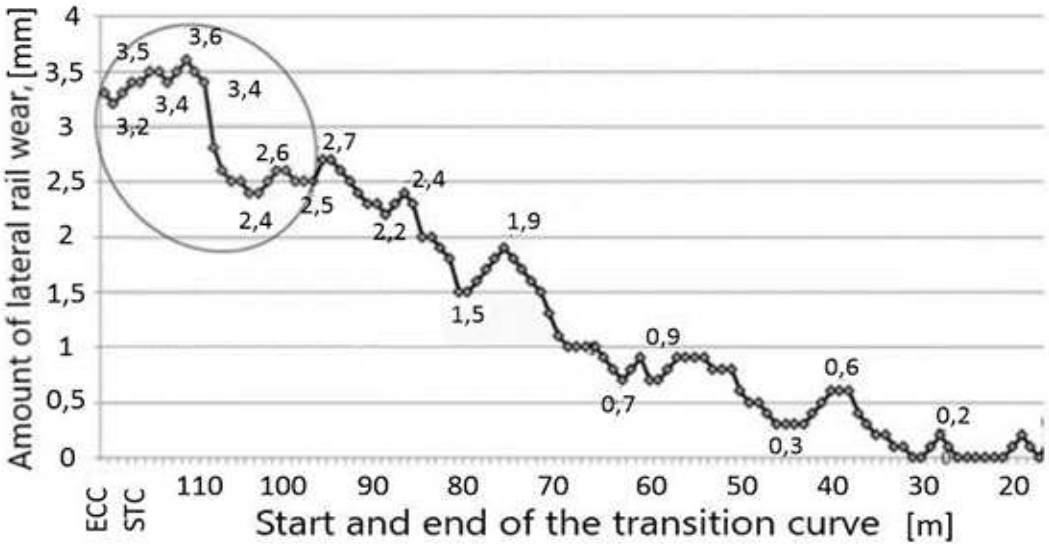

Figure 9. *Lateral wear values in the transition curve of a jointless track*

The lateral wear appears to be smoother. However, it should be noted that the jump in lateral wear occurs at the end of the transition curve, as was also observed in the transition curve of the jointed track. The maximum values of lateral wear are observed on the facing rail along the first metre, then 2 m, 3 m at the joint.

On a jointless track, the lateral wear has a smooth line. The difference between the values of the two critical points does not exceed 3.2 mm. The value between the two critical points in the circular curve on the jointed track at the joints reaches 13.5 mm.

Therefore, the fewer joints there are in the curved track sections, the smoother the train movement and the lower the level of abrupt rail wear.

V.TRACK DESIGN FEATURES IN CURVES WITH RADIUS OF R < 450 M

Under-rail sleepers are made of wood and reinforced concrete. Rails of standard lengths:

25.00 m and shortened 24.92 m, 24.84 m, as well as half-length rails: 12.50 m and shortened 12.46 m, 12.42 m, 12.38 m [15] are mostly used in Ukraine.

On the main lines of Ukrzaliznytsia, JSC, D0, D2, KPPD-2, SKD65-D, SKD65-Dm fasteners for wooden sleepers are used. The following types of fasteners are used on reinforced concrete sleepers: KB-65, KPP-5, SKD65-B, KPP-5-K.

It is not possible to adjust the gauge with D0, D2, KPPD-2, KB-65, KPP-5 fasteners unless the fasteners are removed when the track is reassembled on wooden sleepers using a template.

When KB-65 and KPP-5 fasteners are installed on reinforced concrete sleepers that cannot be adjusted to the track gauge, the track gauge at the start of service is 1520 mm, which makes it difficult to fit rolling stock on the curved track sections with small radii.

The SKD65-D, SKD65-Dm, SKD65-B and KPP-5-K rail fasteners allow track gauge adjustment up to 1535 mm, the Schwihag AG SBS W SL-1-900- R65 fastener, the Vossloh System W-30 fastener allows track gauge adjustment up to 1530 mm and the Skl 21 fastener allows track gauge adjustment up to 1535 mm.

The SKD65-B fastener ensures smooth track gauge expansion diversion by means of adjusting plates and pad turning. The total gauge deviation of the SKD65-D and SKD65-Dm fasteners is 7 mm for one line and 14 mm for two lines; the SKD65-B fasteners are 14 mm for one line and 28 mm for two lines. The SKD65-B fastener allows the rails to be used up to their maximum wear limit of 26 mm.

The KPP-5-K is designed to provide smooth extension from 1522 mm to 1534 mm in 2 mm increments. To ensure a free fit, it is necessary to make a smooth expansion in the transition curve and a stable gauge in the circular curve according to the radius [16].

According to field observations, the dependence of the intensity of lateral rail wear on different track superstructures is as follows (**Table 1**)

Table 1. *Intensity of lateral rail wear as a function of track section characteristics (UH – uphill; DH - downhill)*

Type of fastening	Lateral rail wear intensity, mm/mln t of freight																	
	R<300 m						300 m <R<450 m						450 m <R<650 m					
	up to 10‰		10 to 20‰		>20‰		up to 10‰		10 to 20‰		>20‰		up to 10‰		10 to 20‰		>20‰	
	UH	DH	UH	DH	UH	DH	UH	DH	UH	DH	UH	DH	UH	DH	UH	DH	UH	DH
D0	0.134	0.124	0.172	0.167	0.262	0.235		0.138	0.135		0.249	0.166						
D2 SKD-65D	0.259	0.161	0.329	0.257	0.272	0.257			0.185	0.166	0.280	0.143				0.024	0.138	
SKD65-B	0.342	0.473	0.361		0.456				0.190		0.246	0.267					0.091	0.171
KPP-5-K KPP-5			0.490			0.377	0.205					0.263	0.078	0.103	0.090			0.206
KB								0.090					0.082	0.089				

The analysis of Table 1 shows that the intensity of lateral rail wear on wooden sleepers with D0 and SKD65-D fasteners is lower than with SKD65-B and KPP-5-K fasteners on reinforced concrete sleepers.

Lateral rail wear intensity increases as the radius decreases [17]. On average, wear increases 1.2 times as the gradient increases. This is also due to the way the train operates on the uphill and downhill sections.

To prevent and eliminate wheel slip in electric locomotive traction on uphill gradients, locomotive drivers feed sand under the wheels, which effects wheel and rail adhesion and increases wear. The traction of the wheels and rails depends on the weight of the trains.

VI. TRAIN WEIGHT STANDARDS

The characteristics of jointless track operation in curves with a small radius of the track are described below. Jointless track on Ukrainian railways is mainly used in curves of R 350 m and on straight sections, and only in some cases in curves of 300 m

A critical weight limit for freight trains of up to

4.200 tonnes has been set on the experimental section of the Lviv Regional Railway. Prior to the experimental study, the weight standard was set at 4.600 tonnes. On this section, freight trains were hauled uphill by VL10 and VL11 locomotives, which consisted of 4 locomotives positioned - three at the head of the freight train and one at the rear end. In traction mode, the average speed of freight trains before weight reduction was between 25 and 30 km/h.

As the train passes through curves, the inertia of the wheel set flanges presses against the side surface of the outer rail head, causing friction between them. When passing a curve with a small radius, the end wheel sets of four-axle wagons are pressed against the outer rail.

The average weight of freight trains from the start of the trial on the odd-numbered line was reduced to 4.051 tonnes and the average speed of freight trains was increased to 41.1 km/h.

After the weight limit was reduced to 4.200 tonnes, the intensity of lateral rail wear gradually decreased, especially on the uphill sections where the gradient was greater than 10‰

On the curved track sections with a radius of up to 300 m, the intensity of lateral rail wear before train weight reduction averaged 0.427 mm/mln t of freight on the uphill section and 0.447 mm/mln t of freight on the downhill section. After reducing the weight of the trains, it was 0.398 mm/mln t of freight on the uphill section and 0.384 mm/mln t of freight on the downhill section. In curves with radii between 300 m and 450 m, before the train weight was reduced, the intensity of lateral rail wear was 0.276 mm/mln t of freight on the uphill section and 0.232 mm/mln t of freight on the downhill section. After reducing the weight of the trains, the rail wear was 0.253 mm/mln t of freight on the uphill section and 0.184 mm/mln t of freight on the downhill section. In curves with radii of 450 m and more, the wear before weight reduction was 0.092 mm/mln t of freight on the uphill section and 0.119 mm/mln t of freight on the downhill section; after weight reduction it was 0.098 mm/million tonnes of freight on the uphill section and 0.122 mm/mln t of freight on the downhill section. In percentage terms, the intensity of lateral rail wear decreased by 6.8% on the uphill gradient and by 14% on the downhill gradient on the curved track sections with a radius of up to 300 m; in curves with a radius of between 300 m and 450 m, the reduction in rail wear was 8.3% on the uphill gradient and 20.6% on the downhill gradient; in curves with a radius of 450 m and more, the wear decreased: the intensity of rail wear increased by 6.1% on the uphill gradient and by 2.5% on the downhill gradient.

After weight reduction, the average lateral rail wear rate in curves with radii up to 300 m was 0.286 mm/mln t of freight on the uphill section and 0.201 mm/mln t of freight on the downhill section. In curves with radii between 300 m and 450 m, the average intensity was 0.185 mm/mln t of freight on the uphill section and 0.171 mm/mln t of freight on the downhill section. In curves with radii of 450 m and more, the wear was 0.089 mm/mln t of freight on the uphill section and 0.098 mm/mln t of freight on the downhill section. As a percentage of the year, the intensity of lateral rail wear decreased by 28.1% on the uphill sections of the track with a radius of up to 300 m and by 47.6% on the downhill sections; respectively, in curves with a radius between 300 m and 450 m, the reduction in rail wear was 26.8% on the uphill sections and 7.1% on the downhill sections; in curves with a radius of 450 m and more, the wear decreased by 9.2% on the uphill sections and by 19.6% on the downhill sections.

In comparison with the results at the time of the test, after the reduction in train weight, the intensity of the lateral rail wear in percentage terms decreased on the curved track sections with a radius of up to 300 m, on the uphill gradient to 33% and on the downhill gradient to 55%; respectively, on the curves with a radius between 300 m and 450 m, the reduction in the rail wear was: up to 32.9% on the uphill section and 26.3% on the downhill section; on the curves with a radius of 450 m and more, the reduction in wear was 3.2% on the uphill section and 17.6% on the downhill section.

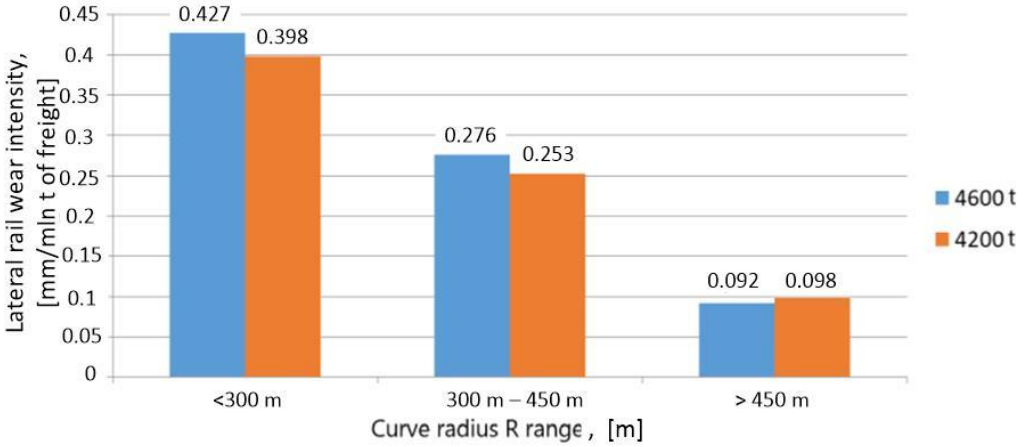

Figure 10. *Weight indicators as a function of the intensity of lateral rail wear on the uphill sections*

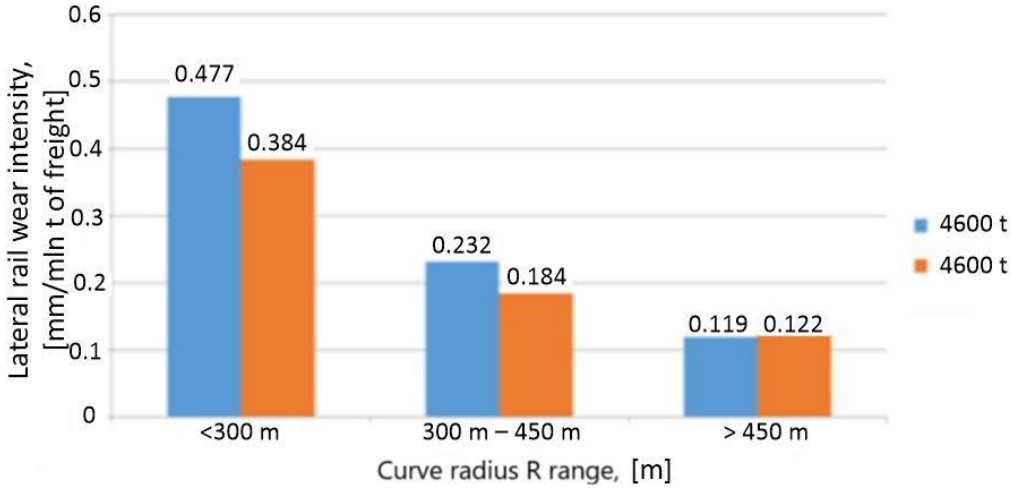

Figure 11. *Weight indicators as a function of the intensity of lateral rail wear on the downhill sections*

On the downhill section of the test line, freight trains were operated by two locomotives due to the twice lower load (running with empty cars), so that the intensity of the lateral rail wear is lower than on the uphill section. Increased wear of the rolling stock wheel sets and of the rails on the downhill section occurs during regenerative braking when the movement is performed by two locomotives, especially on the S-curves and on the curves with small radii, uncontrolled movement of freight wagons occurs, which affects the condition of the track, namely: increased rail wear, displacement of the rail in the direction of movement, skewing of the sleepers, contamination of the road-metal with sand during braking.

Electric regenerative braking concentrates the braking force within the wheelbase of one or more locomotives, which can lead to asynchronous interaction between coupled locomotives when the head locomotive brakes and the rear locomotive rolls onto the rolling stock, ejecting empty cars and possibly loaded cars from the train.

Here is an example of the effect of braking on the intensity of lateral rail wear on a section with a gradient of 28.3 ‰, with a curve radius of 255 m, the intensity of lateral rail wear is 0.538 mm/mln t of freight. At the same time, the regenerative braking modes are only controlled by changing the moving speed. In other words, they are not really controlled.

Multi-section locomotives at the head of the train, the use of rheostat or regenerative braking, emergency and full service braking and locomotive brakes all increase the quasi-static longitudinal compressive forces in the train. When freight trains use pneumatic braking, the brakes in the cars are applied gradually, starting at the head of the train, with additional kinetic energy generated in the last third of the train as the unbraked rear end of the train rolls onto the braking end. If loaded cars are rolled

onto the cars of a train that has already stopped, empty cars can be ejected out of the train.

VII. TRACTION MODE, SPEED MODE, OUTER RAIL HEIGHT

If the outer rail height of the curve corresponds to the speed mode, the load on both rails is equal, so less energy is used in the traction mode to overcome the uphill sections. The effect of outer rail height on lateral wear intensity under different traction conditions is discussed below.

In order to determine the influence of changes in the outer rail height on the wear of the wheel-rail pair, the track sections where only the outer rail height was changed over a different period of time under the same operating conditions (R–m, type of fastening, uphill and downhill gradients, traction and braking modes) were selected.

The following indicators have been analysed:

- $h_{cp\ max}$ is the average value of the maximum outer rail height on the curved track section;
- $h_{cp\ min}$ is the average value of the minimum outer rail height in on the curved track section;
- $i_{cp\ max}$ is the average value of the intensity of the lateral rail wear indicators corresponding to the

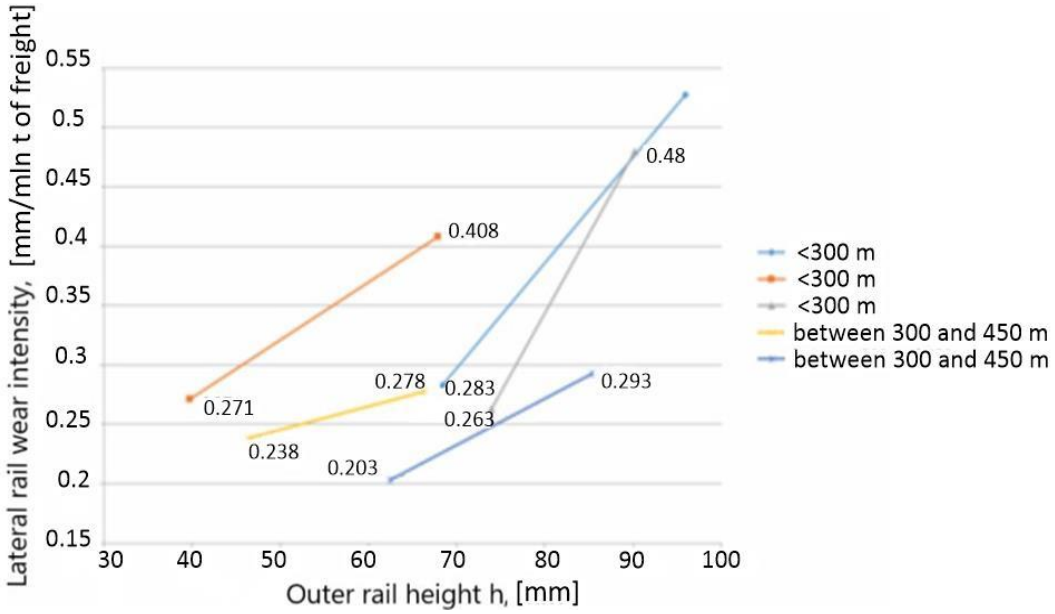

Figure 12. *Change in outer curve rail height as a function of the intensity of lateral rail wear on the uphill sections*

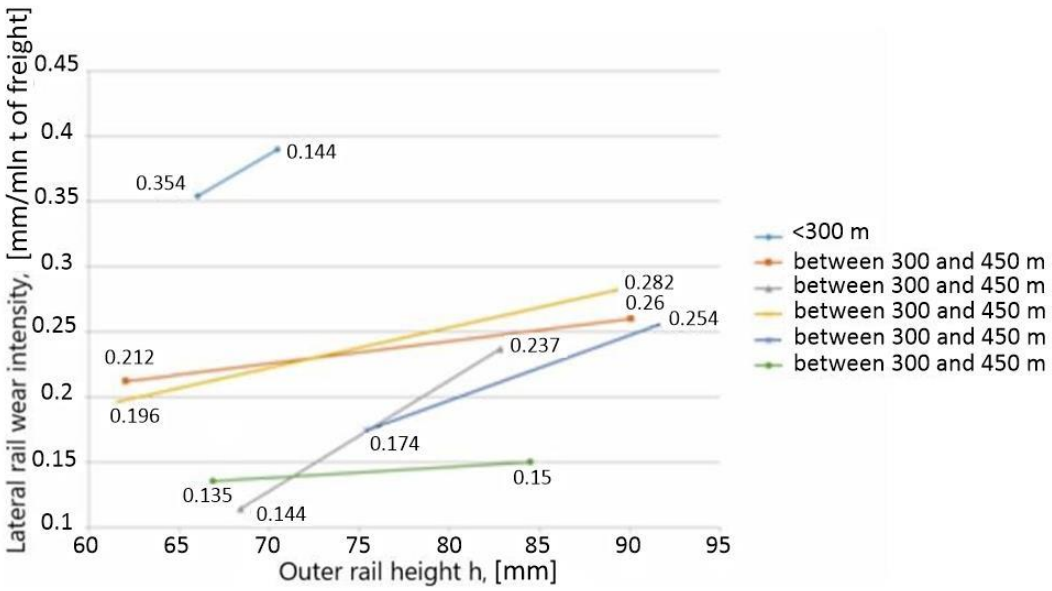

Figure 13. *Change in outer curve rail height as a function of the intensity of lateral rail wear on the downhill sections*

maximum values of the outer rail height on the curved track section;

- $i_{cp\ min}$ is the average value of the lateral wear intensity indicators corresponding to the minimum values of the outer rail height on the curved track section.
- h_{recom} is the recommended outer rail height on the curved track section in accordance with the actual speed of the movement;
- V_{av} is the average actual speed, in km/h;
- traction and braking modes (see **Table 2**).

When analysing the data on the change in outer rail height on the curved track section on mountain passes, the percentage reduction in height gives a positive result from 4.70% to 53.6%. This analysis shows that, on the above-mentioned sections, the maximum height value is calculated for speeds that are not actually reached by either passenger or freight trains. Therefore, when the outer rail height is reduced, the intensity of lateral wear is significantly reduced in areas with a gradient of 10‰ to 20 ‰ (from 18.46 % to 53.6 %), and in areas with a gradient of 20 ‰ (from 4.7 % to 51.68 %).

Thus, at a gradient of 10 ‰ to 20 ‰, both uphill and downhill, an excessive increase in the outer rail

Table 2. *The data of analysed indicators*

Slope of the site	Site characteristics	$h_{cp\ max}$ mm	$h_{cp\ min}$ mm	$i_{cp\ max}$ mm/mln t of freight	$i_{cp\ min}$ mm/mln t of freight	$i_{cp\ min}$ relatively $i_{cp\ max}$, %	Average actual speed, km/h	Mode of movement on the site	h_{rekom}, mm
From 10‰ to 20‰	Ascent 11.2 ‰, KPP-5-K, R - 275 m	95.92	68.36	0.528	0.283	53.59	30	Traction mode	40
	Ascent 15.6 ‰, SKD65-B, R - 270 m	67.87	39.72	0.408	0.271	33.57	21	Overclocking	20
	Descent 13.6 ‰, KPP-5-K, R - 304 m	90.06	62.02	0.260	0.212	18.46	24	Overclocking	25
>20‰	Ascent 21.9 ‰, SKD65-B, R - 300 m	66.33	46.36	0.278	0.238	14.14	24	Overclocking	25
	Descent 22.5 ‰, KPP-5-K, R - 240 m	70.46	66.0	0.390	0.354	9.23	32	Braking	53
	Descent 27.9 ‰, KPP-5-K, R - 315 m	82.8	68.42	0.237	0.114	51.68	37	Braking	54
	Descent 22.8 ‰, KPP-5-K, R - 300 m	89.3	61.6	0.282	0.196	30.49	40	Braking	67
	Ascent 24.5 ‰, SKD65-B, R - 300 m	85.3	62.42	0.293	0.203	30.93	29	Traction mode	35
	Descent 24.2 ‰, KPP-5-K, R - 316 m	91.78	75.37	0.256	0.174	32.03	41	Braking	66
	Ascent 23.1 ‰, SKD65-B, R - 265 m	90.2	73.93	0.480	0.263	45.20	28	Traction mode	37
	Descent 22.8 ‰, KPP-5-K, R - 342 m	84.5	66.86	0.150	0.135	9.6	22	Braking	17

$h_{cp\ max}$ is the average value of the maximum outer rail height on the curved track section.
$h_{cp\ min}$ is the average value of the minimum outer rail height in on the curved track section.
$i_{cp\ max}$ is the average value of the intensity of the lateral rail wear indicators corresponding to the maximum values of the outer rail height on the curved track section.
$i_{cp\ min}$ is the average value of the lateral wear intensity indicators corresponding to the minimum values of the outer rail height on the curved track section.
h_{recom} is the recommended outer rail height on the curved track section in accordance with the actual speed of the movement.
Link track with rails 25 m long.

on the curved track section causes an increase in the lateral wear rate of the rail head. A similar result is observed in areas with a gradient of 20 ‰ or more.

For the uphill sections where the traction mode is used, higher values of lateral wear intensity are observed (average value of 0.361 mm/mln t of freight) compared to the downhill sections where the braking is used (average value of 0.262 mm/mln t of freight). The higher values of lateral wear in the uphill sections can be explained by the use of sand to improve the adhesion coefficient between wheel and rail, and by the presence of excessive outer rail height in all the above-mentioned curves in the uphill sections. This is also explained by the fact that the average weight of a freight train going uphill is 4.051 tonnes and requires 4 locomotives, while going downhill with empty cars it requires only 2 locomotives. The only exception is when regenerative braking is used on gradients of more than 20 ‰.

Taking into account the results obtained, it is recommended to adjust the outer rail height according to the actual train speed on the curved track sections with gradients between 10 ‰ and 20 ‰ and above 20 ‰. This will reduce the intensity of lateral rail wear in curves and also reduce traction resistance.

VIII. CONCLUSIONS

1. In the case of jointed track, the joint is the main cause of track disturbances, subsidence, distortion, and angles in the design (vertical and horizontal deviations from the design line), sleeper breaks, swelling and abrupt rail wear.

2. When analysing the lateral wear of rails on a jointed track, a characteristic pattern of lateral wear along the entire curve is formed during the 'proper driving' of trains, during which abrupt rail wear occurs.

3. Abrupt rail wear in the joint area at a distance of 1 m from the end of the trailing and leading rails in the direction of train movement shows a difference in wear values of up to 6 mm.

4. On a jointless track, the rail wear has a smooth line and there is no deviation in the lateral rail wear of more than 2 mm at adjacent points. The difference between the two critical wear points of the rail is no more than 3.2 mm, and reaches 13.5 mm in a circular curve of a jointed rail.

5. Weight reduction results in a percentage reduction in wear of contacting surfaces on the curved track sections with a radius of up to 300 m, up to 33% on the uphill section and up to 55% on the downhill section; respectively, in curves with a radius between 300 m and 450 m, the reduction in rail wear is: up to 32.9% on the uphill section and 26.3% on the downhill section; in curves with a radius of 450 m and more, the reduction in rail wear is: up to 3.2% in the uphill section and 17.6% in the downhill section.

6. In order to reduce the resistance to movement on the uphill section, it is necessary to reduce the height of the outer curve rail and adjust it to the speed mode when driving in traction mode.

7. On uphill and downhill sections, reducing the outer rail height and adjusting it to the speed mode, in both traction and braking modes, reduces wear on the wheel-rail contact surfaces, except in the case of regenerative braking on sections with gradients greater than 20 ‰.

8. To reduce wear in the wheel-rail pair, the number of joints should be reduced.

9. Wear in a wheel-rail pair is least significant when the speed limit is close to the outer curve rail height.

AUTHOR CONTRIBUTIONS

All authors made a substantial, direct, and intellectual contribution to this work. The manuscript was written through the contribution of all authors. All authors discussed the results, reviewed and approved the final version of the manuscript.

DISCLOSURE STATEMENT

The authors declare that they have no known competing financial interests or personal relationships that could have appeared to influence the work reported in this paper.

ORCID

Y. Makarov http://orcid.org/0009-0006-3869-2200

R. Zaleskyi http://orcid.org/0009-0007-7345-6040

M. Mykhalichenko http://orcid.org/0009-0006-9138-7491

REFERENCES

[1] S. Fischer, D. Németh, H. Horváth, Investigation of the Track Gauge in Curved Sections, Considering Hungarian Railway Lines, Infrastructures, 2023, 8 (4), 69. https://doi.org/10.3390/infrastructures8040069

[2] M. Kurhan, D. Kurhan, M. Husak, & N. Hmelevska, Determination of the type and the length for the transition curves on the directions of high-speed train operation, Acta Technica Jaurinensis, 2022, 15 (2) pp. 117-124.

https://doi.org/10.14513/actatechjaur.00658

[3] L. Kou, M .Sysyn, J. Liu, O. Nabochenko, Y. Han, D. Peng, and S. Fischer. "Evolution of Rail Contact Fatigue on Crossing Nose Rail Based on Long Short-Term Memory", Sustainability 2022, 14 (24) 16565. https://doi.org/10.3390/su142416565

[4] V. Jóvér, Z. Major, A. Németh, D. Kurhan, M. Sysyn, S. Fischer Investigation of the Geometrical Deterioration of Paved Superstructure Tramway Tracks in Budapest (Hungary), Infrastructures, 2023, 8 (8) 126. https://doi.org/10.3390/infrastructures8080126

[5] D. Kurhan, R. Novik, S. Baydak and N. Hmelevska, Improvement of the railway track efficiency by minimizing the rail wearing curves, 2022 IOP Conference Series: Materials Science and Engineering, 985, 012001. https://doi.org/10.1088/1757-899X/985/1/012001

[6] D. Kurhan, M. Havrylov, The Mathematical Support of Machine Surfacing for the Railway Track, Acta Technica Jaurinensis, 2020, 13 (3) pp.246–267. https://doi.org/10.14513/actatechjaur.v13.n3.556

[7] M. Kazemian, F. Astaraki, A. Mohammadidoost, M. Akbarivarmaziar, M. Movahedi Rad, S. Fischer, Effects of Wheel Surface Defects on Ground Borne Vibration, Acta Polytechnica Hungarica, 2022, 19 (6) pp. 129-141.

[8] Ezsias L., Brautigam A., KocsisSzurke S., Szalai S., Fischer S., 2023, Sustainability in railways – a review, Chemical Engineering Transactions, 107, pp. 7-12. https://doi.org/10.3303/CET23107002

[9] K.Dybeł, A.Kampczyk, Sensitivity of Geometric Parameters in the Sustainability Development of Continuous Welded Rail, Acta Technica Jaurinensis, 2022, 15 (3) pp. 150-161. https://doi.org/10.14513/actatechjaur.00663

[10] A. Brautigam, S. Szalai, S. Fischer, Investigation of the application of austenitic filler metals in paved tracks for the repair of the running surface defects of rails considering field tests. Facta Universitatis, Series: Mechanical Engineering. https://doi.org/10.22190/FUME230828032B

[11] S. Fischer, D. Harangozó, D. Németh, B. Kocsis, M. Sysyn, D. Kurhan, A. Brautigam, investigationofheat-affectedzones of thermite rail weldings. Facta Universitatis, Series: Mechanical Engineering. https://doi.org/10.22190/FUME221217008F

[12] A. Németh, S. Fischer, Investigation of the glued insulated rail joints applied to cwr tracks, Facta Universitatis, Series: Mechanical Engineering, 2021, 19 (4), pp. 681-704. https://doi.org/10.22190/FUME210331040N

[13] V. Rybkin, M. Nastechyk, M. Arbuzov, K. Kalenyk, Yu. Makarov, R. Markul// Investigation of the influence of track design parameters on the intensity of rail head lateral wear on the curved track sections, Collection of scientific papers of the Donetsk Institute of Railway Transport, 2013, 34, pp. 155-162.

[14] V. Hovorukha, Yu. Makarov, Investigation of lateral rail wear under mechanical interaction of track and wheels of railway car chassis on the curved track section / Geotechnical Mechanics: Interdisciplinary collection of scientific papers / Institute of Geotechnical Mechanics by N. Poljakovof National Academy of Sciences of Ukraine/ – Dnipro,2017. 134, pp. 125-140. http://dspace.nbuv.gov.ua/handle/123456789/141330

[15] V. Rybkin, O. Patlasov, O. Bielousov, M. Karpov, D. Kurhan, V. Shramenko, A. Babenko, engineer, V. Shtoiko, I. Oliinyk,V. Lysak, j.r.f., K. Kalenyk Technical instructions for design, laying, repair and maintenance of jointless trackon the railways of Ukraine [Text]: Instruction published by Ukrzaliznytsia /. - K., 2012, pp. 6-7.

[16] Ye. Blokhin, A. Pshynko, V. Danovych, M. Korotenko, Assess the impact of deviations from maintenance standards // Report of the International Scientific and Practical Conference "Problems of the interaction between the track and the rolling stock." – 1998, pp. 12-14.

[17] Ye. Danilenko, A. Orlovskyi, M. Umanov, O. Patlasov, M. Karpov, V. Sharamenko, O. Bielorusov, V. Yakovliev, engineer, V. Molchanov, K. Kornoukhova, engineer. Instruction on the design and maintenance of the track of the Railways of Ukraine [Text]: Instruction published by Ukrzaliznytsia / – K., 2012, pp. 47-78.

[18] Ye. Blokhin, V. Danovych, M. Korotenko, L. Manashkin, Mathematical model of forced oscillations of the train-staff-rail system for wheel and rail wear assessment // Report of the IX International Conf. "Problems of Railway Transport Mechanics." – 1996, 59 p.

[19] Ye. Danilenko, V. Rybkin, Rules for calculating the strength and stability of railway tracks. ЦП–0117 (TsP-0117) / – Kyiv: Transport of Ukraine, 2004. 64 p.

[20] Ye. Danilenko, A. Orlovskyi, M. Umanov, O. Patlasov, M. Karpov, V. Sharamenko, O. Bielorusov, V. Yakovliev, engineer, V. Molchanov, K. Kornoukhova, engineer. Instruction on the design and maintenance of the track of the Railways of Ukraine [Text]: Instruction published by Ukrzaliznytsia / – K., 2012, pp. 38-39.

[21] S. Demchenko, A. Taturevych, Yu. Makarov Influence of different types of rail fasteners on the integrity of rail wear on the curved track sections / "Railway Transport of Ukraine",2023. 1, pp. 27-33. http://nbuv.gov.ua/UJRN/ZTU_2023_1_5

[22] Ye. Blokhin, S. Miamlin, N. Serhiienko Increased wheel and rail wear is a critical transport problem / "Railway Transport of Ukraine", 2011, 1, pp. 10-14.